UNIVERSITÀ DEGLI STUDI DI PADOVA

SCUOLA DI SCIENZE
Dipartimento di Geoscienze
Direttore Prof. Fabrizio Nestola

TESI DI LAUREA MAGISTRALE
IN
GEOLOGIA E GEOLOGIA TECNICA (LM-74)

Estimate of earthquake source parameters from an exhumed ancient seismogenic fault (Gole Larghe Fault Zone, Italy)

Relatore: Prof. Giulio Di Toro

Laureando: Francesco Lazari
Matricola: 1233544

ANNO ACCADEMICO 2020/2021

Contents

Riassunto

I metodi di inversione delle onde sismiche sono estremamente utili per comprendere la meccanica dei terremoti. Alcuni parametri della sorgente sismica, però, come l'evoluzione della resistenza al taglio τ_f e la potenza frizionale dissipata ($\dot{Q} = \sigma_N \, \mu_{ss} \, \dot{u}$ in MW/m^2, dove σ_N è lo sforzo normale, μ_{ss} è il coefficiente d'attrito allo steady state e $\dot{u}$ è la velocità di scivolamento durante il sisma) non possono essere conosciuti tramite inversione delle onde sismiche. Tuttavia, i due parametri τ_f e $\dot{Q}$ sono estremamente importanti per approfondire la nostra conoscenza dei terremoti, dato che controllano la velocità di rilascio dell'energia, l'aumento di temperatura sulla faglia e, di conseguenza, l'attivazione di meccanismi di indebolimento dinamico della faglia.

Studiare i fusi di frizione, conservati nel record geologico sotto forma di pseudotachiliti ed esumati dall'attività orogenetica, permette di osservare intere faglie, lunghe da alcuni metri a centinaia di metri, che possono essere studiate per ricavare τ_f (Sibson, 1975; Di Toro et al., 2006). In uno studio precedente (Nielsen et al., 2010), gli autori hanno proposto un modello che mette in relazione $\dot{Q}$ e la micro-rugosità del bordo tra pseudotachilite e roccia incassante. La potenza frizionale dissipata, infatti, è proporzionale al riscaldamento frizionale: se $\dot{Q}$ aumenta, aumenta anche il gradiente termico perpendicolare alla faglia durante lo scivolamento cosismico.

Dato che le rocce sono solitamente composte da diversi minerali con diverse temperature di fusione, un gradiente termico elevato (alto $\dot{Q}$) farà sì che i minerali fonderanno omogeneamente vicino alla superficie di scorrimento della faglia (cioè indipendentemente dal loro punto di fusione), generando un contatto liscio tra pseudotachilite e roccia incassante. Al contratio, un gradiente termico più blando (basso $\dot{Q}$) con le isoterme distanziate causerà la fusione preferenziale dei minerali con temperatura di fusione più bassa, producendo così un contatto rugoso tra pseudotachilite e roccia incassante.

Un primo tentativo di stima della potenza frizionale dissipata è stato effettuato nella tesi di Laurea Magistrale di (Castagna, 2012), in cui l'autrice ha dimostrato che la micro-rugosità nelle pseudotachiliti artificiali prodotte con SHIVA (una potente macchina sperimentale rotary progettata per riprodurre in laboratorio le condizioni di deformazione tipiche di un terremoto naturale; Di Toro et al., 2010) diminuisce all'incrementare di $\dot{Q}$. Tuttavia questa relazione (la diminuzione della micro-rugosità con l'aumentare di $\dot{Q}$) nelle pseudotachiliti naturali non era ben definita e, soprattutto, non fu possibile stimare $\dot{Q}$ nelle faglie naturali. La micro-rugosità delle pseudotachiliti naturali, infatti, risultava notevolmente più elevata di quella dei campioni sperimentali, rendendo molto complicato un confronto diretto tra pseudotachiliti naturali e sperimentali.

In questa tesi, tento di migliorare la relazione tra pseudotachiliti naturali e potenza frizionale dissipata per ottenere una stima di $\dot{Q}$. Per raggiungere l'obiettivo, raccolgo cinque nuovi campioni dalla faglia delle Gole Larghe (GLFZ, batolite dell'Adamello, Alpi Meridionali centrali) ed effettuo un'analisi microstrutturale dettagliata di 22 campioni accuratamente selezionati dalla vasta collezione di pseudotachiliti campionate negli anni dalla faglia delle Gole Larghe dal gruppo di ricerca del Prof. Di Toro. Uno degli scopi principali è l'identificazione dei processi fisici che agiscono sul contatto tra pseudotachilite e roccia incassante durante la propagazione della rottura e lo slip sismico. Effettuo anche una revisione e implemento uno script MATLAB®per descrivere quantitativamente la micro-rugosità (espressa attraverso l'altezza caratteristica delle asperità, ω_0, e il raggio medio delle asperità, λ_{ave}).

Questa analisi microstrutturale, unita alla revisione del metodo di calcolo della micro-rugosità, porta ad una solida relazione tra micro-rugosità e potenza frizionale dissipata nelle faglie naturali, anche se una precisa stima di $\dot{Q}$ utilizzando i campioni sperimentali per la calibrazione non è possibile. La micro-rugosità delle faglie naturali infatti, prima della fusione, è dovuta anche a (1) il danneggiamento indotto dalla propagazione della rottura sismica, che non è riprodotto negli esperimenti di laboratorio che simulano le condizioni dei terremoti, e (2) la rugosità iniziale delle faglie naturali, che è più elevata di quella nelle faglie sperimentali (queste ultime sono molto levigate per prevenire complicazioni durante gli esperimenti). Ciononostante, per faglie naturali in condizioni quasi ideali che, come discusso in questa tesi, soddisfano i le assunzioni fatte nel modello teorico proposto da

Nielsen et al. (2010), è possibile stimare $\dot{Q}$. Per queste faglie ho stimato che la potenza frizionale dissipata negli antichi terremoti della faglia delle Gole Larghe è stata di 156$\pm$90 $\frac{MW}{m^2}$. Questa stima di $\dot{Q}$, che è la prima stima della potenza frizionale dissipata basata unicamente su dati di campagna mai effettuata, è più alta di quanto predetto in precedenza (10-100 $\frac{MW}{m^2}$) da modelli semplificati dei terremoti (e.g., Sibson, 1980).

Abstract

Seismological inversion methods are extremely useful to understand the mechanics of earthquakes. However, some earthquake source parameters such as fault strength evolution (τ_f) and frictional dissipated power ($\dot{Q} = \sigma_N \, \mu_{ss} \, \dot{u}$ in MW/m^2, where σ_N is the normal stress, μ_{ss} is the friction coefficient at steady state and $\dot{u}$ is the slip rate) cannot be derived by the inversion of seismic waves. Nevertheless, τ_f and $\dot{Q}$ are extremely important to improve knowledge about earthquakes, since they control the moment release rate, the temperature increase in the slip zone and therefore the activation of coseismic fault dynamic weakening mechanisms.

The study of frictional melts, preserved in the geological record as pseudotachylytes and exhumed by orogenic activity, allows the observation of entire fault segments from few to hundreds meters that can be studied to retrieve τ_f (Sibson, 1975; Di Toro et al., 2006). In a previous study (Nielsen et al., 2010), the authors proposed a theoretical model that linked $\dot{Q}$ to the pseudotachylyte-host rock boundary micro-roughness. Frictional dissipated power, indeed, is proportional to shear heating: increasing $\dot{Q}$ increases the temperature gradient perpendicular to the fault during coseismic slip.

Since rocks are usually composed by different minerals with different melting temperatures, a high thermal gradient (high $\dot{Q}$) will cause the minerals to melt uniformly near the sliding surface (i.e., independently of their melting points), resulting in a relatively smooth pseudotachylyte-wall rock boundary. On the other hand, a gentle temperature gradient (low $\dot{Q}$) with widely-spaced isotherms will mainly melt those minerals with low melting points, generating a rough boundary.

A first attempt at estimating frictional dissipated power using pseudotachylyte micro-roughness was performed in the M.Sci. thesis of Castagna (2012), where the author proved that artificial pseudotachylytes produced with SHIVA (a powerful rotary shear apparatus

designed to reproduce in the laboratory deformation conditions typical of natural seismic fault slip; Di Toro et al., 2010) become smoother with increasing $\dot{Q}$. However, this relationship (pseudotachylyte-wall rock smoothing with increasing $\dot{Q}$) was not well-established in natural pseudotachylytes and it was not possible to estimate frictional dissipated power in natural faults. Moreover, micro-roughness on natural pseudotachylytes was found to be considerably higher than the one found in experimental pseudotachylytes, making a direct comparison between natural and experimental faults very challenging.

In this thesis, I try to refine the relationship between micro-roughness and frictional dissipated power in natural pseudotachylytes to get an estimate of $\dot{Q}$. In order to do so, I collect five new samples from the Gole Larghe fault zone (GLFZ, Adamello batholith, Southern Alps) and perform a detailed microstructural analysis of 22 carefully selected samples from the large collection of pseudotachylytes from the GLFZ produced in the years by the research group of Prof. Di Toro. One of the main goals was also to identify the physical processes acting on the pseudotachylyte-host rock boundary during seismic rupture propagation and slip. I also revise and improve a MATLAB®script used to quantitatively describe the micro-roughness (expressed as the characteristic asperities height, ω_0, and the average asperities radius, λ_{ave}).

The microstructural analysis, together with the refinement of the micro-roughness measurement methodology, lead to a robust relationship between the micro-roughness and frictional dissipated power in natural faults, though a precise estimate of $\dot{Q}$ using the experimental data for the calibration is still not possible. In fact, micro-roughness of natural pseudotachylytes is also related to (1) the wall-rock damage induced by the propagation of the seismic rupture, which is not reproduced in the laboratory experiments simulating seismic slip and (2) the initial roughness of the natural faults, which are rougher than the experimental ones (the latter are well-polished for experimental issues).

However, for natural near-ideal faults which, as discussed in this thesis, satisfy the assumptions for the theoretical model proposed by Nielsen et al. (2010), I estimated for the GLFZ ancient earthquakes frictional dissipated power values of $156 \pm 90 \ \frac{MW}{m^2}$. This estimate, which is the first field-based frictional dissipated power estimate for an earthquake ever produced, is slightly larger than the $\dot{Q}$ predicted (10-100 $\frac{MW}{m^2}$) from simplified earthquake models (e.g., Sibson, 1980).

Chapter 1

Introduction

1.1 Motivations

In seismology, with seismic inversion methods, it is possible to retrieve several fundamental earthquake source parameters (stress drop, focal mechanisms, hypocentral depth, seismic moment magnitude, rupture speed, rupture directivity, fault slip rates, particle velocities, fracture energy, etc.) which are at the base of the understanding of earthquake physics (Scholz, 2019). However, earthquake physics (rupture propagation and arrest, coseismic slip velocity, earthquake energy budgets, etc.) is also related to the evolution of fault strength during seismic slip and to a wealth of deformation mechanisms activated in the fault slip zone ("on-fault processes") and in the damaged wall rocks ("off-fault processes") bordering the slip zone (Di Toro et al., 2011). While the active slip zone is considered to be few centimeters thick at most (Sibson, 2003, Fondriest et al., 2013, Austrheim and Boundy, 1994), the damage fault zone can be up to several hundred meters thick (Fondriest et al., 2020a). Because of the low frequency and long wavelength of the seismic waves detected at the surface, information about on-fault and off-fault deformation processes can be hardly obtained from the inversion of seismic waves. As a consequence, geological field surveys on exhumed seismogenic fault zones and dedicated laboratory experiments can be complementary to seismological studies (e.g. Di Toro et al., 2010).

Investigations of active faults at depth, carried out with fault drilling projects (e.g., Koyna drilling project, Gupta et al., 2014; Wenchaun drilling project, Li et al., 2013; SAFOD drilling project, Zoback et al., 2010), grant access to real-time data such as pore fluid

pressures and strain rates at depth, and to fault rock specimens that had limited overprint during the seismic cycle. However, these projects are extremely expensive and allow the investigation of very small volumes of the fault (the diameter of the cores is limited to tens of centimeters at most) and drilling is limited to 3 km depth, while most crustal earthquakes nucleate and propagate at larger depths. Field surveys, on the other hand, allow us the investigation of large volumes (tens of kilometers in length in some cases) of exhumed fault zones. This approach enable detailed reconstructions of fault zone architecture and geometry, and also to describe and collect fault zone rocks. Some of the limitations of the field studies of exhumed faults are that it is difficult, or simply not possible at all, relate the sampled fault rocks to a precise seismic event and that the pristine coseismic fault rock assemblages might be overprinted by different processes (e.g., fluid-rock interaction and alteration, Fondriest et al., 2020b; overprinting by other deformation processes during exhumation).

Between the earthquake source parameters, fault strength evolution (τ_{ave}) and frictional dissipated power ($\dot{Q}$) are extremely difficult to estimate by seismic inversion data (Guatteri and Spudich, 1998). Fault strength evolution is defines as $\tau_{ave} = \frac{E\ \omega}{u}$ (Sibson, 1975; Di Toro et al., 2006) where $E \approx 1.7\ \frac{MJ}{kg}$ is the heat for melting, ω is the average pseudotachylyte thickness and u is the displacement, whereas the frictional dissipated power can be defined as $\dot{Q} = \mu_{ss}\ \sigma_N\ \dot{u}\ [\frac{Mw}{m^2}]$ (Sibson, 1980), where μ_{ss} is the friction coefficient at steady-state, σ_N is the normal stress and $\dot{u}$ is the on-fault coseismic slip rate. However, these parameters are crucial in earthquake physics, as they control the release of elastic strain from the wall rocks (and thus the propagation of the seismic rupture), the temperature increase in the slip zone and the activation of several coseismic deformation mechanisms which result in "fault dynamic weakening" (Di Toro et al., 2011). In natural faults, τ_{ave} and $\dot{Q}$ can be estimated from the meso- and micro-structural investigations of pseudotachylyte-bearing faults (Sibson, 1975, Di Toro et al., 2006, Nielsen et al., 2008, Nielsen et al., 2010, Castagna, 2012).

Pseudotachylytes are solidified friction melts produced during seismic slip in silicate-built natural faults (Sibson, 1975). In particular, theoretical and experimental arguments support the hypothesis that

1. the ratio of the average thickness of pseudotachylyte (ω) versus displacement (u)

accommodated by the pseudotachylyte-bearing fault allows us to estimate the average dynamic fault strength during seismic slip (i.e., $\tau_{ave} = \frac{E\ \omega}{u}$, Sibson, 1975, Di Toro et al., 2006)

2. the micro-roughness of the pseudotachylyte-wall rock boundary (described by the roughness asperities radius λ_{ave} and amplitude ω_0) allows us to determine the frictional dissipated power ($\dot{Q} \propto \frac{1}{\lambda\,\omega_0}$, Nielsen et al., 2010).

However, to obtain estimates of τ_{ave} and $\dot{Q}$, the studied pseudotachylyte-bearing faults should satisfy a series of characteristics and assumptions:

1. polished and extended outcrops, which allow to measure the average thickness of the pseudotachylyte-bearing fault;
2. structural markers (e.g. dykes) which allow to estimate the coseismic fault slip;
3. the studied faults need to record only one seismic slip event (this can be constrained by dedicated microstructural studies, Pittarello et al., 2008);
4. the average coseismic slip rate of about 1 m/s;
5. knowledge of the ambient conditions (depth, presence of fluids, etc.) during seismic faulting.

In particular, the first attempt to estimate the frictional dissipated power from natural faults was carried out in Castagna (2012). In her thesis, the estimates for frictional dissipated power were calibrated with dedicated experiments simulating seismic slip conditions and performed on the same rocks of the natural exposures. The results of Castagna's thesis were extremely promising, but in order to obtain more robust conclusions the natural dataset requires to be expanded.
Motivated by the preliminary results of Castagna (2012), in this thesis my main goal is to obtain more accurate estimates of $\dot{Q}$ from natural faults, by:

1. adding further constrains on seismic faulting conditions at typical earthquake nucleation depth (e.g., slip rate $\dot{u}$, dynamic fault strength τ_{ave});

2. expanding the number of the sampled natural faults to produce a more robust statistical dataset;

3. investigating the processes involved in the formation of pseudotachylyte micro-roughness with a detailed microstructural analysis;

4. revising and improving the MATLAB®script used to quantitatively determine the micro-roughness of natural and experimental faults.

1.2 State of the art

The relationship between frictional dissipated power and pseudotachylytes micro-roughness has been theorized by Nielsen et al. (2010) (see section 1.2.3) and early tested by Castagna (2012), though more detailed data are required to improve the robustness of the dataset. Here we present the basic concepts of earthquake energy budget and pseudotachylyte production, as well as the principal hypothesis behind frictional evolution during coseismic slip and the effect of increasing frictional dissipated power on micro-roughness (i.e., in general, the roughness of a fault at the scale of the grain size of the rock, see Figure 1.6).

1.2.1 Earthquake energy partitioning

An earthquake is a plastic (irreversible) and brittle (localized) deformation of the Earth's crust in response to the action of stresses (e.g. plate motion, tectonic or human-induced stress perturbations) which results in the instantaneous release of the elastic strain energy stored in the rocks in centuries or millennia. Because of tectonic loading, wall rocks deform elastically storing potential (elastic) strain energy, which is released when the shear stress acting on the fault overcomes the fault yield strength. The stored elastic strain energy is released in seconds to minutes as radiated (seismic) energy, fracture energy, and thermal energy.

Following Kanamori and Rivera (2006), we can subdivide the total energy released during an earthquake as follows:

$$E_T = E_R + E_{NR} \quad [\frac{J}{m^2}] \tag{1.1}$$

Where E_T is the total released energy, E_R is the radiated energy, used to produce seismic waves, and E_{NR} is the non-radiated energy, that fuels on-fault processes and is not accessible to seismic investigations.
The non-radiated energy can be further divided:

$$E_{NR} = E_F + E_G \tag{1.2}$$

Where E_G, also called fracture energy, represents the energy for plastic yielding, rupture propagation and latent heat (if, for instance, during slip the temperature on the fault plane reaches the melting temperature of the rock, producing a pseudotachylyte). E_F is the frictional energy which, according to the interpretation in Pittarello et al. (2008), is partitioned into:

$$E_F = Q + U_S \tag{1.3}$$

Where Q is heat and U_S is the surface energy. At typical seismic nucleation depth, surface energy is thought to be negligible with respect to heat production (Pittarello et al., 2008), so that frictional energy per unit fault surface can be approximated as:

$$E_F \approx Q = \mu_{ss}\, \sigma_N\, u \tag{1.4}$$

With μ_{ss} being the friction coefficient at steady state. The first time derivative of heat is the heat flux, that can be approximated to the frictional dissipated power (that is the first time derivative of the frictional energy)

$$\dot{Q} = \mu_{ss}\, \sigma_N\, \dot{u} = \tau_{ss}\, \dot{u} \quad [\frac{W}{m^2}] \tag{1.5}$$

Since at typical earthquake nucleation depth σ_N is in the order of 10^8 Pa, $\dot{u}$ on average during seismic slip is about 1 m/s and μ_{ss} is between 0.05 and 0.2 in lubricated faults (Di Toro et al., 2006), $\dot{Q}$ is of the order of $10 - 100\ \frac{MW}{m^2}$. Such large frictional dissipated power, given the low thermal diffusivity of rocks, can lead to an abrupt temperature increase:

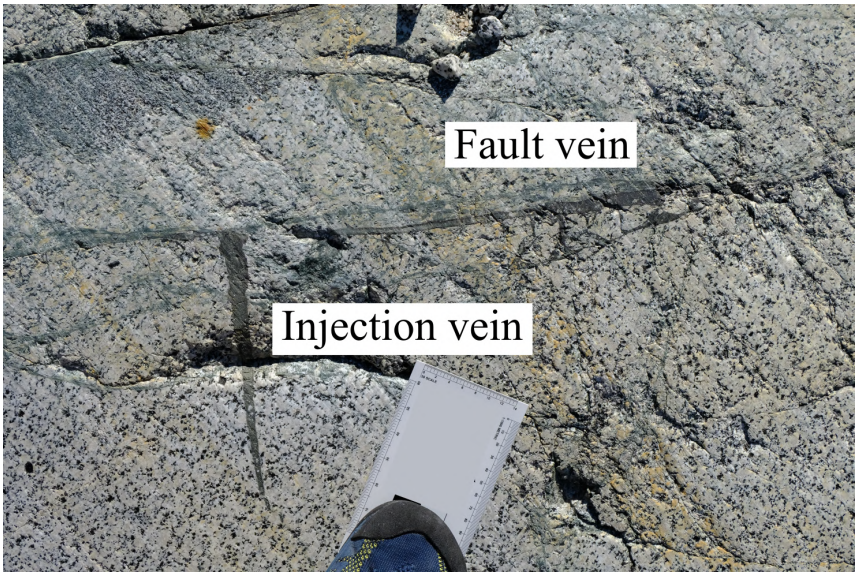

Figure 1.1: An example of a natural pseudotachylyte with a fault and injection vein from the Gole Larghe fault zone (Section 3.1.2).

$$\Delta T = \frac{2\tau \dot{u}\ \sqrt{t_{th}}}{c_p\ \rho \sqrt{\kappa \pi}} \tag{1.6}$$

With ΔT the temperature increase [K], τ shear stress [MPa], $\dot{u}$ on-fault slip rate $[\frac{m}{s}]$, t_{th} weakening time [s], c_p specific heat $[\frac{J}{K\ kg}]$, κ thermal diffusivity $[\frac{m^2}{s}]$.
The temperature increase ΔT is proportional to $\dot{Q}$ and may lead to rock melting, producing pseudotachylytes (Mckenzie and Brune, 1972). Currently, pseudotachylytes are the only rocks that testify the ancient seismicity of a fault (Cowan, 1999, Rowe and Griffith, 2015), and their occurrence has been widely studied to understand earthquake mechanics (for a review, see Di Toro et al., 2009).

1.2.2 Natural pseudotachylytes

A pseudotachylyte is a rock generated by melting of the fault slip zone during an earthquake. Based on their geometry, pseudotachylytes are distinguished in **fault veins** which decorate the main fault, and **injection veins** which depart from the main fault and intrude fractures in the wall rocks (Figure 1.1).
When an earthquake propagates at km/s and passes through a fault patch, the large stress perturbation (of the order of GPas) at the rupture tip results in pulverization, in-situ frag-

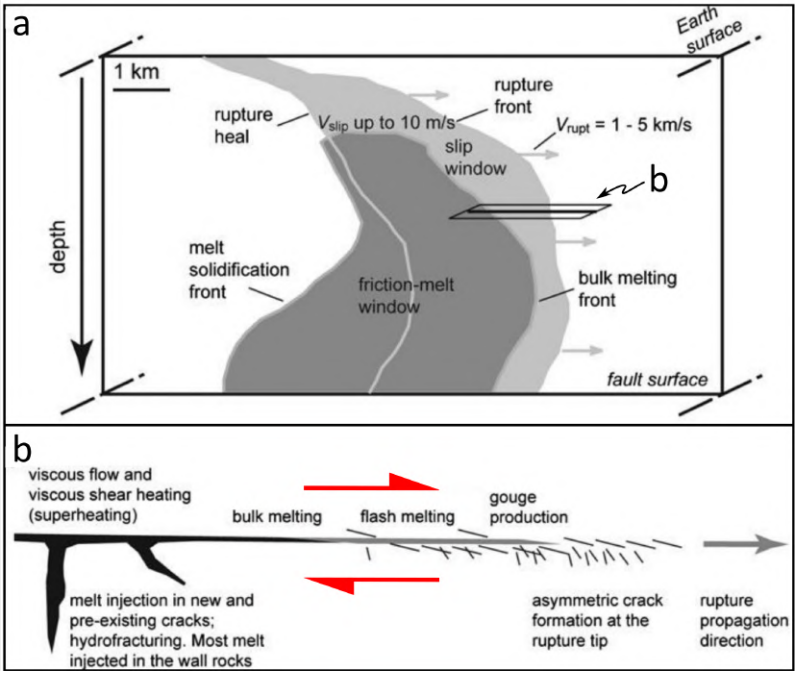

Figure 1.2: Representation of a fault plane during an earthquake (a) and horizontally oriented cross section of the same plane (b). The light gray zone is the fault area in motion, while the dark gray zone is the melt patch. Note that the melt does not appear as soon as the fault moves and persists also when slip is ceased, since it solidifies in minutes, while the earthquake usually lasts some seconds. Modified from Swanson (1991)

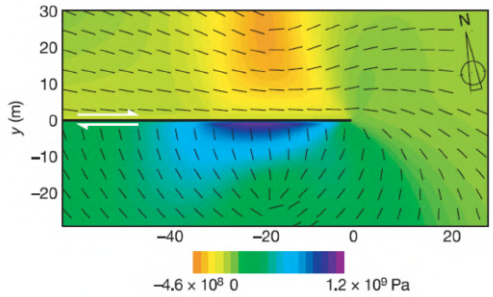

Figure 1.3: Numerical simulation of the stress perturbation induced by the transition of the crack tip, showing the direction of the maximum principal stress (marked by the small black lines). Rupture tip velocity $v = 0.9\ v_s$, where v_s is the Rayleigh wave velocity. Note that on the southern block the maximum stress is oriented perpendicular to the fault, thus generating a transient extensional stress that can produce mode I cracks perpendicular to the fault. These can be subsequently filled with friction melt. From Di Toro et al. (2005a)

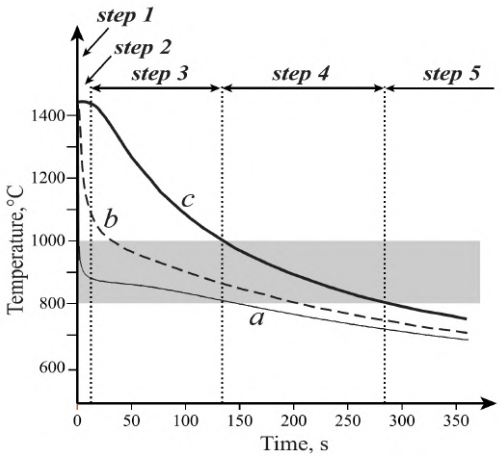

Figure 1.4: Temperature evolution during the cooling of a 24-mm thick pseudotachylyte at the contact with the host rock (a), at 1.8 mm from the vein wall (b) and in the vein center (c). The gray area is the crystallization window for plagioclase and biotite, step 1 is at Time=0 seconds. From Di Toro and Pennacchioni (2004)

mentation, cataclasis and wearing of the fault wall rocks (Figure 1.2, Swanson, 1991, Bestmann et al., 2012 and Bestmann et al., 2016). The rupture tip propagating along the fault causes also tensional cracking on one side of the fault (Figure 1.3, Di Toro et al., 2005a) These tension fractures can be intruded by the friction melt and become injection veins or, if not intruded, can be sealed and preserved as fluid inclusions trails (Griffith et al., 2010). It is still unclear what exactly determines the filling or sealing of cracks, though this is probably ruled by the elastic parameters of the rock.

After the passage of the rupture front and the initial melting of some fragments of the rupture-damaged rock, the fault slips further (if there is enough elastic energy stored) melting the host rock and generating a continuous melt layer that lubricates the fault, obtaining fault strengths up to one order of magnitude lower than those expected in a typical Byerlee frictional regime (Di Toro et al., 2006, Di Toro et al., 2011). When the slip stops, no more melt is produced and it cools down to ambient temperature due to heat conduction and radiation towards the host rock (melt solidification front in Figure 1.2). Melt cooling and solidification, at least in the studied faults of the Gole Larghe Fault Zone, is a strain hardening process that leads to a complete welding of the two rock walls making the fault tougher than the wall rock itself (Swanson, 1991, Di Toro and Pennacchioni, 2005, Mitchell et al., 2016).

The cooling history process of a circa 2 cm-thick pseudotachylyte (Figure 1.4) was described in Di Toro and Pennacchioni (2004) with the help of a numerical simulation and is here briefly summarized. Cooling can be subdivided into five steps:

- Step 1, 1-5 seconds from the beginning of the slip: during rupture propagation and the initial coseismic slip a gouge is produced and melted due to shear heating, reaching a temperature of 1450°C and generating flow structures.
- Step 2, 3-5 seconds after the earthquake: melt temperature drops more than 500°C, entering in the plagioclase and biotite crystallization window at the vein boundaries, where heterogeneous nucleation on relic clasts occurs.
- Step 3, 5 to 170 seconds after the earthquake: the crystallization of microlites in the external area of the pseudotachylyte proceeds with a high growth rate due to the high undercooling.

- Step 4, 130-140 seconds after the earthquake: the melt in the central part of the vein starts to crystallize plagioclase and biotite on large relic clasts, with the formation of spherulites.

- Step 5, after 280 seconds: the crystallization of biotite and plagioclase microlites is completed and a residual K-enriched, Ti-saturated melt precipitates k-feldspar and titanite grains.

In smaller veins the spherulitic domain does not develop because the melt cools too fast to allow the crystallization of large microlites.

1.2.3 Seismic frictional dissipated power and pseudotachylyte-wall rock micro-roughness

In Nielsen et al. (2010) the authors proposed a theoretical model that describes the variations in pseudotachylyte micro-roughness as a function of the frictional dissipated power, based on the selective melting of the rock forming minerals.
Silicate-built rocks are usually composed of different minerals, each one with different melting temperature (T_m). If there is an extremely fast increase in temperature (like in pseudotachylyte generation), melting does not occur at equilibrium; instead, low melting point minerals melt faster than high-melting point ones (Spray, 2010). Figure 1.5 shows a pseudotachylyte in an idealized gabbro, a rock composed mostly of plagioclase ($T_m = 1450$°C) and diopside ($T_m = 1400$°C). During melting, diopside is consumed faster than plagioclase, thus generating embayments where the boundary is made of the first mineral and protrusions when made of the second one.
The same reasoning can be applied to a granitoid rock, where biotite melts at 650-700°C, plagioclase at 1450°C and quartz at 1700°C. In fact, pseudotachylyte glass in tonalites has a considerably lower silica content with respect to the host rock (58% vs 66%, respectively) due to preferential melting of biotite (Di Toro and Pennacchioni, 2004). Another process that occurs at non-equilibrium melting is the Gibbs-Thomson effect: local melting temperature of minerals decreases with grain-melt interface curvature, so that edges are smoothed and rounded (Hirose and Shimamoto, 2005).

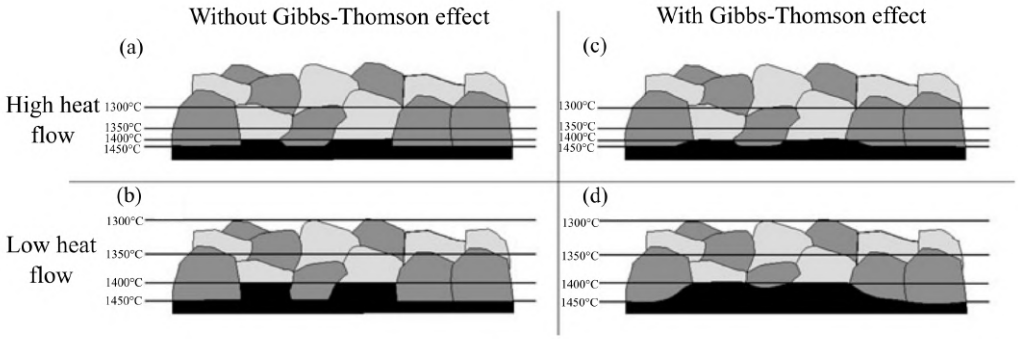

Figure 1.5: Idealized model of a melting boundary in a two-mineral rock (plagioclase, dark gray and diopside, light gray). In (a) and (b) melting strictly occurs according to the melting temperature of minerals, with a high and low heat flow, respectively. In (c) and (d) the Gibbs-Thomson effect is considered; thus the boundary is smoother due to preferential melting of edges. From Nielsen et al. (2010)

For a given wall rock grain size, the amplitude and wavelength of the boundary (or micro-roughness) at the pseudotachylyte-host rock contact depends on the temperature gradient perpendicular to the fault vein (Figure 1.5). For a high heat flux ($\dot{Q}$) the temperature gradient is high and, as a result, the boundary will be more planar. Instead, with a low heat flux, the temperature gradient is lower and the boundary rougher.

To quantitatively describe the relationship between micro-roughness evolution, selective or differential melting and frictional dissipated power, I introduce few geometrical parameters that characterize the pseudotachylyte-host rock boundary (Figure 1.6).

In fact, the boundary can be represented by N spherical caps of different radius λ with a probability distribution of height $\phi(z)$. Following Nielsen et al. (2010), the separation 2ω between two rough surfaces in function of the normal stress σ_N can be described as:

$$\frac{\omega}{\omega_0}^2 = 2\log\left(\frac{4}{3(1-\nu^2)}\left(\frac{\omega_0}{\lambda_{ave}}\right)^{3/2}\frac{E}{\sigma_N}\right) - 5\log\frac{\omega}{\omega_0} \tag{1.7}$$

Where ω_0, the characteristic asperities height, is the root mean square of the pseudotachylyte-host rock boundary height distribution $\phi(z)$, with z=0 being the reference height, defined so that $\int_R \phi(z)\,da = 0$ (where R is the considered fault area, Figure 1.6); ν is the Poisson ratio; E is the Young modulus and σ_N is the normal stress, which in the presence of a fluid between the two sliding walls (melt in the case of pseudotachylytes) can be further subdivided in:

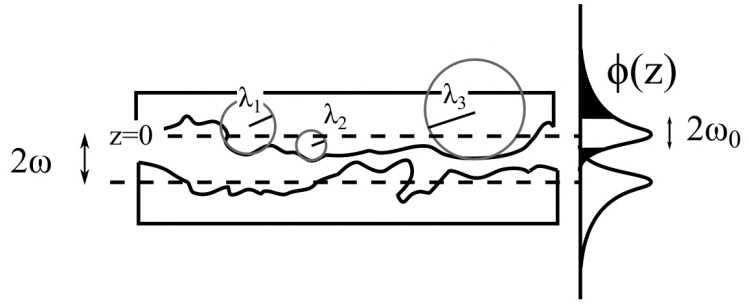

Figure 1.6: Representation of the roughness parameters analyzed in this thesis. 2ω is the pseudotachylyte melt thickness; $\phi(z)$ is the probability density function of asperities height distribution; ω_0 is the root mean square of $\phi(z)$; λ_{ave} is the average radius of the spherical caps that can be fitted on the surface. From Nielsen et al. (2010)

$$\sigma_N = \sigma_v + \sigma_0 = C\,\eta_e\,\dot{\omega}_c\,\frac{R^2}{\omega^3} + \sigma_0 \tag{1.8}$$

With σ_0 being the residual stress experimentally found in Nielsen et al. (2008); σ_v the viscous push exerted by the melt on the wall rocks; C is a geometric scaling factor; η_e is the apparent viscosity of the melt; $\dot{\omega}_c$ is the extrusion rate of the melt and R is the length of the melt patch (for discussion, see Nielsen et al., 2010).

In Nielsen et al. (2008) the authors argued that the thermal boundary (i.e. the distance where the temperature increase due to shear heating is not relevant) in a frictional melting environment at steady state, where the displacement is considerably smaller than the total contact length (i.e. fault length) is the following:

$$z_b = \frac{\kappa\rho(L + c(T_m - T_i))}{\tau\dot{u}} \tag{1.9}$$

Where κ is the thermal diffusivity, ρ is the density, L si the latent heat, c is the thermal capacity, T_m and T_i are the melt and initial ambient temperatures, respectively. This equation allows for the identification of the distance of the thermal boundary from the melting surface, that separates the rock portion affected by the temperature increase from the unaffected rock portion.

As shown in Figure 1.5, the micro-roughness of a melting surface with different minerals is controlled by the thermal gradient perpendicular to the fault. To determine it, it is necessary to know the temperature distribution in the host rock when a pseudotachylyte is being produced. In Nielsen et al. (2008), the authors derived the following temperature

distribution for a melt-producing fault at steady state:

$$T = (T_m - T_i)e^{-xv/\kappa} + T_i \tag{1.10}$$

Where x is the distance from the pseudotachylyte-wall rock boundary and v is the melting rate of the host rock:

$$v = \frac{\tau_{ss}\dot{u}}{\rho(L + C(T_m - T_i))} \tag{1.11}$$

With Equations 1.10 and 1.11 we will be able to determine the frictional dissipated power of some samples, by assuming that melting on biotite occurred up to the distance of the 800-1200°C isotherms (Section 5.2).

1.2.4 Frictional dissipated power on natural faults

To test whether the theoretical model described in Section 1.2.3 is suitable for natural faults, I needed to compare pseudotachylyte-wall rock samples from fault areas with different dissipated power. As frictional dissipated power is $\dot{Q} = \mu\ \sigma_N\ \dot{u}$, to get different values on the same fault there has to be at least a change in normal stress (σ_N), since we assume that $\dot{u}_{(t)}$ and $\mu_{(t)}$ are similar during the same slip event along the same fault (see Section 1.2.5 and Griffith et al., 2010 for discussion).

Wavy faults (Figure 1.7) present bends along slip that strongly affect the slip evolution of the fault and, in some cases (but probably not those presented here as the studied faults are decorated by a continuous layer of melt), can stop the rupture propagation (Nielsen and Knopoff, 1998, d'Alessio and Martel, 2004, Kame et al., 2003). It is therefore of primary importance to understand how fault orientation with respect to the far stress field affects slip dynamics.

1.2.5 Stress state on wavy faults

Stress distribution on wavy faults is not homogeneous and determines the processes acting on the fault during slip (Griffith et al., 2010). Figure 1.8 represents a numerical simulation of the stress, temperature and friction coefficient distribution on a wavy fault (L05, which

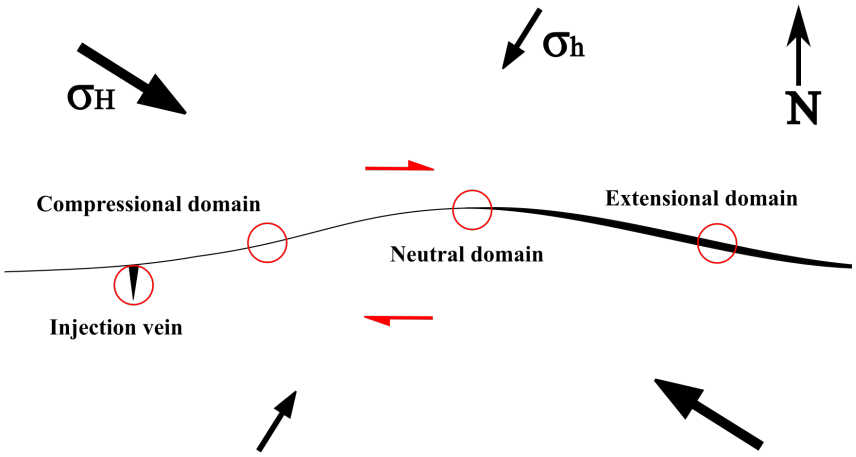

Figure 1.7: Idealized dextral wavy fault with compressional, neutral and extensional domains and an injection vein. The red circles are the ideal sampling sites to get different frictional dissipated power. Bends are exaggerated with respect to the studied faults, to better show fault bending.

is one of the faults analyzed in this thesis) performed in Griffith et al. (2010), showing how the maximum principal stress is perpendicular to the fault on compressional bends (those with highest σ_N) and parallel on extensional bends (with the lowest σ_N). One of the most important consequences of the stress distribution, visible in Figure 1.8, is that most of the melting occurs on contractional bends, since there is a higher normal stress (and therefore a higher τ, Nielsen et al., 2008); on the extensional bends the fault opens, as proved by melt pooling and by the maximum compressive stress parallel to the fault, so that frictional melting occurs in limited quantity or does not occur at all on these portions of the fault (Figure 1.8, Griffith et al., 2010, Nielsen et al., 2010).

Because of the stress gradient between contractional and extensional jogs and because of injection veins, the melt is mostly extruded from the source areas so that extensional bends act as ”melt pools”, while in contractional bends there is only a thin layer of melt because of the high normal stress squeezing away the melt. Moreover, the local stress field rotation directly reflects on the rock with the formation of micro-cracks parallel to the maximum stress, visible as inclusions trails in quartz crystals (Griffith et al., 2010). As discussed in this thesis, the formation of micro-cracks has a great influence on the micro-roughness, since crack orientation and fracture density of the rock determines its

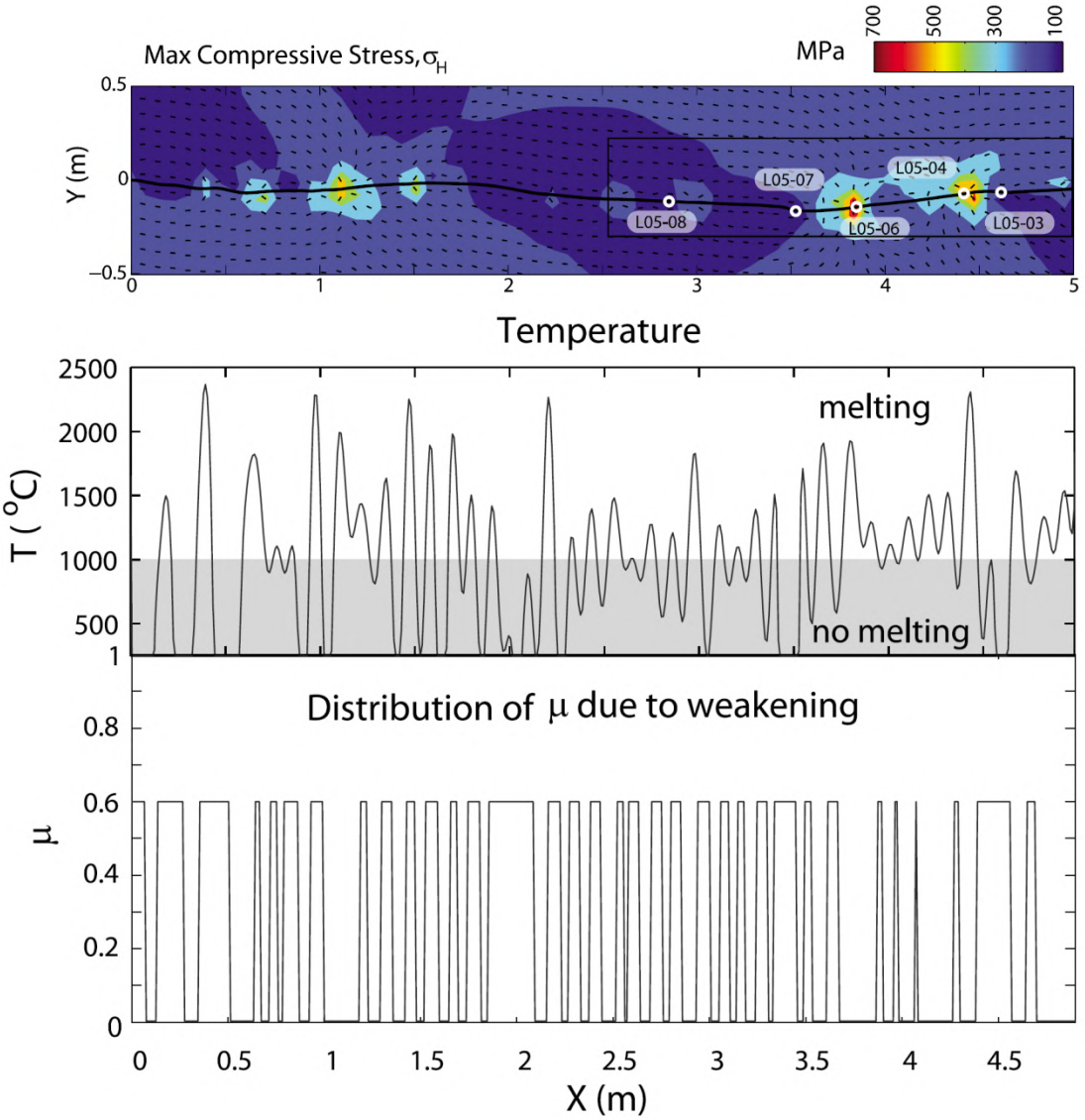

Figure 1.8: Results of the numerical model performed in Griffith et al. (2010) based on a right-lateral wavy fault from the Lobbia outcrop (L05). From top to bottom: maximum principal stress; temperature increase on the fault plane; friction coefficient during slip: μ is 0.0 if there is melting ($T > 1000$°C) and μ=0.6 if there is no melting ($T < 1000$°C). See text for description. From Griffith et al. (2010)

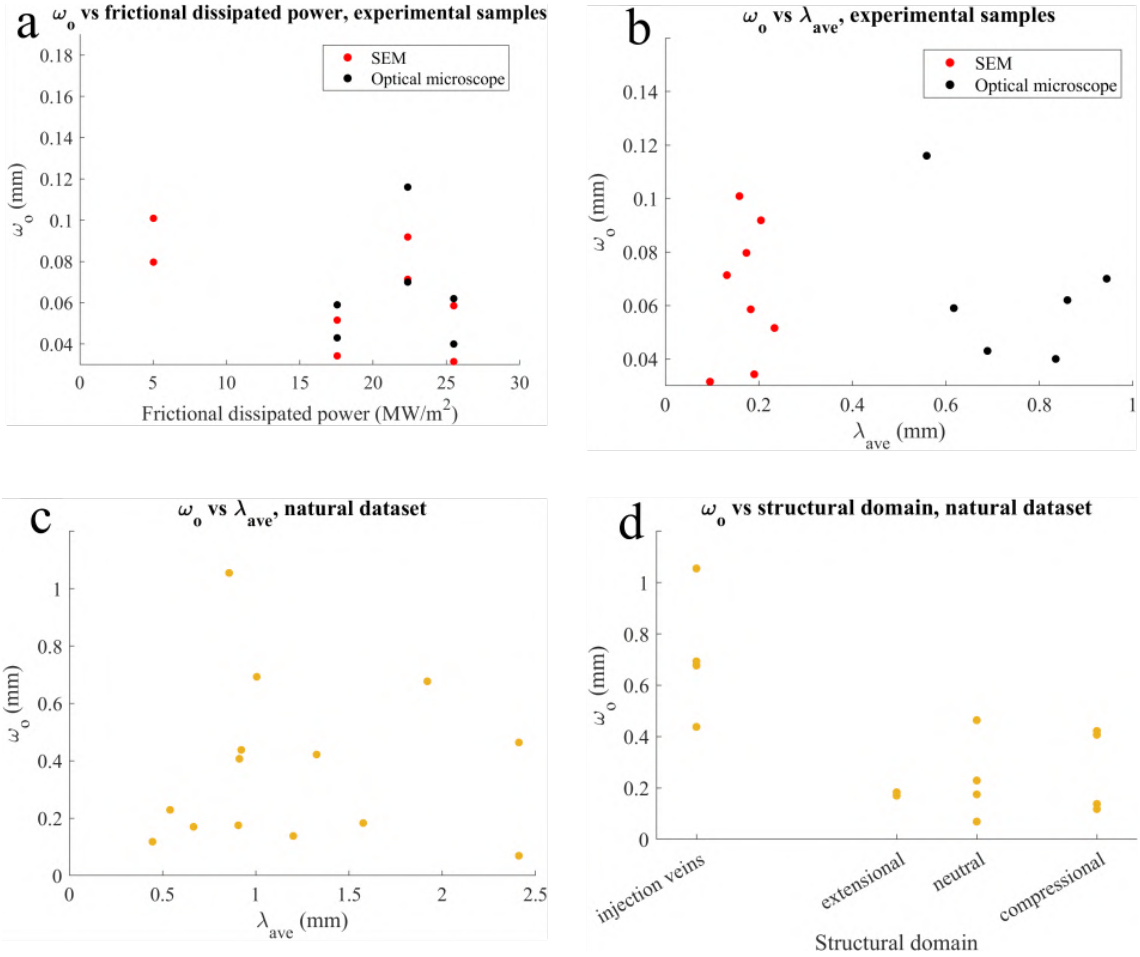

Figure 1.9: (a) ω_0 versus $\dot{Q}$ in experimental pseudotachylytes. Characteristic asperities height decreases with increasing frictional dissipated power; (b) ω_0 versus λ_{ave} in experimental pseudotachylytes. Note the difference in λ_{ave} between SEM and optical microscope-derived measurements; (c) ω_0 versus λ_{ave} in natural samples. There is an inverse trend, though the scatter is significant; (d) ω_0 versus structural domain in natural pseudotachylytes. As for experimental data, characteristic asperities height decreases with increasing dissipated power. All the data are from Castagna (2012)

resistance to mechanical wear during slip and the possibility of wall rock fragments to be ripped out during sliding and to be carried in the friction melt.

1.2.6 Preliminary studies on seismic frictional dissipated power

As stated in section 1.1, Castagna (2012) attempted at estimating frictional dissipated power using pseudotachylyte-wall rock micro-roughness with encouraging results. In her work, dedicated experiments were performed with increasing frictional dissipated power to constrain the micro-roughness for a given $\dot{Q}$. This was obtained with SHIVA, a powerful rotary shear experimental machine (Di Toro et al., 2010) that allows the sliding of two

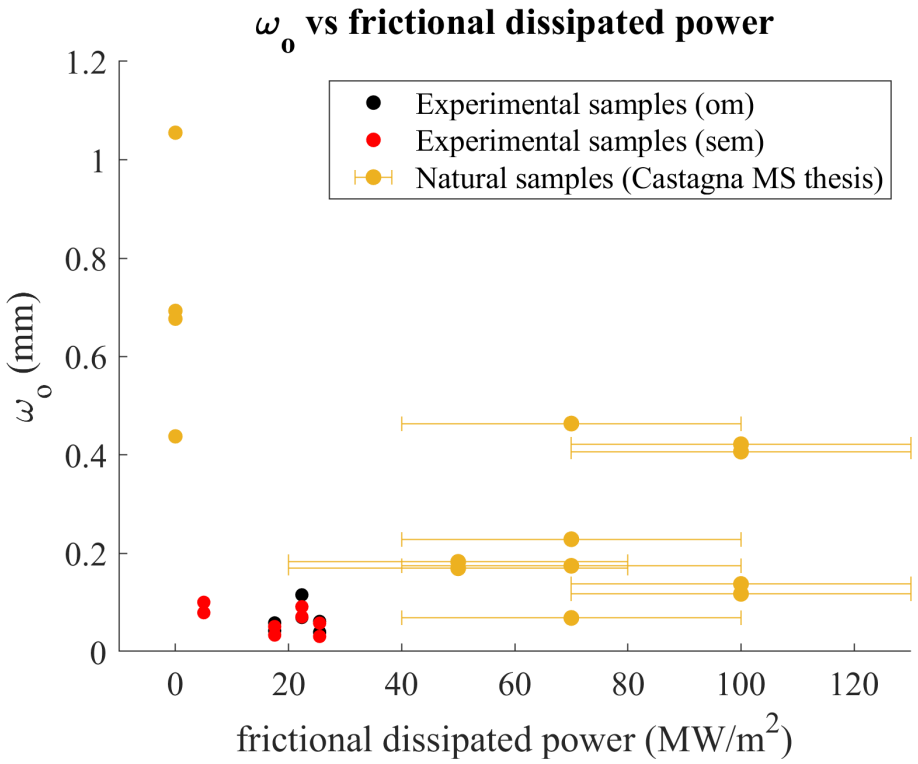

Figure 1.10: ω_0 versus frictional dissipated power in both natural and experimental samples. The large error is due to the assumptions presented in section 1.1. From Castagna (2012)

samples (50 mm in diameter) at a slip rate between 10 $\frac{\mu m}{s}$ and 9 $\frac{m}{s}$, with a normal stress of up to 50 MPa. In Castagna (2012), 3 experiment were performed on tonalite (the same rock found in the Gole Larghe Fault Zone, see section 3.1.2) with a slip rate of $6,5\ \frac{m}{s}$ and increasing normal stresses of 20, 30 and 40 MPa, which led to 17.55, 25.5 and 22,36 $\frac{MW}{m^2}$, respectively, of frictional dissipated power at steady state. She also analyzed an experiment carried out in Di Toro et al. (2006), performed at 1.3 $\frac{m}{s}$ and 20 MPa, always on tonalite, which led to a frictional dissipated power at steady state of $5.02 \pm 0.15\ \frac{MW}{m^2}$. These slip rates and normal stresses lead to the melting of the fault, producing an artificial pseudotachylyte.

The micro-roughness data calculated from the experimental pseudotachylyte - wall rock boundaries showed that ω_0 decreased with increasing frictional dissipated power (Figure 1.9a), while there was no relationship between λ_{ave} and ω_0 (Figure 1.9b). However, Castagna (2012) found that λ_{ave} was systematically higher when the micro-roughness was measured with the optical microscope (OM) rather than with the scanning electron microscope (SEM) (Figure 1.9b, see Castagna, 2012 for discussion).

In the aforementioned work were also analyzed 7 natural samples to estimate the frictional dissipated power in natural pseudotachylytes, based on the experimental data calibration. Natural data showed a consistent trend with experimental ones regarding the relationship between ω_0 and frictional dissipated power (Figure 1.9d); in natural pseudotachylytes there is also an inverse trend between λ_{ave} and ω_0 (Figure 1.9c), not found in experimental samples.

An approximative estimate of the frictional dissipated power in natural pseudotachylytes can be done with some strong assumptions such as slip rate and friction coefficient during slip (see Griffith et al., 2010 and Castagna, 2012 for discussion), that lead to values of 0, 50, 70 and 100 $\frac{MW}{m^2}$ for injection veins, extensional, neutral and compressional domains respectively, with a $\pm$30 MPa error. Even with such an important error, a comparison between natural and experimental samples was done (Figure 1.10). From Figure 1.10 it appeared that characteristic asperities height in experimental samples is 3 to 10 times smaller than ω_0 in natural samples.

This was probably caused by the different scale between experimental and natural faults (about 15 cm versus several meters at least) and by the polishing of experimental samples (to avoid mechanical complications during the experiment), which did not occur in natural pseudotachylytes (Castagna, 2012).

Chapter 2

Methods

In this thesis, I used various methodologies to determine the micro-roughness of the pseudotachylyte-host rock boundary from natural pseudotachylytes as follows:

1. natural pseudotachylytes were sampled from selected faults of the Gole Larghe Fault zone (Adamello Massif, Southern Alps, see section 3.1.2);
2. samples were cut into 30 μm-thick polished thin sections;
3. thin sections were digitally scanned;
4. pseudotachylyte-host rock boundaries were manually drawn from the digital images;
5. drawn profiles were analyzed with a MATLAB®script (see Appendix A).

2.1 Field sampling methods

Pseudotachylytes were sampled from the Gole Larghe fault zone in the Adamello batholith (Southern Alps, Section 3.1), where thousands of pseudotachylyte-bearing faults are exposed. A field survey was carried out from September, 1^{st} to 8^{th} 2020 (during COVID-19 pandemics) to identify and sample pseudotachylyte-bearing faults based on the following characteristics:

- good outcrop exposure that allowed me to identify fault bends and to recognize one of the four structural domain (see Figure 1.7) together with fault dip and dip angle;

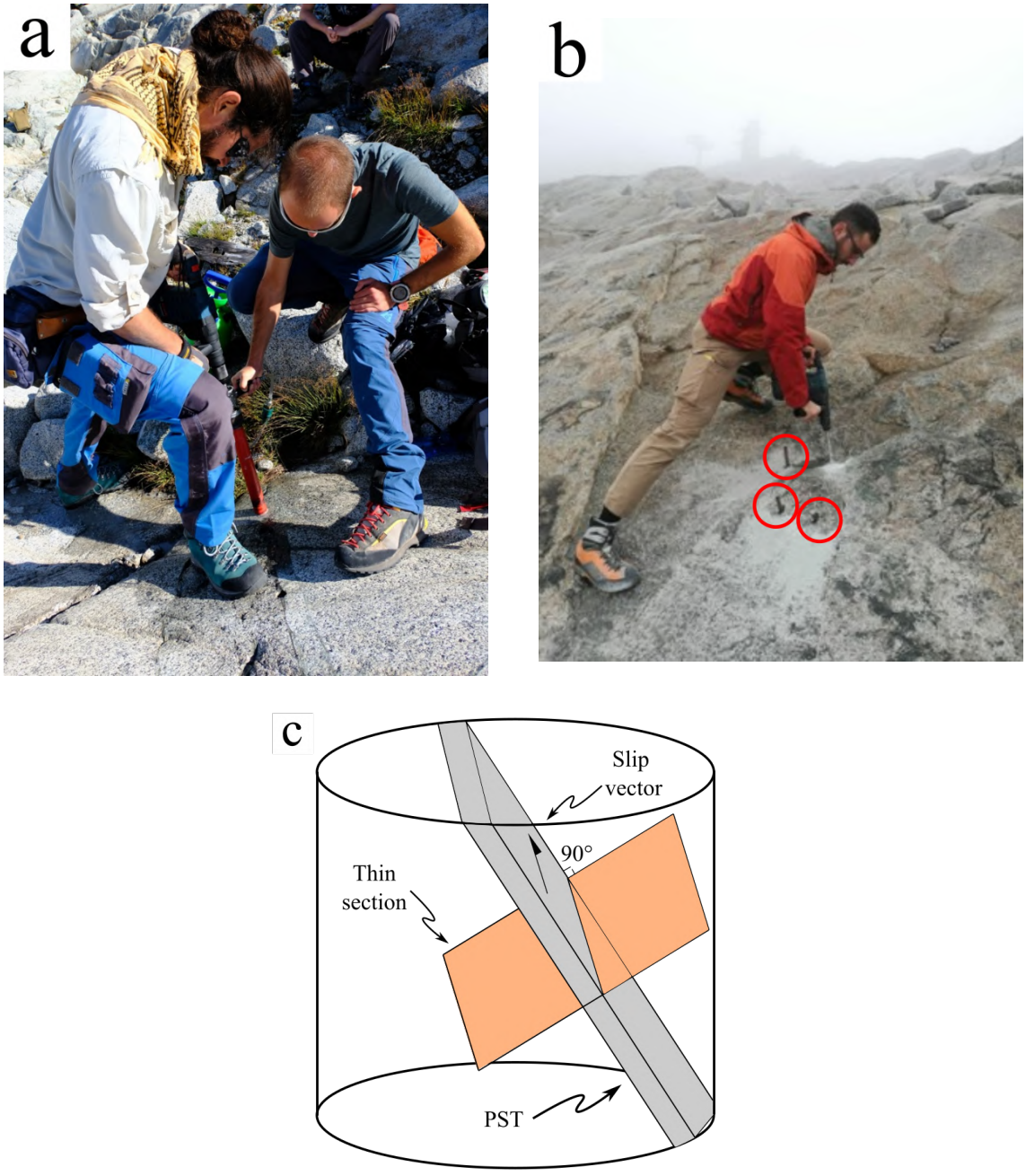

Figure 2.1: From outcrop sampling to thin section preparation. (a) sampling with core drill; (b) sampling with block extractors (red circles); (c) thin section orientation with respect to the pseudotachylyte (PST).

- presence of lineations on the fault surface to determine the slip vector, for an accurate determination of the micro-roughness of the pseudotachylyte-host rock boundary;
- absence of cataclasites juxtaposed to the pseudotachylyte;
- presence of a marker to assess the fault separation.

Six faults were selected and sampled with a core drill or block extractors. Samples were classified accordingly to their structural position along the fault as injection veins, compressional, neutral or extensional domain along the fault vein (see Figure 1.7 and Figure 2.1).

2.2 Determination of the pseudotachylyte-host rock micro-roughness

From the samples obtained in the field, five were cut with a diamond saw, oriented parallel to the slip vector and perpendicular to the fault surface. This orientation allowed me to study microstructural features oriented parallel to the sense of shear (Figure 2.1c). Microstructural investigations were then carried out with a standard transmission optical microscope with polarized lenses.
The thin sections were scanned to obtain digital images with a resolution of 10 μm. The pseudotachylyte-host rock boundary (or micro-roughness or profile) was drawn on these digital images.

2.2.1 Pseudotachylyte/host rock boundary drawing procedure

I traced 56 experimental and natural pseudotachylyte-host rock boundaries using a vector graphics software (Inkscape®) with a 10 μm resolution. Between these, to avoid biases due to different drawing methods, I also redrew the natural and experimental (SEM and OM for the latter) pseudotachylyte-host rock boundaries of the samples discussed in the previous study of Castagna (2012).
For the correct utilization of the MATLAB®script required for the analysis of the micro-roughness (section 2.2.2), I followed this procedure:

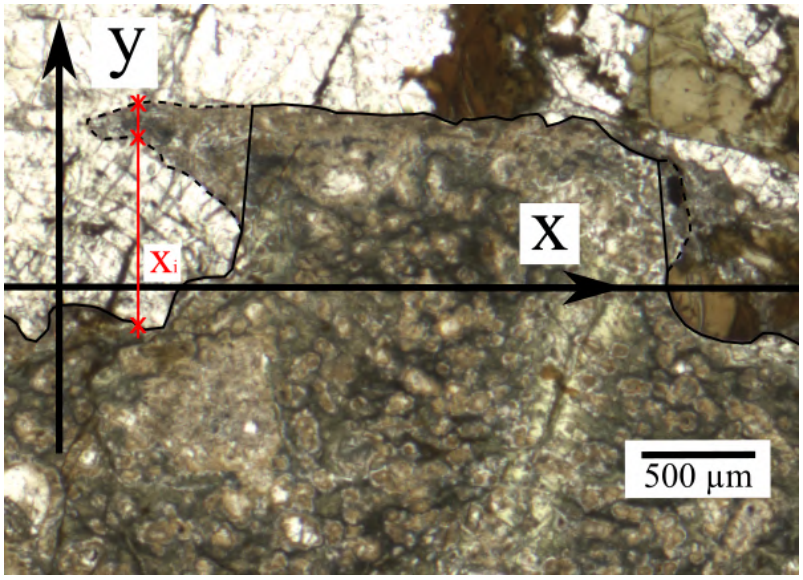

Figure 2.2: Example of an embayment. The horizontal line is the x axis, that is determined linking the two end points of the profile. The y axis is perpendicular to the x axis. The thin, black solid line is the drawn boundary, while the dashed line is the real boundary. The red line indicates a generic x_i coordinate, red crosses show the boundary points with the same x coordinate.

1. in Inkscape®, I scaled the digital scans so that they had the length and width of the real thin sections, in this way the length of the drawn boundary matches the length of the real one;

2. I rotated the scans of the thin sections so that the two end points of the pseudotachylyte-host rock boundary laid on a horizontal line, the x axis (Figure 2.2);

3. if the x axes of two opposite pseudotachylyte-host rock boundaries were not parallel (in fact, the pseudotachylytes are sandwiched between the two host rock walls), I rotated one of the two boundaries and its x axis to obtain parallelism.

4. drawing of the micro-roughness was carefully carried out following the pseudotachylyte-host rock boundary after verifying under the optical microscope ambiguous contacts between the pseudotachylyte and the host rock (i.e., sometimes the pseudotachylyte matrix has a similar color as the biotite or as some cataclasites in the host rock);

5. since the MATLAB®script works correctly if there are unique values of y with respect to x (see section 2.2.2), embayments were cut, when required, with a line almost perpendicular to x (but not at a 90°angle, since then there would be 2 points with the same x value, Figure 2.2);

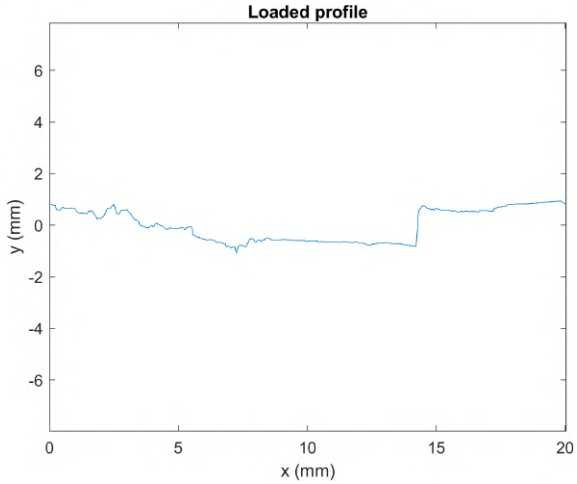

Figure 2.3: Loaded pseudotachylyte-host rock boundary.

6. when all the micro-roughness profiles were drawn in .svg format, they were first converted into .dxf format (CAD files) within Inkscape®, and eventually in .xyz files (raw coordinates) with the open source program "Dxf2xyz".

2.2.2 MATLAB®script for the determination of micro-roughness parameters ω_0 and λ_{ave}

A MATLAB®script to calculate the main micro-roughness parameters ω_0 and λ_{ave} (i.e., the root mean square of the height distribution (y) of the pseudotachylyte-host rock boundary and the average radius of the spherical caps fitting on the asperities, respectively; Figure 1.6) was used in Castagna (2012). However, the script required a series of improvements as the output parameters ω_0 and λ_{ave} were not consistent with the actual pseudotachylyte-host rock boundary micro-roughness. This revised script is attached in Appendix A.
Here I will describe the main steps required for the calculation of the micro-roughness parameters:

Step 1: Loading the drawn micro-roughness files

The first step is to load the .xyz file containing the coordinates of all the points of the drawn pseudotachylyte-host rock boundary. I wrote three different loading methods:

1. single file loading, to calculate the micro-roughness parameters for only one boundary or to check that the script is working correctly;

2. multiple file loading (case for natural pseudotachylytes), to load all the 42 natural profiles in one step thus reducing analysis time;

3. multiple file loading (case for experimental pseudotachylytes).

I wrote two separate loading modes for natural and experimental micro-roughness because experimental samples analysis was carried out both at the OM and SEM (Castagna, 2012), so that for each experimental sample there are 4 drawn host rock-pseudotachylyte boundaries, two for the SEM scan and two for the OM scan, while natural pseudotachylytes were only scanned with the optical microscope, so that for each natural pseudotachylyte there are two boundaries. A single loading method could be created, though I preferred to keep the script as simple as possible.
At this point, the pseudotachylyte-host rock boundary is plotted to check whether the loading process was correctly completed (Figure 2.3).

Step 2: micro-roughness profile elaboration

First, a reference value y_{ref} is calculated as the average height of the whole profile (average of all y values, Figure 2.2), then the deviation from the reference is calculated for all points as: $z = y - y_{ref}$. The elevation of the profile from the reference value is z instead of y to differentiate the original drawn pseudotachylyte-host rock boundary ($x - y$) from the elaborated profile ($x - z$).
At this point, ω_0 can be determined from the distribution of height of the boundary (i.e., the distribution of z; Figure 2.4a).
In the original version of the script (Castagna, 2012) at this stage a filter was introduced to remove the short wavelength asperities (under 50 μm). Then, the profile was interpolated to a regularly-spaced x axis. However, as discussed below, I realized that this filtering step introduced a critical bias.
Drawing of vertical steps was carefully avoided (section 2.2.1; Figure 2.4c) to reduce the risk of any bias during the micro-roughness parameters determination. In Figure 2.4b I reported the filtered and interpolated profile. With respect to the original boundary in Figure 2.3, this step deeply modified the profile because of the introduction of vertical section of the profile after the filtering phase (red circles in Figure 2.4d; for a comparison

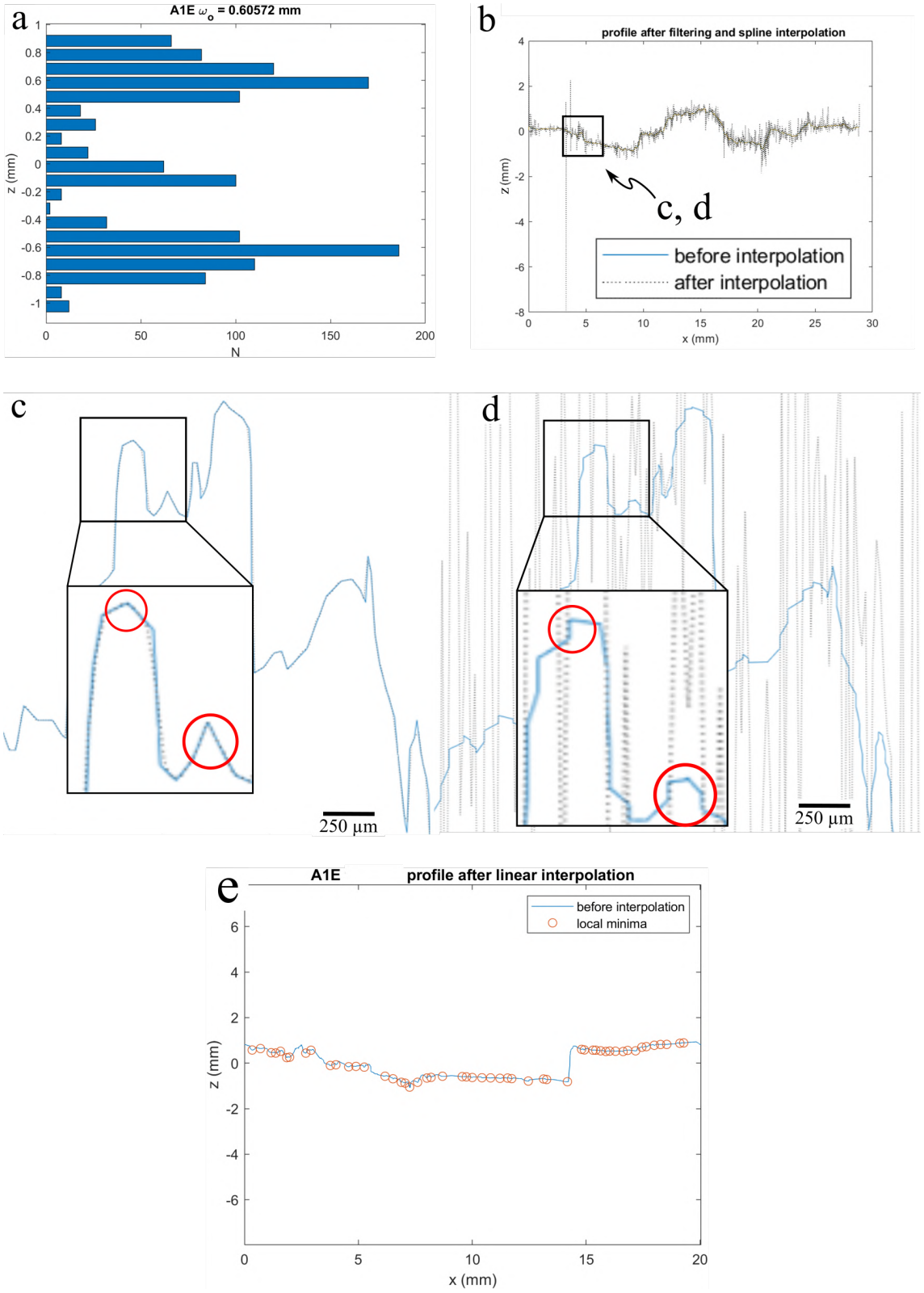

Figure 2.4: Profile elaboration steps. (a) profile distribution of height (z) with the value of ω_0 in the title of the histogram; (b) profile after filtering and interpolation; (c) detail of the original non-filtered (blue line) and interpolated profile (black dashed line), in the enlarged area there are no vertical sections (red circles); (d) detail of the filtered (blue line) and interpolated profile (black dashed line), in the enlarged profile area, the same as the one in figure c, there are vertical sections (red circles); (e) local minima position on the profile.

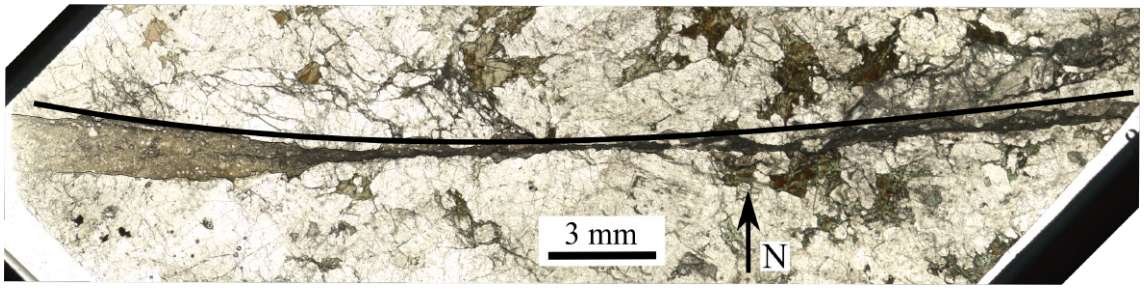

Figure 2.5: Example of a pseudotachylyte-host rock boundary with the influence of macroscopic roughness, not related to melting processes. The black solid line represents the largest circular (spherical in 3D) cap fitting the northern profile

with the original drawn profile see red circles in Figure 2.4c). These vertical sections cause the over-and undershooting of the interpolation (black dashed line in Figure 2.4b and d) that results in an unrealistic profile. Without the filtering phase, the interpolation almost perfectly matches the original profile (enlargement in Figure 2.4c).
Given the spurious data introduced by the utilization of the filter that finally results in unrealistic ω_0 and λ_{ave} values, I decided to exclude the filter from the micro-roughness analysis.

Micro-roughness curvature parameters

Once the micro-roughness profile was interpolated into a regularly-spaced x axis, the curvature parameters can be calculated. Since λ_{ave} is the average radius of the spherical caps fitting the asperities, the script first needs to identify the position of the local maxima and minima along the profile (Figure 2.4e). Then, x and z curvature components between each adjacent maxima and minima (kX and kZ) are calculated as the second space derivative of x and z shifts between maxima and minima (dX and dZ). The radius R of the spherical cap fitting each asperity can be derived as:

$$R = \frac{1}{\sqrt{kX^2 + kZ^2}} \tag{2.1}$$

Since the micro-roughness analysis is performed to understand the effects of differential melting on the pseudotachylyte-host rock boundary, when calculating λ_{ave} larger values of R related to the macroscopic roughness of the pseudotachylyte (Figure 2.5) must be discarded. For this reason, λ_{ave} is calculated as the average of all R$<$1 mm, which is

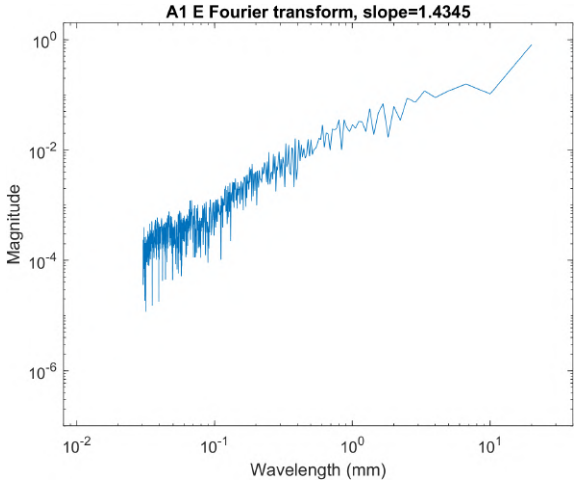

Figure 2.6: Fourier transform spectrum of sample A1, eastern boundary, plotted on a log-log plane. The black solid line represents the linear fit of the spectra.

approximately the upper limit of the curvature radius of profile oscillations caused by differential melting (sections 4.1 and 5.1).

Fourier transform analysis of the micro-roughness

To further test if the micro-roughness wavelength varied with frictional dissipated power, I performed a Fourier transform analysis of the micro-roughness profiles implementing the same script used to determine ω_0 and λ_{ave}.

The Fourier spectrum for each measured profile was then saved as a .txt file and plotted in MATLAB®(Figure 2.6).

To make the entire micro-roughness analysis more efficient and for a direct comparison of the 56 pseudotachylyte-host rock boundaries, I automatized several processes. This automatized procedure includes the loading of all the natural or experimental profiles together as well as the plotting and saving of an overview figure with the thin section digital image, the profile I traced, the distribution of profile height with ω_0 and the Fourier spectrum with the slope of the regression fit line (Figure 2.7; the entire dataset is reported in Appendix B). I also automatically created an Excel spreadsheet with the pseudotachylyte-host rock boundary name, the calculated ω_0, λ_{ave}, Fourier spectra linear regression fit slope and intercept.

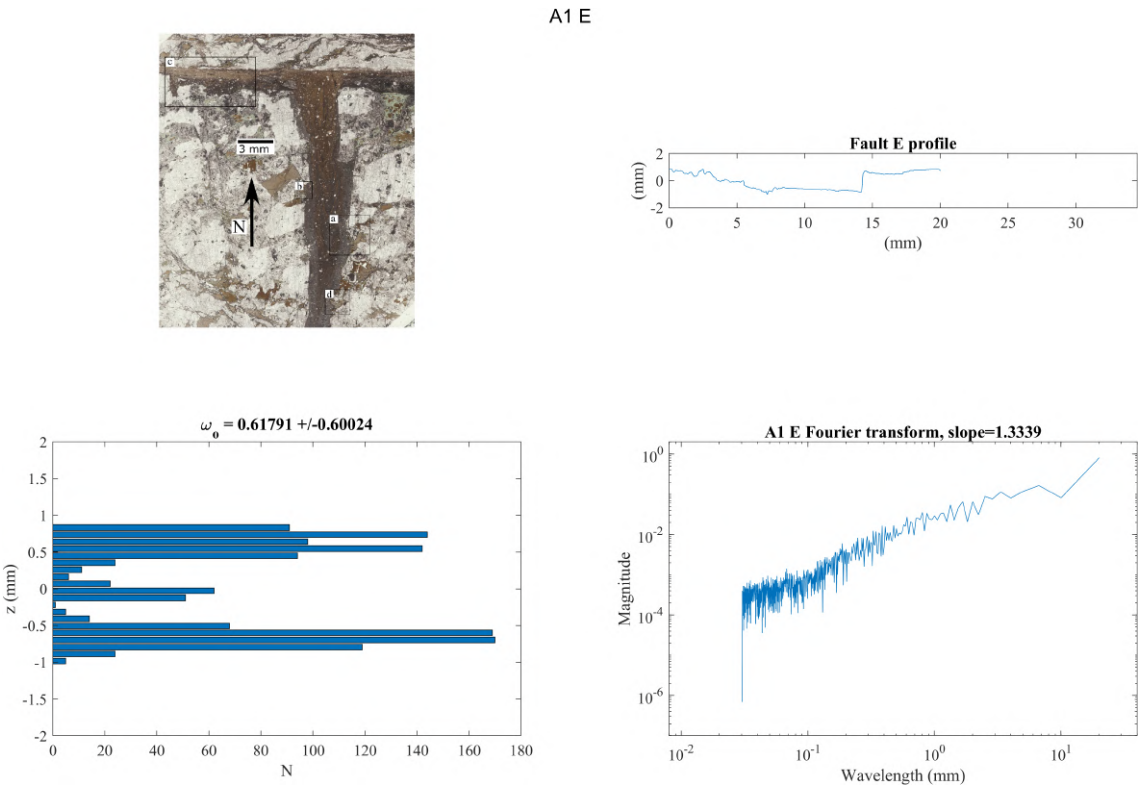

Figure 2.7: Overview image of the eastern pseudotachylyte-host rock boundary of sample A1

Chapter 3

Geological setting

The natural pseudotachylyte samples discussed in this thesis were collected from the Gole Larghe fault zone (Adamello batholith, Southern Alps, Italy). A geological introduction to the area is presented below, as well as the ambient conditions during seismic faulting associated to the formation of the studied pseudotachylytes.

3.1 Regional setting

3.1.1 The Adamello batholith

The Adamello batholith is the largest magmatic intrusion related to the Alpine Orogeny (670 km^2 of exposed rock, Callegari and Brack, 2002). The batholith is a subduction-related intrusion (Ji et al., 2019) enclosed between the Giudicarie and Tonale lines and intruded the crystalline basement and covers of the Southern Alps (Figure 3.1a).
The main rocks composing the batholith are tonalites with minor granodiorites, leuco-tonalites, diorites and gabbros (Callegari and Brack, 2002; Schaltegger et al., 2019).
The batholith is composed by four main plutons (each pluton is composed by several individual plutons) emplaced at ages decreasing from south-west to north-east (Figure 3.1a; Brack, 1981; Brack, 1985; Stipp et al., 2002; Callegari and Brack, 2002; Stipp and Fügenschuh, 2004; Schaltegger et al., 2019)

I Re di Castello-Corno alto pluton (40-42 Ma), composed of medium to fine-grained biotite and horneblende-bearing tonalites to granodiorites;

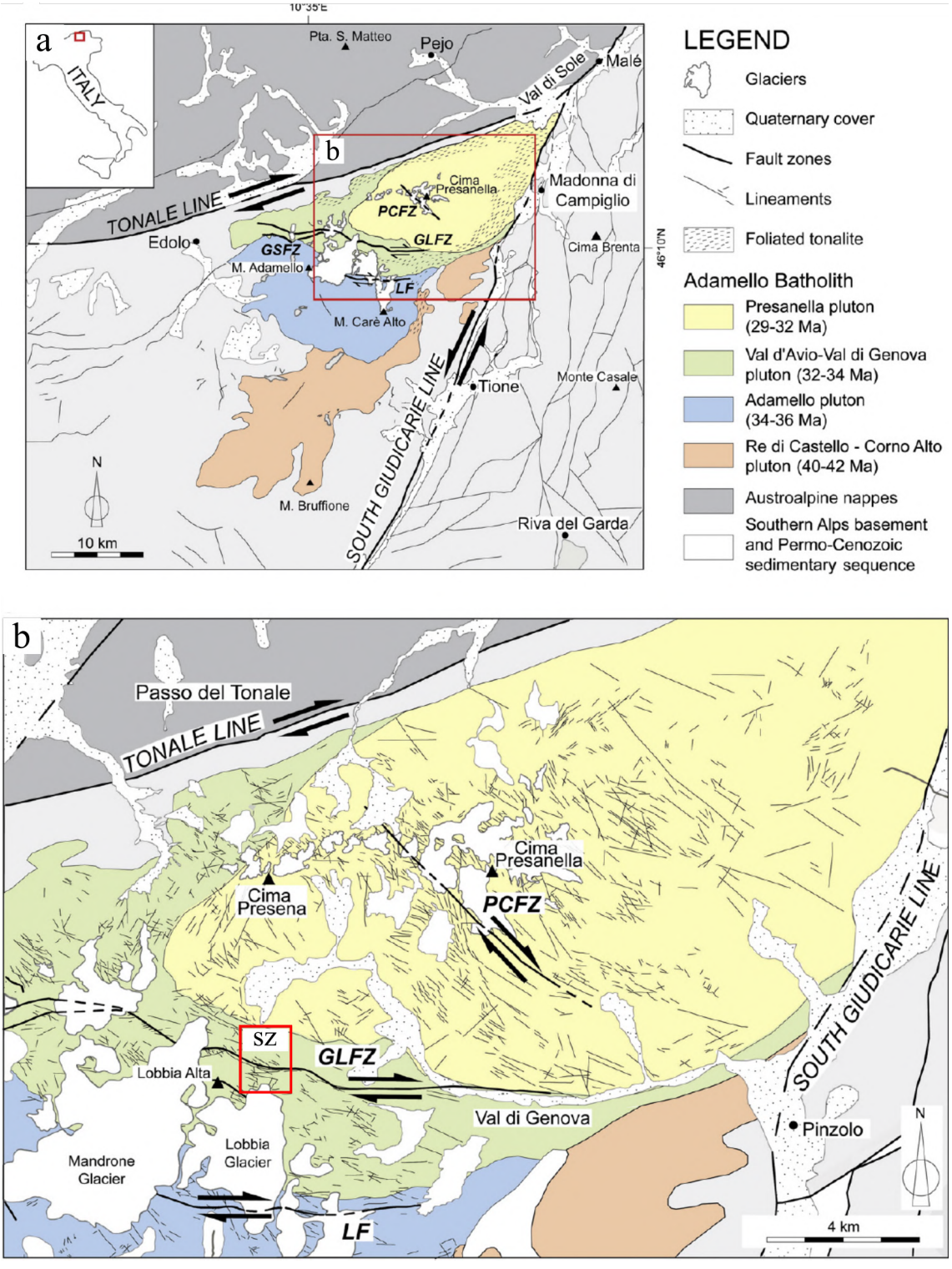

Figure 3.1: (a) Geological map of the Adamello batholith, with the four main plutons. Near the Tonale and Giudicarie lines the intrusion is foliated. (b) detail of the northern portion of the Adamello batholith, where the studied fault zone is (red box). GLFZ and GSFZ: Gole Larghe and Gole Strette fault zones; PCFZ: Passo Cercen fault zone; LF: Lares fault. The samples analyzed in this thesis were collected from the GLFZ, (red box, sz). From Mittempergher et al. (2009)

II Adamello pluton (36-34 Ma), made of coarse-grained biotite and horneblende bearing tonalites to leucotonalites;

III Val d'Avio- Val di Genova pluton (34-32 Ma), made of biotite and quartz-bearing diorites to medium-grained biotite-bearing tonalites;

IV Presanella pluton (32-29 Ma), made of horneblende- and biotite-bearing tonalites.

The batholith emplacement mechanism has been debated for a long time and several regional studies have been carried out to describe emplacement-related structures (for a review, see Callegari and Brack, 2002 and Schaltegger et al., 2019).
Both the northern and eastern border of the Adamello batholith have a magmatic foliation, overprinted by ductile and brittle deformative events associated to the Tonale and Giudicarie lines, which occurred both during and after the cooling of the intrusion (Stipp et al., 2002; Stipp and Fügenschuh, 2004; Schaltegger et al., 2019). The southern border of the batholith (i.e., Re di Castello) has evidence for stopping and ballooning, as suggested by the presence of inward-dipping strata at the contact with the host rock, big sunken blocks inside the batholith and radial flattening at intrusion margins (Brack, 1985; John and Blundy, 1993).
Geochemical studies on the country rocks suggest an ambient temperature before the emplacement of the batholith lower than 300-350°C, since there is no evidence for Rb/Sr resetting after sediment deposition (Martin et al., 1996).
Petrological studies indicate ambient pressures during batholith emplacement to be between 200 and 350 MPa (Riklin, 1983; John and Blundy, 1993), without significant differences between the northern and southern areas suggesting that the whole batholith has not tilted nor vertically deformed.
Assuming an average rock density of 2650 kg/m^3, a depth intrusion of 9-11 km can be inferred (see discussion in Di Toro and Pennacchioni, 2004).

3.1.2 The Gole Larghe fault zone

The Adamello batholith is cut by several faults. Within these, the Gole Larghe fault zone (GLFZ) is the most studied (Figure 3.1b; Di Toro and Pennacchioni, 2004; Di Toro and Pennacchioni, 2005; Pennacchioni et al., 2006; Griffith et al., 2010; Bistacchi et al., 2011;

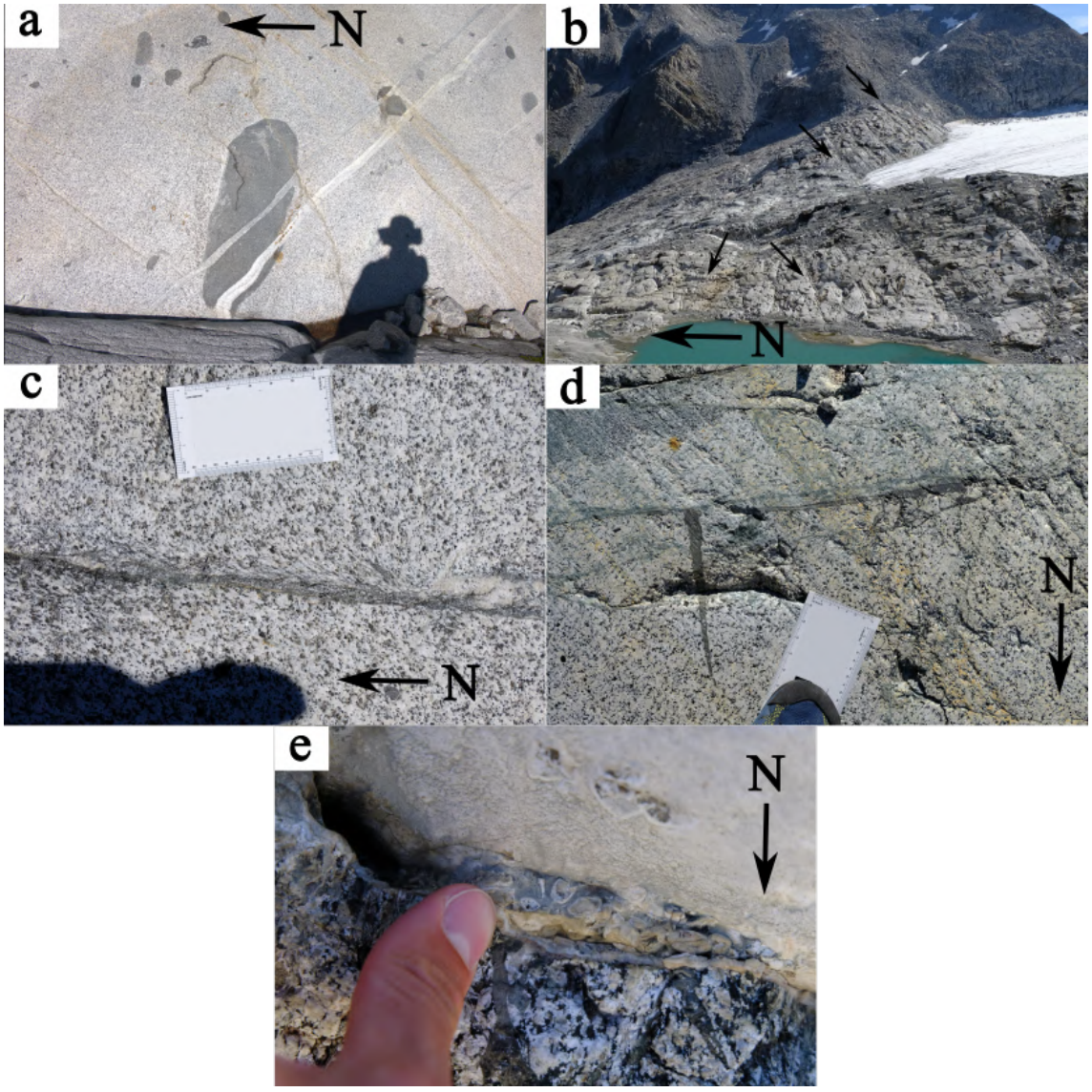

Figure 3.2: The five main deformative structures found in the GLFZ: (a) late-magmatic foliation and folding; (b) joints; (c) mylonites; (d) pseudotachylytes and green cataclasites; (e) zeolite-bearing faults.

Smith et al., 2013; Dempsey et al., 2014; Mittempergher et al., 2021).
The fault strikes from the West a few kilometers North of the village of Edolo, where it probably merges with the Tonale line, to the East towards the Genova valley and the Giudicarie line. The GLFZ dips 40-50° to the south in the studied area (red box in Figure 3.1b).
The samples were collected form an outcrop located North of the Lobbia glacier (Lobbia outcrop; Figure3.1b). The exposed area was covered by the glacier until a few decades ago, so that the outcropping surface is perfectly polished and not weathered, granting an optimal exposure of most rock features. Here, the GLFZ cuts the Avio pluton, composed by medium-grained, biotite-bearing tonalites. The igneous rock is affected by five main late to post-magmatic deformation events, (Pennacchioni et al., 2006; Figure 3.2)

1. late-magmatic deformation: magmatic foliation is well developed at the boundary of the intrusions, in the Lobbia outcrop there are folded aplitic dykes and deformed mafic inclusions;

2. cooling joints: the whole outcrop is characterized by the presence of three regularly spaced sets of cooling joints, two steeply dipping, orthogonal sets oriented N-S and E-W and a low-angle set. Many of the joint surfaces are lineatied by biotite and hornblende grains, suggesting high temperature conditions during joint formation. Joints are segmented along strike (from less than a meter to tens of meters) and displacement on individual joints is negligible;

3. ductile shear zones: they reactivate cooling joints and cut the aplitic dykes. In some case there is a well-developed S-C foliation, though shear zones are usually few millimeters-thick. N-S striking mylonites have left-lateral sense of shear, while E-W ones are right-lateral;

4. cataclasite- and pseudotachylyte-bearing faults: these faults are widespread in the outcrop, and cut or reactivate aplitic dykes, cooling joints and ductile shear zones. These brittle faults dip circa 50° towards N195° on average, accommodate right-lateral shear and are clustered together to build a major fault zone (Gole Larghe fault zone). In the GLFZ, cataclasites are closely-spaced (less than 1 meter to 5 meters

apart) and are few millimeters to over a meter thick.

Cataclasites are often associated with pseudotachylytes, black to dark green/brown and occur as both fault- and injection- veins, as well as pseudotachylyte breccias and pull-apart related pools (Sibson, 1975);

5. zeolite-bearing veins and faults: the zeolite-bearing fault network is made by N-S and E-W striking major faults, which exploit cooling joints, ductile shear zones and cataclasite- and pseudotachylyte-bearing faults (Dempsey et al., 2014). The kinematic is quite complicated, and includes both strike-slip and reverse faults (Dempsey et al., 2014). Where there are multiple veins grouped to form small fault zones, they form an incision due to fast alteration and weathering of the zeolite veins sets. This is the last deformative event recorded in the rocks exposed in the Lobbia outcrop.

Ambient temperature during seismic faulting (i.e., during the formation of pseudotachylytes) can be inferred by the presence of incipient bulging recrystallization of quartz crystals in low-strain domains and epidote veins and greenschists facies propylitic alteration (Di Toro and Pennacchioni, 2005). These microstructural and mineralogical assemblages suggest a temperature of about 250°C during seismic faulting. The mineral assemblages in the contact aureole suggest a depth of 9-11 km at the time of seismic faulting (Riklin, 1983).

$^{40}Ar/^{39}Ar$ ages on pseudotachylytes are ca. 30 Ma (Pennacchioni et al., 2006). Since 30 My ago the Periadriatic lineament was active (Stipp et al., 2002; Stipp and Fügenschuh, 2004) and the GLFZ has right-lateral kinematic and branches from a compressional jog of the Tonale line (see Figure 3.1; Pennacchioni et al. (2006) for discussion) seismic faulting inside the Adamello pluton was probably induced by the transfer of strain from the Tonale segment of the Periadriatic line to the batholith, where inherited structures were reactivated (Di Toro et al. (2005a); Pennacchioni et al., 2006; Mittempergher et al., 2021). Di Toro et al. (2005a) and Di Toro et al. (2006) report evidence that some of the pseudotachylytes found in the Lobbia area were produced by seismic ruptures associated with ancient earthquakes of magnitude Mw 6.0 - 7.0 propagating from the Tonale Line towards the east into the Val D'Avio pluton.

Chapter 4

Results

Here I present the results of my thesis. My original study includes samples collected for previous studies (Castagna, 2012; Griffith et al., 2010) and new samples I collected specifically for the purposes of this thesis (sample list in Table 4.1). In particular, I describe:

1. the microstructures found in the pseudotachylytes, divided by structural domains (Figure 1.7)

   - injection veins;
   - extensional domains;
   - neutral domains;
   - compressional domains.

   The microstructural analysis has been carried out with a polarized-light optical transmission microscope. The main goal is to investigate the deformation processes that act during pseudotachylyte generation (mainly, earthquake rupture propagation and seismic slip) at the boundary between the pseudotachylyte and the wall rocks. When describing the microstructures, I refer to:

   - large crystals or grains: size$>$1 mm;
   - medium crystals or grains: 500 μm$<$size$<$1 mm;
   - small crystals or grains: size$<$500 μm.

2. the measurements of the main micro-roughness parameters (ω_0 and λ_{ave}, Figure 1.6)

Fault	Sample	Structural domain	Latitude	Longitude	Collected by
Fault 1-GPS	A1 A2	injection vein injection vein	N46 10' 19"	E10 34' 58"	A. Castagna (in Castagna, 2012)
Fault 2-GPS	A02-02 A02-04	neutral compressional	N46 10' 19"	E10 34' 53"	
Fault 3-GPS	A4	compressional	N46 10' 19"	E10 34' 52"	
Fault 4-GPS	A5 A7	extensional compressional	N46 10' 20"	E10 34' 53"	
L05	L05-02 L05-03 L05-04 L05-06 L05-07 L05-08	extensional neutral compressional compressional extensional neutral	N46 10' 21"	E10 34' 52"	W. A. Griffith (in Griffith et al., 2010)
L09	L09-01a L09-01b L09-02a L09-02b L09-03a L09-03b	extensional extensional compressional compressional neutral neutral	N46 10' 12"	E10 34' 26"	W. A. Griffith
W05	W05-S01 W05-S04	injection vein extensional	N46 10' 19'	E10 34' 58"	F. Lazari (this thesis)
W09	W09-S01	compressional	N46 10' 20"	E10 34' 59"	

Table 4.1: Samples analyzed in this thesis. All this dataset has been revised in the thesis.

3. the Fourier transform spectral analysis of the pseudotachylyte-host rock boundary.

4.1 Microstructural description of pseudotachylytes

4.1.1 Injection veins

A1 includes both an injection and the fault vein of fault1-GPS (Table 4.1). The injection vein includes flow structures, marked by brown and dark gray-colored bands. The dark gray areas appear to be rich in both small and large survivor clasts, while the brown bands have more glassy-like matrix and contain larger survivor clasts. The vein boundaries are coated with a gray band, while the brown bands are only found in the middle of the vein, though a higher resolution investigation (possibly with Field-Emission Scanning Electron Microscope) is required to precisely establish the matrix (or former melt) to clast ratio (Figure 4.1a).
On the eastern pseudotachylyte-host rock boundary there is a large left-lateral step, which is not related to any structure on the western side. Where the pseudotachylyte-host rock boundary is on biotite grains, the profile becomes rougher with both embayments and protrusions (Figures 4.1b and 4.1c). Note that, while embayments along the pseudotachylyte-host rock boundary are very common in the presence of biotite grains in fault veins (e.g., Figure 4.3d), protruding biotite crystals are almost exclusively found in injection veins.
The fault vein is bounded by cataclasite/ultracataclasite to the south, while to the north the rock is deformed but not altered (Figure 4.1d). The northern side has dragged biotite grains (with right-lateral shear sense) and pressure-solution seams. The northern boundary is quite straight, while the southern one has large steps and embayments not related to the presence of biotite grains.

A2 is a circa 6 mm-wide injection vein collected from the same fault of A1. The injection vein is composed of two en-echelon segments that nicely show the Mode I opening of the vein. In the quartz grains in the wall rocks there are well-developed fracture sets parallel and perpendicular to the injection vein, visible thank to fluid inclusion trails (Figure 4.2a). The features that characterize the micro-roughness of A2 are similar to A1, previously described.

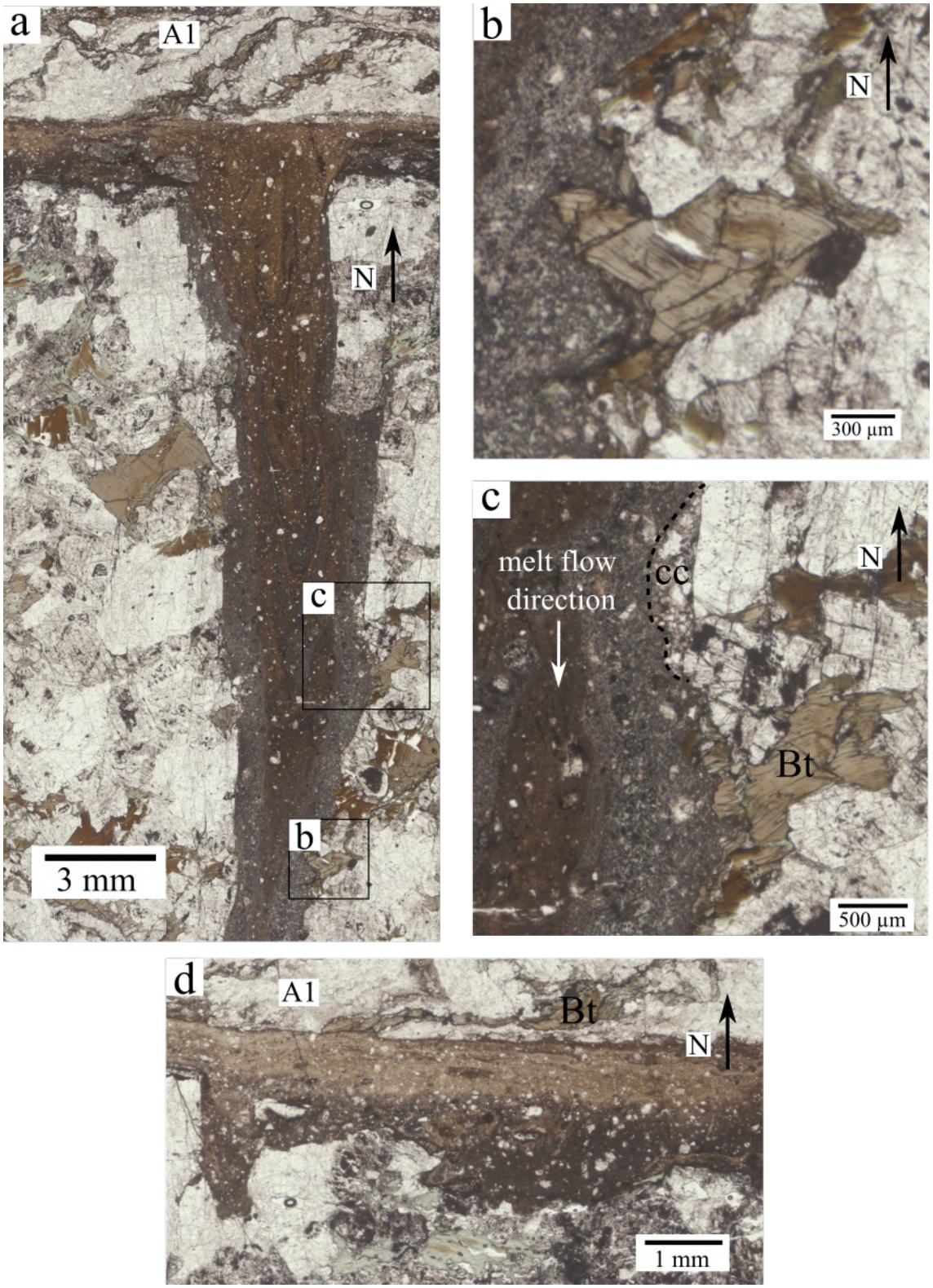

Figure 4.1: Plane-polarized light microphotograph of the Injection Vein A1. (a) injection vein in sample A1; (b) kinked biotite (Bt) with a protrusion and an embayment; (c) biotite (Bt) crystal with embayment, the dashed line defines a patch of white cataclasite (cc); (d) Fault vein boundaries of sample A1, the southern wall rock is altered and has a rough boundary, while the northern one is deformed and has a straight profile. Note the right-lateral drag of the biotite grain in the northern wall rock.

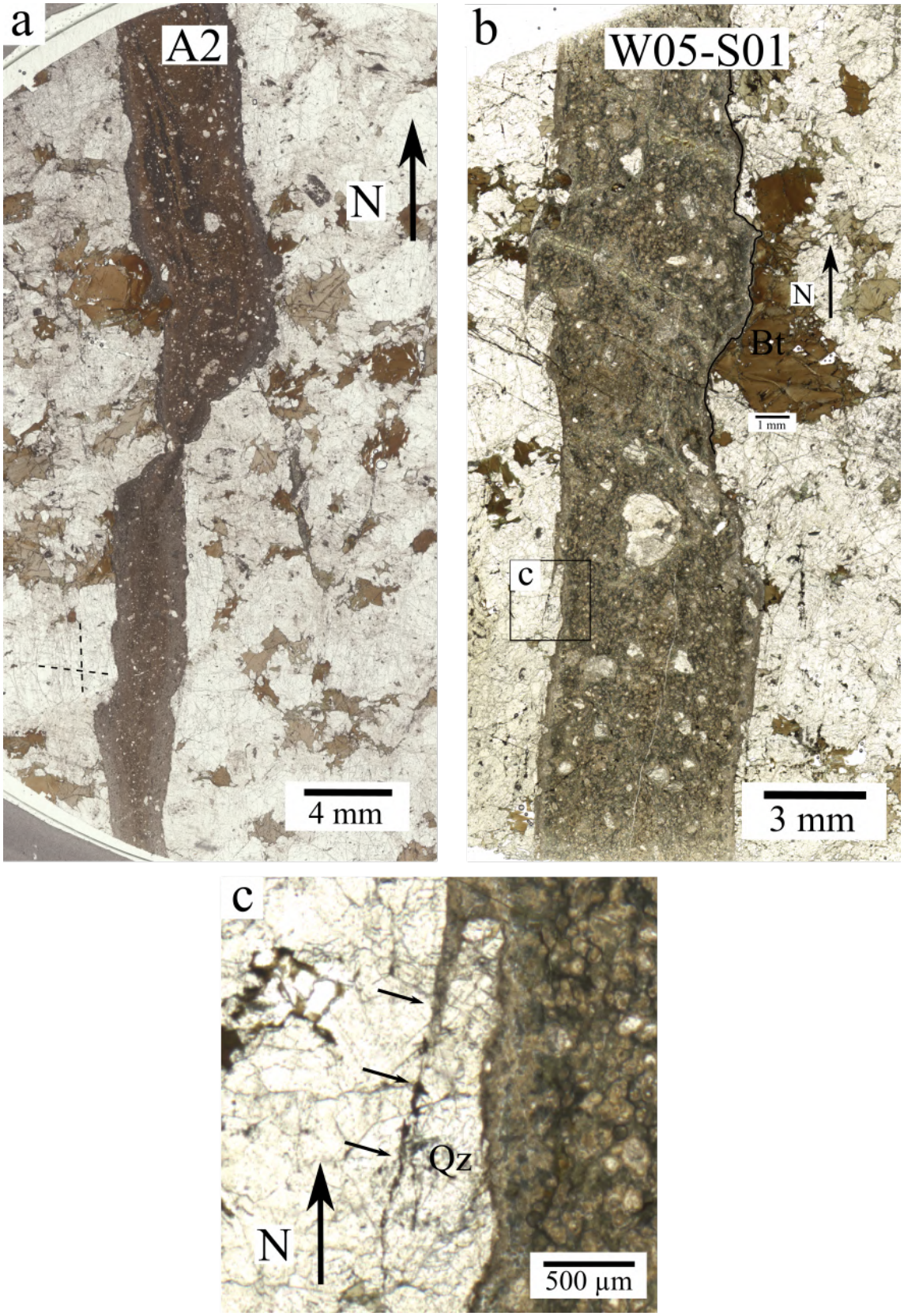

Figure 4.2: Features of injection veins A2 and W05-S01 (plane-polarized light microphotographs). (a) sample A2. In the middle of the vein there is a right-lateral stepover, the black dashed lines in the southwestern area highlight the two fracture sets; (b) sample W05-S01, note, on the eastern side, the large biotite grain (Bt) and the related embayment and the large survivor clasts (black circle); (c) detail on sample W05-S01, fragment of quartz (Qz) detaching from the wall rock because of former melt infiltration in a crack (marked with small black arrows).

W05-S01 shows similar features to samples A1 and A2 with biotite grains on the pseudotachylyte-host rock boundary that both protrude and create embayments (Figure 4.2b). On the western side of the vein there is a quartz promontory that during the injection of the melt was being detached from the wall rock (Figure 4.2c).
In the pseudotachylyte there are large spherulites (as those described in Di Toro and Pennacchioni, 2004; here up to 300 μm in diameter) and very large quartz and cataclasite clasts (up to more than 2 mm; Figures 4.2b and 4.2c).

4.1.2 Extensional domains

A5 in the northern wall rock has a network of pressure-solution seams and fractures/veins filled by ultra-fine, aphanitic, dark material (Figure 4.3a; probably an association of chlorite, epidote, titanite and iron-oxides, as described by Di Toro and Pennacchioni, 2005). One of these fractures/veins is connected to the pseudotachylyte (Figure 4.3b) and acts as a weakness surface, with the wall rock protruding into the pseudotachylyte matrix. Biotite grains always show well-defined embayments. There is a small injection vein on the southern pseudotachylyte-wall rock boundary (arrow in Figure 4.3a)

L05-02 was collected from a melt pool, it only contains the southern boundary of the fault. The pseudotachylyte-wall rock boundary presents multiple biotite-related embayments, two of which (Figure 4.3c) are filled with a-type cataclasite (see sample L09-01 for cataclasite classification).

L05-03 and L05-07 are similar, both present a smooth northern pseudotachylyte-host rock boundary and a cataclasite on the southern boundary (Figure 4.3d).

L09-01 a and L09-01b The pseudotachylyte-host rock boundary in these two samples is extremely rough due to the presence of cataclasites. In Figure 4.3e there is an example of the complex microstructures found in the two samples. The pseudotachylyte alternates with different types of cataclasites, that I classify as:

- a-type (cc-a) white, very fine-grained cataclasite. Similar to the one found in sample L05-02, I also refer to this cataclasite type as ”ultrafine cataclasite”;

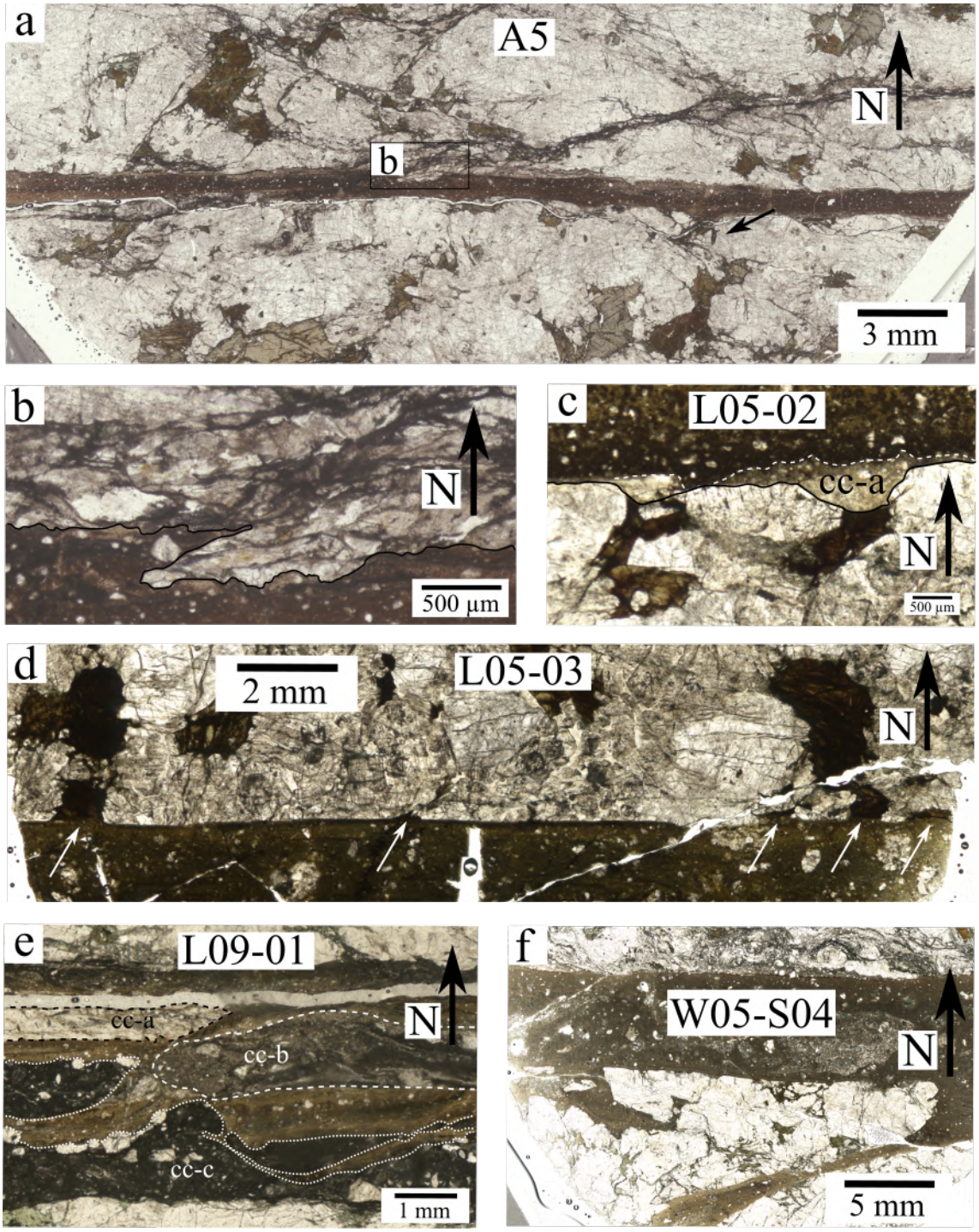

Figure 4.3: Features of extensional jogs (plane-polarized light microphotographs). (a) sample A5, on the northern wall there is a large pressure-solution seam (black vein), the black arrow points at a small injection vein in the southern wall rock; (b) detail of sample A5 on the embayment caused by the intersection between the pressure-solution seam and the pseudotachylyte; (c) a-type cataclasite-filled embayments on sample L05-02; (d) sample L05-03, white arrows mark biotite-related embayments; (e) different cataclasites in sample L09-01 (see text for description); (f) sample W05-S04 with the branching pseudotachylyte on the southern wall.

- b-type (cc-b) pale-brown, fine-to very fine-grained cataclasite, it always presents a graded boundary with the pseudotachylyte matrix, that might indicate a low melting temperature;
- c-type (cc-c) very fine dark green/black cataclasite containing quartz/plagioclase clasts.

W05-S04 the pseudotachylyte is branching on the southern side, isolating a rock portion that presents glassy matrix intruded up to 2 mm from the pseudotachylyte-host rock boundary (Figure 4.3f).

4.1.3 Neutral domains

A02-02 presents a thick fault vein (up to 5-6mm, Figure 4.4a), with a very large embayment on the southwestern side of the pseudotachylyte and a c-type cataclasite on the southeastern side. In the embayment there is a large clast preserving the contact between the cataclasite and the host rock (Figure 4.4b).
As for some of the extensional domains, the northern pseudotachylyte-wall rock boundary is smooth with some embayments, though here are caused by pressure-solution seams (marked by white arrows in Figure 4.4a) instead of biotite grains, as in the other samples.

A4 and L05-04 are similar, they both have thin (200-500 μm) fault veins and present a-type cataclasites patches in the melt (Figure 4.4c). Pseudotachylyte-host rock boundaries in both samples are rough due to pressure-solution seams or damaged rock portions.

L05-08 has smooth northern and southern pseudotachylyte-host rock boundaries, with 6 injection veins in the southern wall rock (white arrows in Figure 4.4d). On this sample were performed Field-Emission Scanning Electron Microscope cathodoluminescence and back-scattered electron investigations for the Bachelor thesis of Silvia Aldrighetti (2021).

L09-03 a and L09-03b were damaged during the sampling phase. The samples show complicated pseudotachylyte-cataclasite relationshipships, similar to that of sample L09-01, and two generations of pseudotachylytes, with the youngest (PST-2) cutting the older

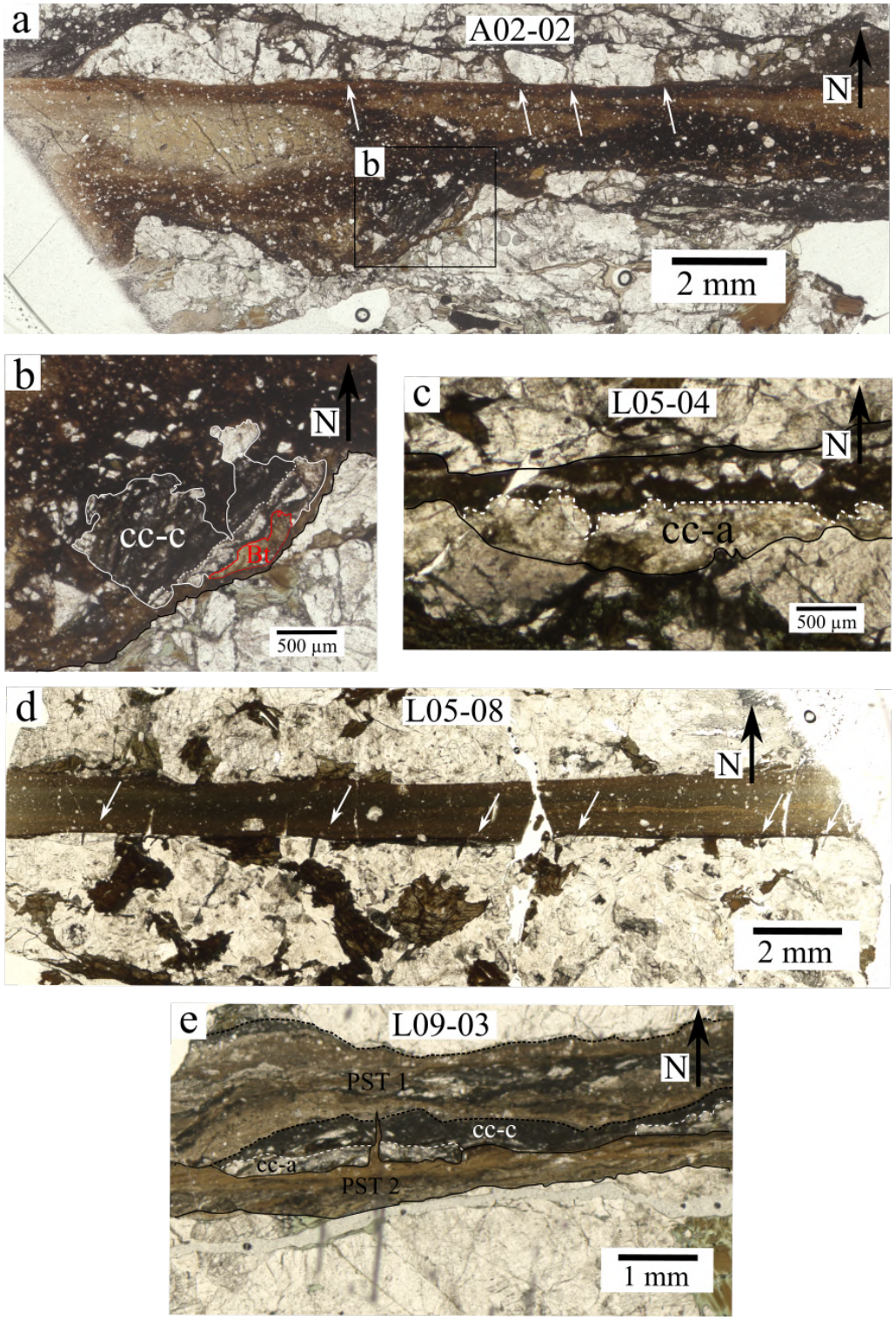

Figure 4.4: Features of neutral domains (plane-polarized light microphotographs). (a) sample A02-02, the southern boundary has a very large embayment, white arrows mark pressure-solution seams-related embayments; (b) clast in the embayment of sample A02-02 with preserved cataclasite-host rock contact, in red is outlined an extremely deformed and partially melted biotite grain in the clast; (c) biotite-related embayment filled with a-type cataclasite (cc-a) in sample L05-04; (d) sample L05-08, white arrows mark injection veins; (e) detail of sample L09-03, see text for description.

(PST-1) with an injection vein (Figure 4.4e). Note that on sample L09-01 there was no evidence for multiple pseudotachylytes.

4.1.4 Compressional domains

A02-04 and A7 both have previously deformed host rocks and are cut by pressure-solution seams. In both sections the southern pseudotachylyte-host rock boundary is dominated by the presence of cataclasites (c-type in A02-04 and a- and b-type in A7; Figure 4.5a). On biotite grains there are shallow embayments.

L05-06 has an extremely thin fault vein (Figure 4.5b) that contains a-type cataclasite patches. The northern pseudotachylyte-host rock boundary is exceptionally smooth, while on the southern boundary there are some shallow biotite-related embayments. In the middle of the section the two wall rocks are in contact with each other and the southern wall rock is extremely fractured (Figure 4.5c)

L09-02 a and L09-02b have a 2 mm-wide fault vein on the western side of the thin sections, while on the eastern side the fault vein is only 200 μm thick. In the middle the two wall rocks are in contact, as in sample L05-06. The northern pseudotachylyte-host rock boundary presents an embayment filled by b-type and a-type (Figure 4.5d).

W09-S01 fault vein's geometry is similar to sample L09-02, the sample presents important alteration in both the northern and southern wall rocks and pressure-solution seams in the northern wall rock, that generate deep embayments.

4.2 Pseudotachylyte-wall rock micro-roughness

4.2.1 ω_0, λ_{ave} and dissipated power.

After the qualitative analysis, I proceed to quantitatively describe the micro-roughness of the pseudotachylyte-host rock boundaries with the revised MATLAB®script presented in Section 2.2.2. Since the calculation method was changed and to avoid any bias caused by the profile drawing method, I retraced and recalculated the results from both natural

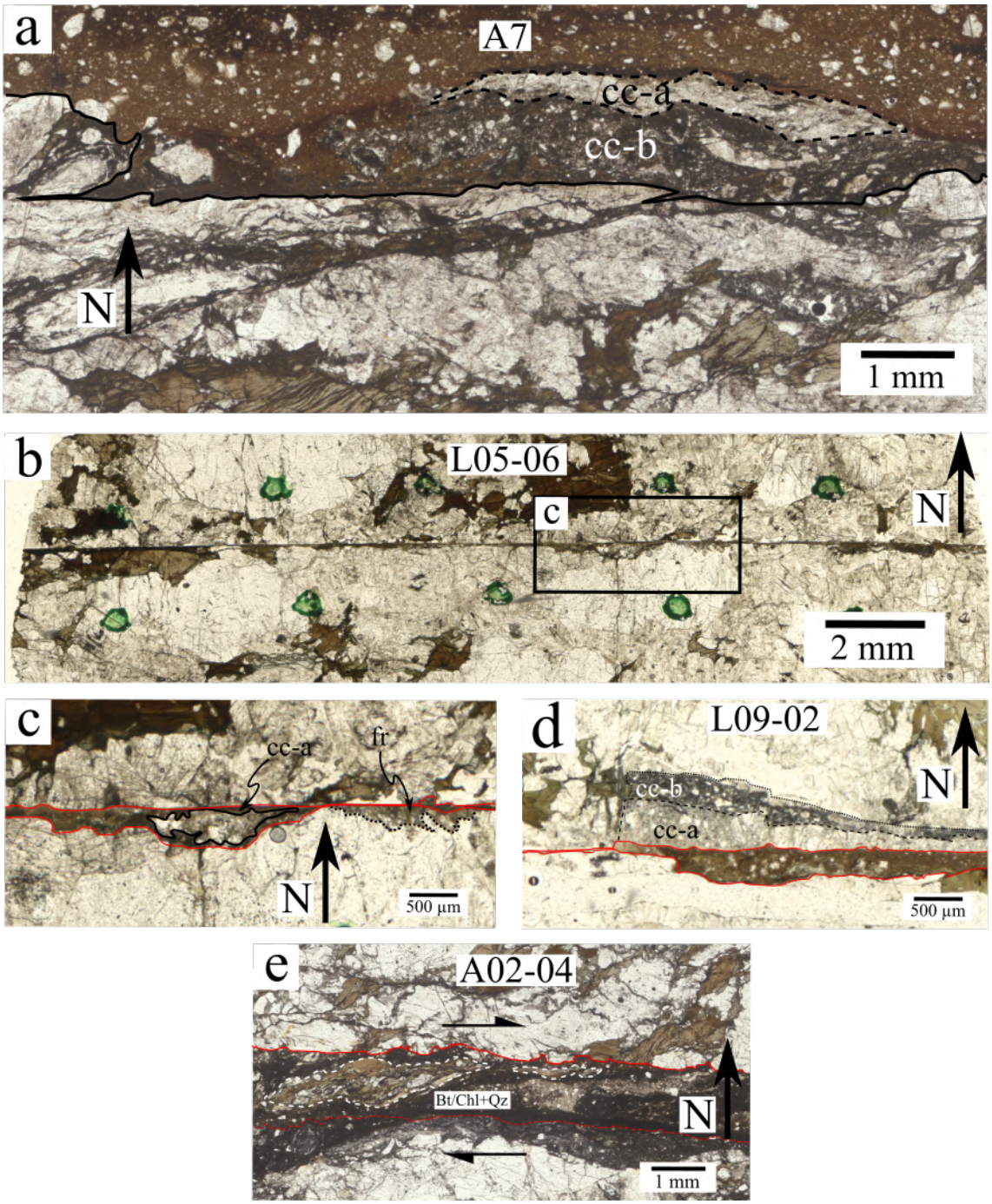

Figure 4.5: Features of compressional domains (plane-polarized light microphotographs). (a) detail from sample A7, a large embayment is set up where a b-type cataclasite was found, now cc-b is partially melted; (b) sample L05-06; (c) detail from sample L05-06, fr indicates the fractured rock at the contact between the two wall rocks; (d) detail from sample L09-02b showing the a- and b-type cataclasites that fill the embayment; (e) detail from sample A02-02, a wall rock clast made of biotite and quartz is being dragged in the pseudotachylyte with right-lateral shear. The southern pseudotachylyte-host rock boundary is dashed because the presence of a c-type cataclasite, the same color of the matrix, makes the boundary identification difficult.

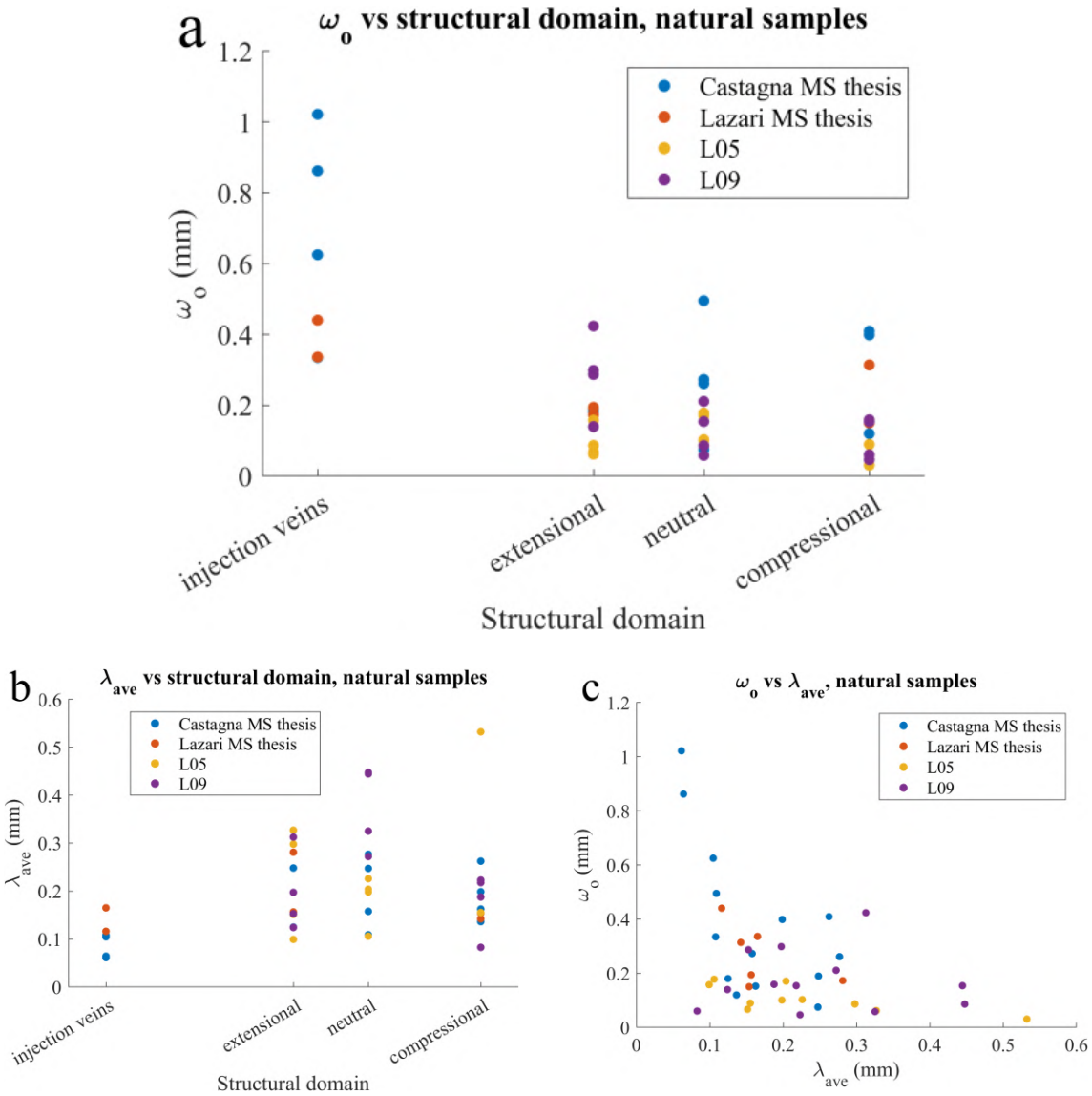

Figure 4.6: (a) ω_0 versus structural domain in all natural samples. Injection veins show a higher ω_0, while there are no relevant changes between the other structural domains; (b) λ_{ave} versus structural domain. There is no relationship in natural samples; (c) ω_0 versus λ_{ave} for natural samples, there is no relationship. An apparent inverse relationship can be seen at a first glance, but it is determined by some outliers and could only be caused by the high dispersion.

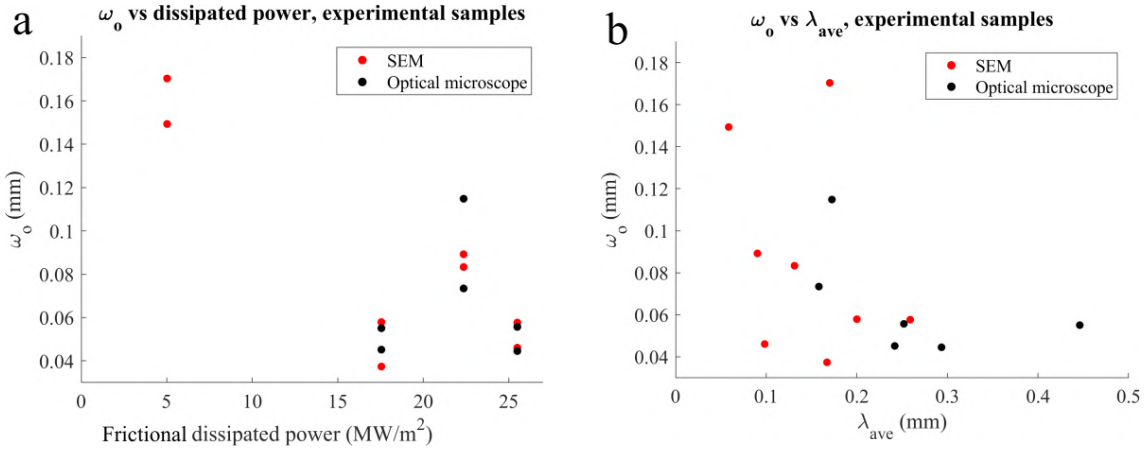

Figure 4.7: (a) ω_0 versus frictional dissipated power. There is an inverse relationship; (b) ω_0 versus λ_{ave}. There is a poor inverse relationship, data dispersion is extremely high.

and experimental samples calculated in previous study (Castagna, 2012), to obtain a coherent and solid dataset. All the thin sections digital scans, the host rock-pseudotachylyte boundaries, boundary height distributions, ω_0 values and the Fourier transform spectra are reported in Appendix B.

In Figures 4.6 are plotted the roughness parameters for all the natural samples with respect to the structural domain instead of the estimate of dissipated power, as it requires some strong assumptions (see Section 1.2.6). Theoretically, from injection veins to extensional, neutral and to compressional domains there is an increase in frictional dissipated power (Section 1.2.5).

λ_{ave} does not show any relationship with structural domain nor with ω_0, while there is an inverse relationship between ω_0 and structural domain. Note how with respect to Castagna's original data (Figure 1.9d) the newly calculated ω_0 values for Castagna's dataset are shifted inconsistently, though the overall trend is preserved. In all the plots there is a large dispersion, that is discussed and treated in section 5.2.

Experimental data (Figures 4.7a and 4.7b) varied with respect to the original ones in Figures 1.9a and 1.9b. In particular, ω_0 values for the sample with the lowest dissipated power doubled, for the other SEM-derived profile there is not an important variation, but the dispersion between top and bottom boundaries appears to be reduced. For OM-derived boundaries, instead, there is not an important variation between Castagna's data and the newly calculated ones.

The increase in ω_0 for the lowest-frictional dissipated power sample actually improved

significantly the trend between ω_0 and frictional dissipated power.

4.3 Fourier transform spectral analysis

Since there is no correlation between λ_{ave} and ω_0 or $\dot{Q}$, I decided to perform a Fourier transform spectral analysis on each pseudotachylyte-host rock boundary to better understand whether the wavelength of the boundary oscillations are related to the structural domains or not. The results are reported in Figure 4.8, subdivided by structural domain. Since the grouped spectra are difficult to read, I decided to plot the slope of the linear regression of each spectrum (in log-log space) against frictional dissipated power or structural domains (see Figure 4.8e for the slope determination).

In Figure 4.9a are plotted the slopes of the Fourier spectra of experimental samples versus frictional dissipated power. In optical microscope-derived slopes there is an increase in slope with increasing dissipated power, as in SEM-derived profiles, though the sample with frictional dissipated power equal to 5 $\frac{MW}{m^2}$ has a very high dispersion that causes the difference in slope variation between OM and SEM derived-spectra (0.019 MW^{-1} for OM-derived pseudotachylyte-host rock boundaries versus 0.0060 MW^{-1} for SEM-derived boundaries, Figure 4.8a).

In Figure 4.8b, instead, there are the slopes of natural samples spectra. Both in the whole dataset and in single faults there is not a trend in slope variation with different structural domains.

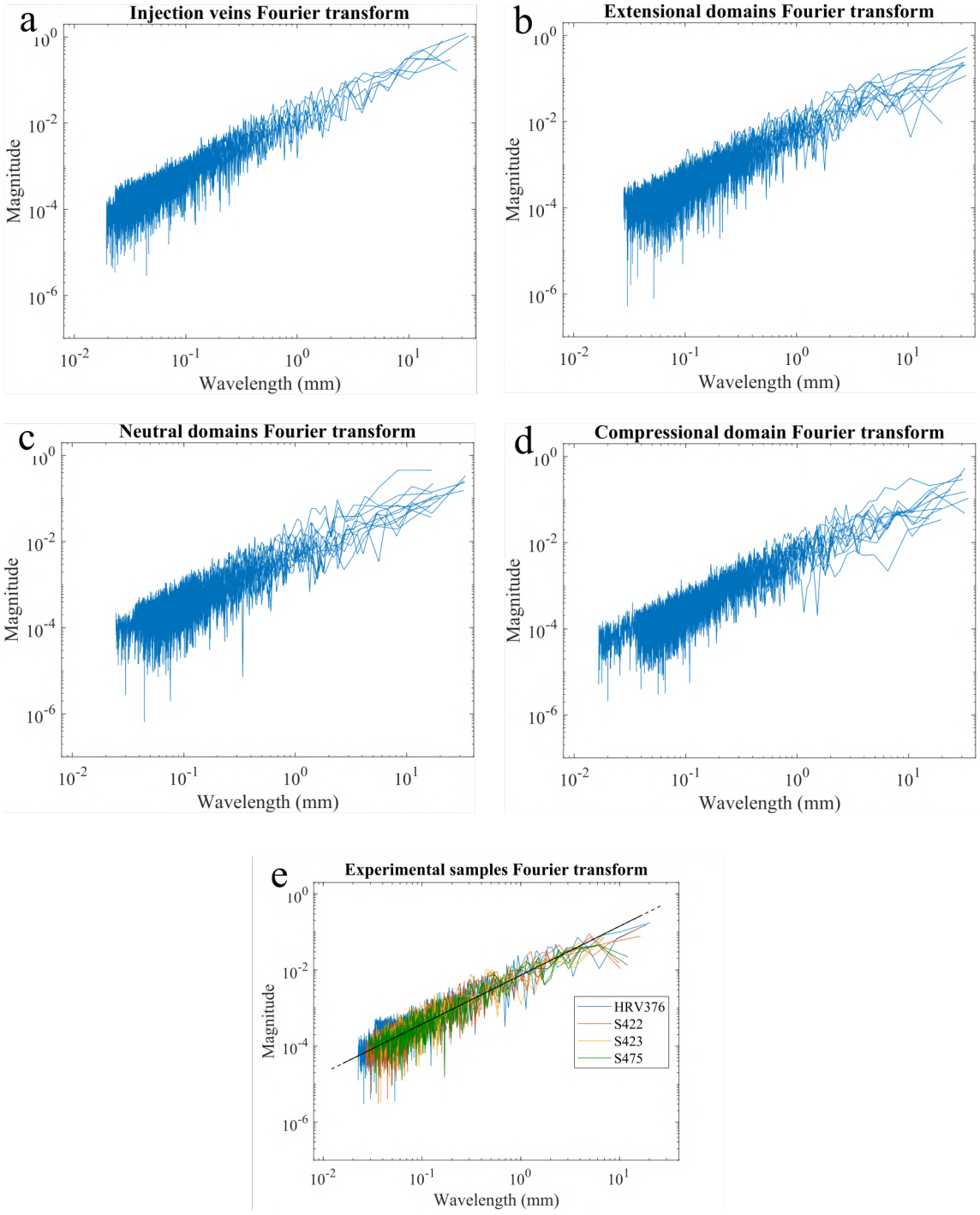

Figure 4.8: Fourier transform spectral analysis for:(a), injection veins; (b) extensional domains; (c) neutral domains; (d) compressional domains; (e) experimental samples, here the black line is the log-log linear regression fit.

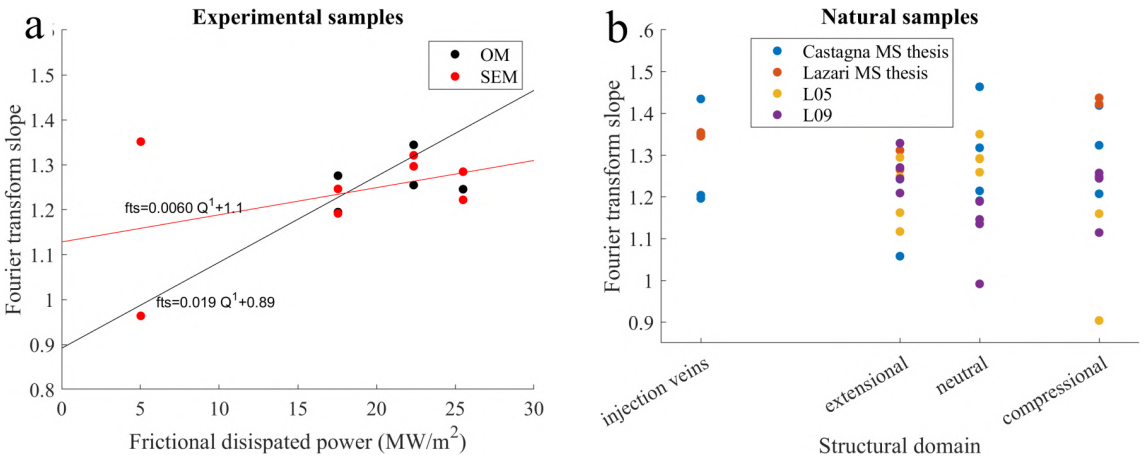

Figure 4.9: Slope of the Fourier transform versus frictional dissipated power for experimental samples (a) and versus structural domain in natural samples (b). In Figure (a) are also plotted the slope variation regression lines for both SEM and OM-derived profiles.

Chapter 5

Discussion

Based on the microstructural data presented in Chapter 4, some general considerations and interpretations of the microstructures as well as a selection of the micro-roughness data can be done. This analysis and selection is crucial to test whether the relationship between frictional dissipated power and micro-roughness of the pseudotachylyte-host rock boundary presented in Section 1.2.3, which is supported by both theoretical and experimental evidence (Nielsen et al., 2010; Castagna, 2012), is applicable also to natural pseudotachylytes. In fact, theoretical studies (which consider the micro-roughness evolution during seismic slip by friction melt–wall rock interaction) and experimental studies (which simulate seismic slip in the laboratory but not the stress perturbation which induces intense fracturing at the rupture tip; e.g., Swanson, 1991; Bestmann et al., 2016) neglect the fact that pseudotachylytes are fault zone rocks produced by both seismic rupture propagation and seismic slip.

5.1 Interpretation of pseudotachylyte-wall rock microstructures

Based on the microstructures found in fault and injection veins (section 4.1), I attempt at distinguishing the microstructures mainly associated with rupture propagation or with seismic slip. This interpretation should allow me to select the micro-roughness data to be used to estimate the frictional dissipated power in natural faults during earthquakes.

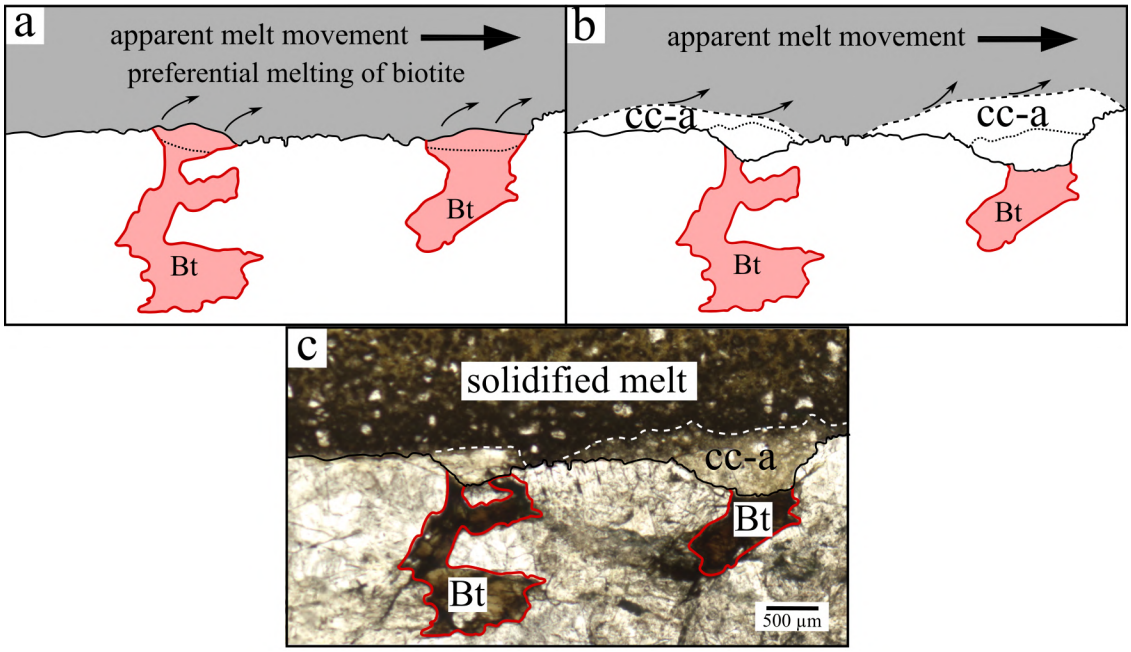

Figure 5.1: Interpretation of the formation of the cataclasite-filled embayments found in sample L05-02 (Figure 4.3c). Black arrows in subfigure (a) represent biotite (Bt) melting, while in subfigure (b) represent the possible loss of material from the cataclasite (cc-a) to the melt, that could happen at the cc-melt boundary.

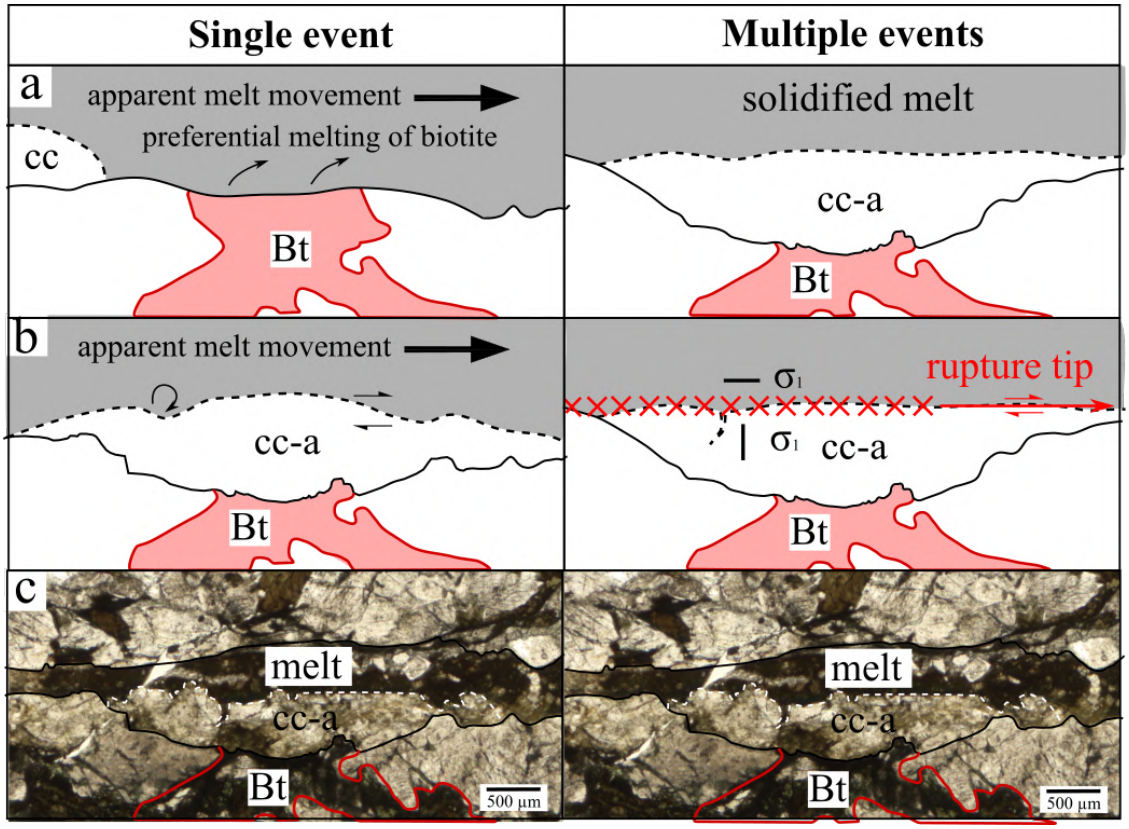

Figure 5.2: Two possible mechanisms for the formation of the cataclasite (cc) patch found in sample L05-04 (Figure 4.4c)

5.1.1 White cataclasites

Ultrafine a-type cataclasites (white in color under the optical microscope with plane polarized light) are found as clusters or patches dispersed in the pseudotachylyte matrix or sealing the pseudotachylyte-host rock boundary, often as a filling of the embayments (Figures 4.1c, 4.3c and e, 4.4c, 4.5a, c and d). These clusters of ultrafine cataclasites are never found away from the pseudotachylyte matrix and, as a consequence, they must be associated to seismic processes.

During seismic rupture propagation, the large stress perturbation at the rupture tip propagating at kilometers per second along the fault induces intense fracturing in the wall rocks (Swanson, 1991; Di Toro et al., 2005a; Bestmann et al., 2016). This is instantaneously followed by fault slip, probably occurring at rates of 10-100 m/s in the first milliseconds; such large slip rates decay to few meters and cm/s with progressive slip (yielding an average coseismic slip rate of 1 m/s). Coseismic rupturing and slip are associated to on-fault frictional sliding and, because of frictional heat dissipation, to an abrupt temperature increase in the slipping zone and eventually melting of the fragmented rocks. The intense coseismic fracturing, which might be more intense in contractional domains, produces a dense nano- to meso-scale fracture network (see Figs. 4.1a and 5.3) including sidewall ripeouts (that produce clasts like the one found in Figure 4.4b) or these ultrafine cataclasites that can be dragged by the melt.

Because of their low individual melting point (ca. 700°C, Spray, 2010) fragments of biotite dispersed in the slipping zone are easily melted, while quartz and plagioclase, given their higher individual melting point (ca. 1700 °C and 1100°C, respectively, Spray, 2010), are more refractory and may (1) be partly assimilated by the friction melt, (2) survive, forming these ultracataclasite-like clusters or (3) survive as single or polymineralic clasts.

This fragmentation process mainly associated to intense mechanical perturbation and frictional sliding (abrasive wear, adhesive wear, etc.) on geometrically heterogeneous slipping zones and surfaces (i.e., presence of contractional and extensional domains, Figure 1.7), can be further aided by mineral thermal cracking or fluid inclusion expansion and decrepitation due to the very fast temperature increase induced by rapid shear heating (Sibson, 1975; Pittarello et al., 2008).

If the fragmented material, be it produced by the rupture propagation, by abrasive/adhesive

wear or by thermal cracking, is dragged along the friction melt-host rock boundaries during sliding and not dispersed in the melt it can end up filling the embayments that formed due to selective melting of biotite.

In Figure 5.1 I interpret this sequence of fracturing, melting and ultrafine material dragging by the friction melt, associated to seismic rupture propagation and slip which lead to the formation of a ultra-smooth pseudotachylyte-wall rock boundary, independently of the frictional dissipated power associated to seismic slip. In Fig. 5.1, the point of view is fixed to the wall rock, so that there is a relative motion of the melt in the direction of the shear sense (right-lateral). In Figure 5.1a, seismic rupture propagation and frictional sliding (that preferentially fracture the biotite grains also because of their low strength; Spray, 2010) plus selective melting consume preferentially the biotite grains forming an embayment. In Figure 5.1b an ultrafine cataclasite cluster, formed by fragmentation of quartz and/or plagioclase elsewhere along the fault, is dragged by the melt on the host rock-pseudotachylyte boundary and fills the embayment, forming a smooth melt boundary in Figure 5.1c.

A more complex structure is present in sample L05-04 (Figure 4.4c) and can be explained at least in two ways (Figure 5.2). The first interpretation is similar to the one in Figure 5.1 but the ultrafine cataclasite cluster (made of quartz and plagioclase) is further shaped by the melt into its final arrangement, with the formation of a straight surface on the eastern side of the patch and a sharp embayment on the western side (Fig. 5.2a, b and c, left side). However, further considerations on melt and granular aggregates fluid dynamics are required to establish whether this explanation is realistic or not.

The second interpretation considers the occurrence of multiple seismic events: first, the ultrafine a-type cataclasite patch is emplaced and spread on the embayment with the same mechanisms as in Figure 5.1, then a seismic rupture associated to another earthquake (or a second rupture pulse during the same earthquake) fractures the rock, forming an injection vein in the cataclasite body (Figure 5.2b, right side). Then, friction sliding and melting shape the ultrafine cataclasite into the one found in the sample (Figure 5.2c). The problem with this second interpretation is that there is no evidence for multiple events on the fault L05 on the outcrop nor in the thin sections.

If such ultrafine cataclasite clusters formed during the rupture propagation, they witness a

deformation stage related to the propagation of the rupture tip that are not reproducible in rotary shear experiments. As a matter of fact, such ultrafine clusters have never been described in experimentally produced pseudotachylytes (Di Toro, personal communication).

5.1.2 Effects of rupture propagation on the host rock at the microscale

As presented in Section 1.2.2 and in Figure 1.3, numerical simulations and field evidences show that the rupture propagation induces an intense stress perturbation at the rupture tip (Kame et al., 2003; Poliakov et al., 2002; Di Toro et al., 2005a). If the rupture propagates from the west towards the east, (as was probably the case for most of the seismic ruptures propagating along the Gole Larghe Fault; Di Toro et al., 2005a) and the sense of shear is dextral, the maximum principal stress at the rupture tip rotates perpendicular to the fault surface on the southern block and parallel to the fault surface on the northern block. This causes the production of most injection veins on the southern block (since rocks are weaker in extension than in compression, Di Toro et al., 2005a).

On the sample L05-08 (Figure 4.4d) were performed Scanning Electron Microscope Back Scatter Electron (SEM-BSE) and cathodoluminescence (SEM-CL) investigations. In the SEM-BSE image the wall rock appears to be intact and cut by the injection vein (Figure 5.3c). However, in the SEM-CL image, the wall rock grains are intensely "in-situ" fractured. At the tip of the injection vein the fracturing is so intense that the rock is almost pulverized.

The injection vein sharply cuts the fractured rock, suggesting that (1) vein filling occurred when the grain fragments were sealed or (2) the melt was too viscous to intrude such thin fractures. Case (1) implies that coseismic fracturing at the rupture tip was immediately followed by a sintering, sealing or welding stage, otherwise melt injection would have impregnated the microfracture network. In any case, these densely fractured rock volumes bordering the slipping zone could be at the source of the ultrafine cataclasite patches previously discussed (see Figures 5.1 and 5.2).

Instead, in the northern wall rock of sample L05-08 fracturing is considerably less intense than in the southern wall, and the few fractures are oriented parallel to the fault (SEM-BSE and SEM-CL images in Figures 5.3a and 5.3b). This fracture distribution and orientation would be consistent with the propagation of seismic ruptures from the West towards the

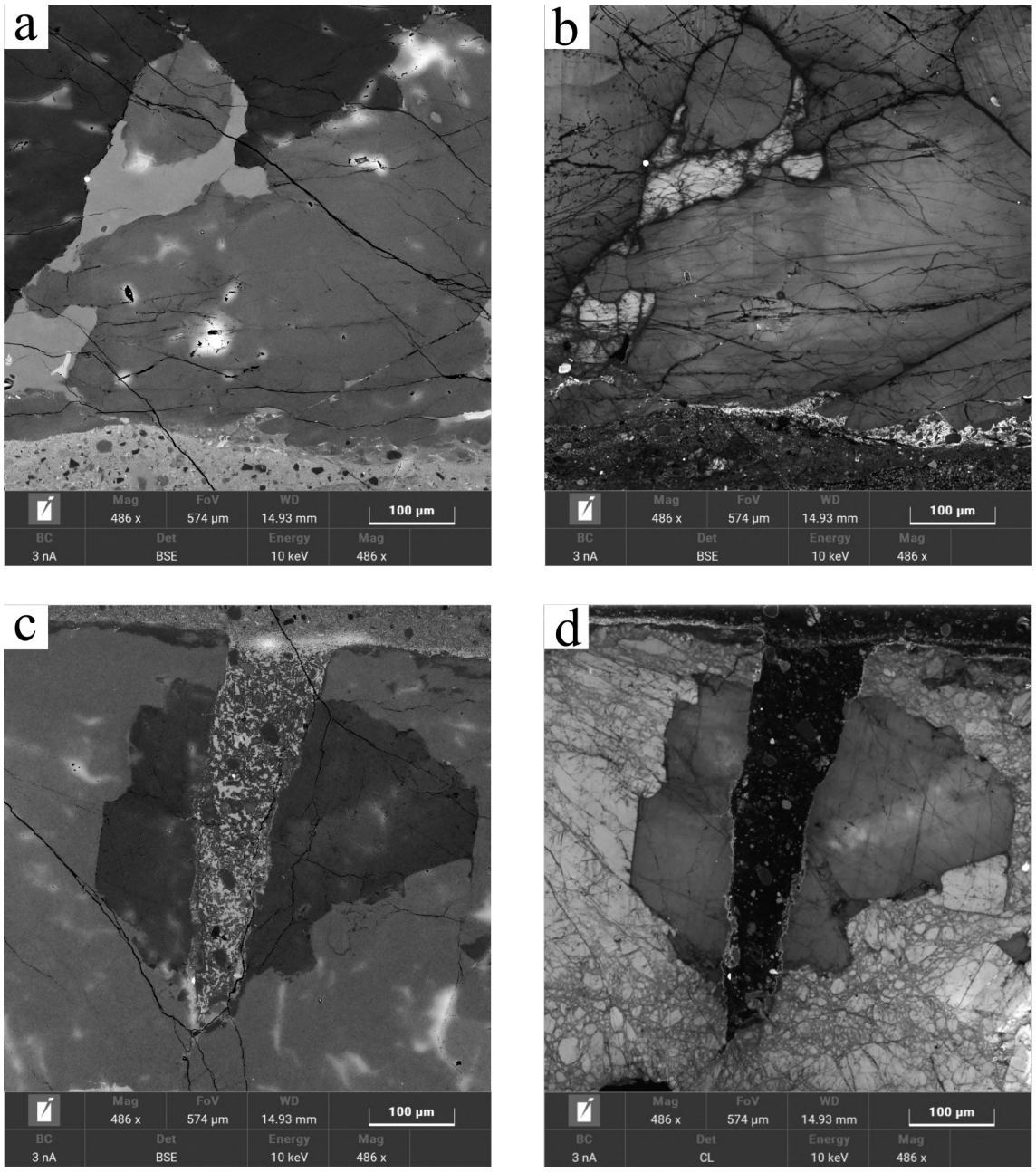

Figure 5.3: SEM images of sample L05-98 (a) back-scattered electrons image of the northern pseudotachylyte-host rock boundary. From the darkest to lightest mineral: quartz, plagioclase and K-feldspar, white patches are due to a poor graphite coating of the section. (b) cathodoluminescence panchromatic image of the northern boundary. Note the relative integrity of the minerals with respect to subfigure (d) and the presence of a fault-parallel fracture set. (c) SEM-BSE image of the second injection vein from the West. The darker mineral is quartz, while the lighter one is plagioclase. (d) SEM-CL panchromatic image of the injection vein. Note the extreme in-situ fragmentation of plagioclase and the relative integrity of quartz, where the few fractures formed at a high angle to the fault and parallel to the injection vein.

East along this particular right-lateral strike slip fault of the Gole Larghe Fault Zone (Di Toro et al., 2005a).

5.1.3 Effects of frictional sliding and preexisting cracks on the micro-roughness

When looking at the pseudotachylyte-wall rock boundary micro-roughness there are no particular features typical of only one structural domain.
For instance, the presence of a biotite grain in the wall rock should form an embayment (Spray, 2010). However, the evidence is that in the case of injection veins (samples A1, A2 and W05-S01) and in one case of a compressional domain (sample A4), biotite grains are associated to embayments but also protrusions or "promontories".
This means that, though preferential fracturing and melting act on the wall-rocks where biotite grains are exposed, as witnessed by the numerous associated embayments, Mode I fracturing and abrasive/adhesive wear can generate biotite-made protrusions. Moreover, ripping of quartz and plagioclase fragments from the wall rock and abrasive wear can in some cases result in the formation of embayments. The presence of embayments associated to quartz grains in the wall rock is clearly in contrast with theoretical expectations for frictional melting, but should not be surprising if we consider the role of fracturing associated to the propagation of seismic ruptures.
However, in general, in the studied pseudotachylyte-host rock boundaries fault veins from contractional domains are smoother than those from extensional domains (Figures 4.3 and 4.5). Instead, injection veins (or melt-filled cracks) have the more rough boundaries with respect to the other domains mainly due to their formation mechanism under pure tension (Mode I cracks). Mode I crack propagation results in the formation of rough surfaces which are not refined by later shearing and smoothing in the presence of solid rock, melt or a combination of the two in the slipping zone: shearing and frictional power dissipation clearly results in boundary smoothing. For this reason, injection veins are here considered as a reference roughness generated with $\dot{Q}$=0 $\frac{MW}{m^2}$.
Other features that affect the micro-roughness are the presence of preexisting (1) cataclasites and (2) microfractures and pressure-solution seams in the fault walls. Preexisting

cataclasites often make the pseudotachylyte-wall rock boundary rougher, since there are at least two kinds of preexisting cataclasites, b- and c-type, which seem to have different toughness and/or melting points (Figures 4.3e, 4.5a; note that the cc-a, also called here ultrafine cataclasite, is probably coeval to the formation of the pseudotachylyte as previously discussed; Figures 5.1 and 5.2). Instead, if the wall rock is made by the same kind of cataclasite, the boundary with the pseudotachylyte is quite smooth. Given the further complexity that the presence of different preexisting cataclasites brings to the micro-roughness, pseudotachylyte-wall rock boundaries that include different preexisting cataclasites will be discarded from the selected "frictional dissipated power versus micro-roughness" plots, discussed in section 5.2 (Figure 5.4).

Pressure-solution seams perhaps have a simpler effect on micro-roughness, at least compared to the presence of preexisting cataclasites in the wall rocks, due to the lower melting temperature of the minerals of these seams (mostly chlorite, melting at ca. 700°C; Spray, 2010) with respect to the rock forming minerals. For instance, pressure-solution seams form deep embayments along the boundaries, without any evidence for fracturing or other mechanical process: the presence of these embayments is probably related to selective non-equilibrium melting (Figure 4.4a). A second feature of these pressure-solution seams is that they act as weakness surfaces inside the wall rocks, so that rock portions delimited by these seams can detach from the wall rock and be carried in the melt, leaving in the wall rock a large embayment (Figures 4.3a and 4.3b). The thermal-related effect of these seams on the micro-roughness is compatible with the theoretical model discussed in section 1.2.3, while the detachment of small fragments along the pressure-solution seams next to the slipping zone results in an additional micro-roughness not related to thermal processes and melt interaction with the wall rock.

For this reason, I excluded from the selected "frictional dissipated power vs. micro-roughness" plots samples that showed a micro-roughness influenced by the detachment of wall rock fragments (section 5.2).

5.2 Estimate of frictional dissipated power during earthquakes

5.2.1 Selection of the profiles from the dataset

The relationship between ω_0 and frictional dissipated power has a large scatter (Figure 4.6a). Based on microstructural evidences I interpret this scatter as due to the several processes (seismic rupture propagation, frictional sliding, wear, frictional melting, etc., see section 5.1) that affect the formation and evolution of the micro-roughness of the pseudotachylyte-wall rock boundary. In fact, with the exception of the frictional melt-wall rock interaction, none of these mechanical processes were considered in the theoretical model or discussed in the previous works (Nielsen et al., 2010; Castagna, 2012). For this reason, I selected from the dataset the boundaries that better satisfy the assumptions of the theoretical model as follows:

1. pseudotachylyte must not be altered;

2. since the thermal model does not include the effects of rupture propagation, I discarded micro-roughness boundaries of fault veins that are clearly influenced by mechanical processes (e.g. presence of sidewall ripeouts).

The boundaries discarded from the dataset are:

- A02-04, southern profile (Figure 4.5e) was excluded because the pseudotachylyte and the cataclasite in the southern wall have almost the same color, making the accurate identification of the pseudotachylyte-wall rock boundary difficult, if not impossible, at the optical microscope.

- Sample L09-01b has a complex microstructure (Figure 4.3e), with the pseudotachylyte pinching out in the host rock and with several cataclasite bands. I could not draw a continuous line on the northern nor on the southern boundary.

Instead, for the following samples I considered a limited part of the entire boundary:

- Sample A02-02 (Figure 4.4a) has a large embayment on the southern wall, clearly not related to a thermal process but rather caused by a mechanical one. Therefore, I discarded the western portion of the profile and only kept the eastern part, not influenced by the ripping of the sidewall.

- The northern side of sample A5 contained a sharp embayment (Figure 4.3b) that had to be cut with a step on the drew boundary, since the script cannot evaluate profiles with multiple points with the same x-coordinate values (Section 2.2.2). Therefore, I cut the promontory from the drew boundary with a straight line (that does not influence roughness parameters) to avoid the creation of an artificial step.

- On the southern side of sample A5 there is basically the same feature described for the northern side of sample A5. However, here was not possible to cut the step without creating any artificial roughness, so I excluded the small portion of the profile west of the step.

- The southern profile of sample A7 contains a very large step in the middle of the section, caused by the sudden opening, from the West to the East, of a cataclasite layer (Figure 4.5a). Here, I removed the step by joining the two segments of the profile, east and west of the step.

- The western side of sample W05-S01 presents a needle-like embayment because of the detachment of a ”promontory” of quartz (Figure 4.2c), that creates a step. As for profile A5 N, I cut the promontory with a straight line.

- The northern side of sample W09-S01 is partly altered. In the easternmost portion of the sample, indeed, the rock is so altered that it is not straightforward to identify the host rock-pseudotachylyte boundary. For this reason, I decided to only keep the central and western portions of the boundary.

The revised dataset of the micro-roughness parameters for the natural pseudotachylytes is plotted in Figures 5.4a, b and c. Between ω_0 and λ_{ave} and between λ_{ave} and frictional dissipated power there is no relationship. Instead, the inverse relationship between ω_0 and frictional dissipated power, with the largest micro-roughness amplitudes for the injection

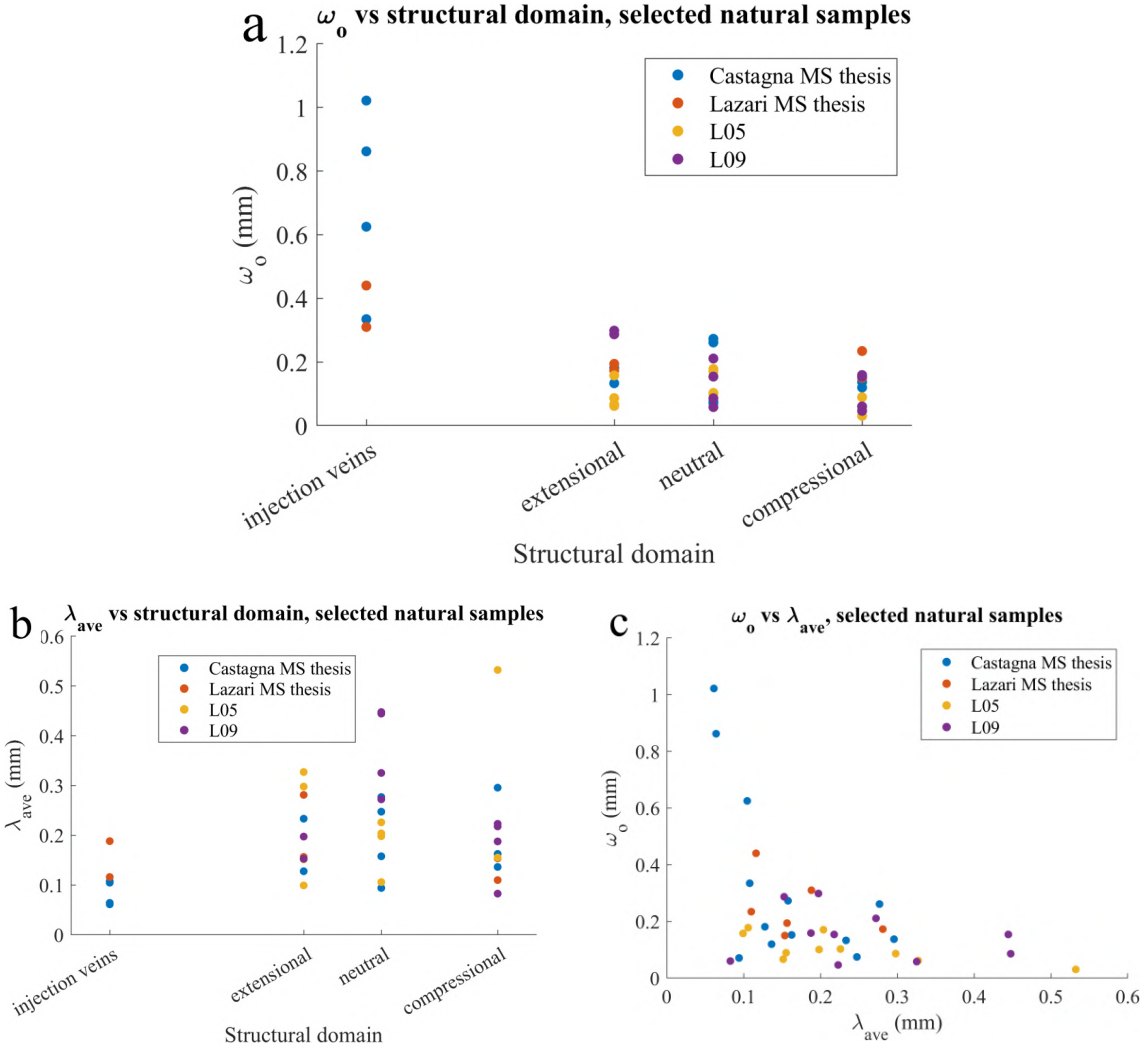

Figure 5.4: Micro-roughness parameters plots of the revised dataset. (a) plot between ω_0 and structural domain. The boundaries selections and elaboration improved the trend in fault veins; (b) λ_{ave} versus structural domain. The dataset is still extremely dispersed and does not show a trend; (c) ω_0 versus λ_{ave}, a relationship is still absent.

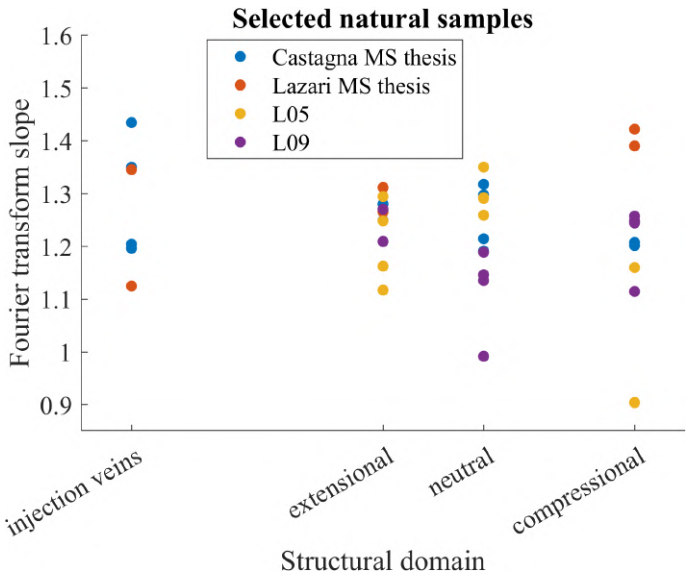

Figure 5.5: Slope of the Fourier transform versus frictional dissipated power for selected natural profiles.

veins (i.e., where the frictional dissipated power should be negligible) and the smallest for the compressional domains (i.e., where the frictional power dissipation should be the largest), is more robust due to the removal of the rupture-dominated micro-roughness areas (Figure 5.4a).

In Figure 5.5 is reported the slope of the Fourier transform spectrum of the micro-roughness versus the frictional dissipated power, calculated for the selected boundaries. Consistently with the diagram which reported the full dataset in Figure 4.9b, the removal of these selected micro-roughness data confirms the lack of clear dependence of the slope of the spectrum of the micro-roughness with increasing frictional dissipated power.

For experimental samples, instead, the slope of the spectrum increases with increasing dissipated power both in SEM and OM-derived profiles (Figure 4.9a), though on the sample with $\dot{Q} = 25 \frac{MW}{m^2}$ there is a discrepancy between OM and SEM-derived profiles. The increase of the slope means that with increasing frictional dissipated power large wavelengths become more common than small ones. The SEM-derived boundaries show a change in slope of 0.006 MW^{-1}, while OM-derived profiles show a slope variation of 0.019 MW^{-1}, meaning that on average for SEM-derived samples the Fourier spectra slope goes from 1.15 at 5 $\frac{MW}{m^2}$ to 1.3 at 25 $\frac{MW}{m^2}$ and from 1 to 1.4 for OM-derived profiles for the same frictional dissipated power range. Note that this variation is within the dispersion of natural samples slope (Figure 5.5).

5.2.2 Estimate of frictional dissipated power in natural faults

Following the discussion in previous works presented in Section 1.2.6 (Griffith et al., 2010; Castagna, 2012), we can relate experimental and natural data of the micro-roughness parameters describing the pseudotachylyte-host rock boundary, even though natural samples will carry a large error of $\pm 30 \frac{MW}{m^2}$ due to the uncertainties in the estimates of $\dot{u}$ and τ_{ss}.
In Figure 5.6 is plotted ω_0 versus frictional dissipated power for both experimental and natural samples, with the error for the latter. The ω_0 values of natural samples are higher than those of the experimental samples for a given estimated frictional dissipated power and there are two trends: one for natural samples, with a higher ω_0, and a second one for experimental samples with lower ω_0 values.
Starting from Equation 1.9 we can calculate the thermal boundary using the host rock thermal parameters:

$$z_b = \frac{A}{\tau \dot{u}} \tag{5.1}$$

with A being a scaling parameter dependent on the rock thermal properties:

$$A = \kappa \rho (L + c(T_m - T_i)) \, [\frac{kg\ m}{s^3}] \tag{5.2}$$

with, for tonalites, $\kappa = 4.97 \times 10^{-6} \frac{m^2}{s}$, $\rho = 2600 \frac{kg}{m^3}$, $L = 332 \frac{kJ}{kg}$, $c = 1.153 \frac{kJ}{kg\ K}$, $T_m = 1450°C$ and $T_i = 250°C$ (from Di Toro and Pennacchioni, 2004), so that $A = 2.2169 \times 10^4 \frac{kg\ m}{s^3}$.
With the parameter "A" for tonalite, I can plot Equation 5.1 on the ω_0 vs. frictional dissipated power plot (Figure 5.6).
According to Figure 5.6, z_b is larger than ω_0 except for the northern profile of sample W09-S01 that lays almost on the curve for A=22169.
This is consistent with the observation that melting should occur closer to the slipping zone with respect to the thermal boundary z_b: hence ω_0 should be always lower than z_b (Figure 5.7).
As previously discussed, experimental data have lower ω_0 values than natural ones for a given (estimated) frictional dissipated power, so that the tonalite-calibrated thermal bound-

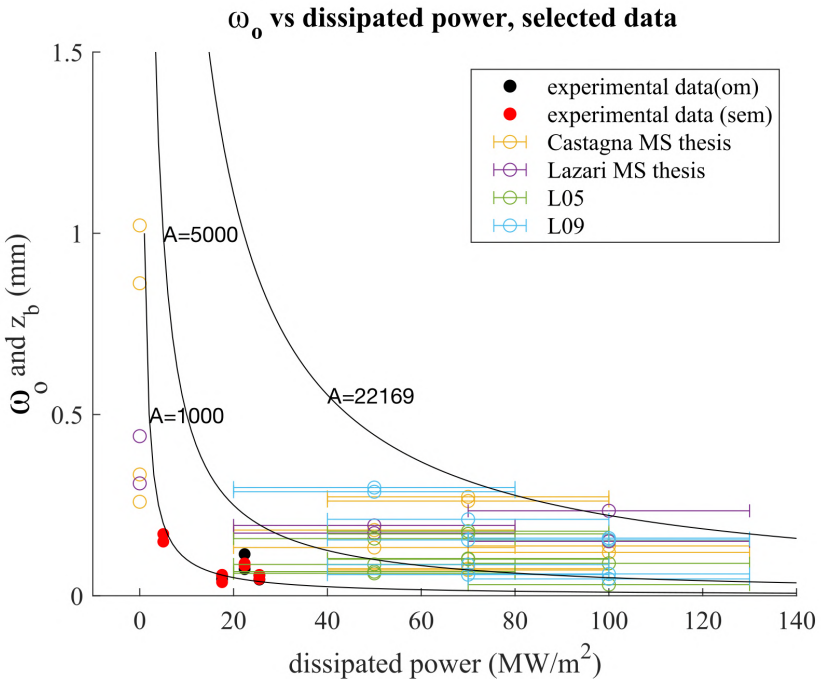

Figure 5.6: ω_0 versus frictional dissipated power in both natural and experimental samples. Black lines are the thermal boundaries calculated with Equation 5.1 for different A values. The highest A value is the scale factor derived from tonalite's thermal parameters.

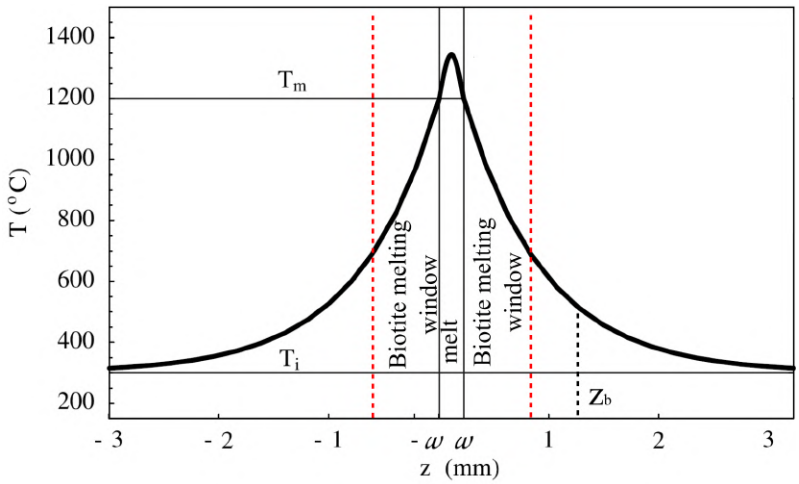

Figure 5.7: Temperature distribution in the melt and in the host rock during pseudotachylyte generation at steady state, with ambient conditions similar to those found in the GLFZ. Red dashed lines represent the distance where $T = T_{biotite\ melting}$. Modified from Nielsen et al. (2008).

ary curve does not fit the experimental trend. A thermal boundary curve with $A \approx 5000$, for example, better suits the experimental dataset. Given that ρ, L and c should not change, and that in an experimental environment T_i can be set to 20°C, thus increasing A, one possibility of decreasing A by an order of magnitude is to set $\kappa \approx 5 \times 10^{-7}$. This could be accomplished by considering that in the high velocity friction experiments the rock samples are in contact with air, which is a good insulator.

Moreover, a relevant parameter that determines the thermal boundary is the slip rate $\dot{u}$. Slip rate was assumed to be constant and on average circa 1 $\frac{m}{s}$ in the natural seismic slip events that produce friction melts and pseudotachylytes. However, $\dot{u}$ evolves abruptly in natural faults. In fact, as the seismic rupture tip propagates at 3 or more km/s along the fault patch, the wall rocks initially at rest are abruptly (in few micro to milliseconds) accelerated up to 10-100 m/s and then rapidly decelerated to few tens of cm/s or less for most of the coseismic slip. These abrupt accelerations and decelerations have been only recently investigated in laboratory experiments (e.g., Harbord et al., Geophysical Research Letters under review) and their impact on the micro-roughness evolution associated to melt generation and heat diffusion during seismic slip is not quantified yet.

Another explanation for different ω_0 values for experimental versus natural pseudotachylyte-host rock boundaries could be related to scaling issues. Natural pseudotachylyte-bearing faults are up to kilometers long, while the experimental faults are 0.10-0.15 meters long (the circumference of the sample). In fact, the amplitude of fault waviness or roughness scales with fault length (e.g., Bistacchi et al., 2011). Since experimental samples are small (and also polished to avoid vibrations of the experimental machine), their initial roughness is only few tens of micrometers over 0.15 meters at most (Castagna, 2012). Instead, in natural pseudotachylytes, when the rupture tip propagates and breaks the rocks the newly formed (and to be polished by the processes associated to frictional power dissipation) fault surfaces have a roughness with an amplitude of circa 1 cm over 0.15 meters of fault length (Bistacchi et al., 2011). As a consequence, it may not be surprising that the pseudotachylyte-host rock boundaries of experimental faults are systematically smoother than those of natural faults.

According to my analysis of the full dataset, an ideal case for discussing the relationship between micro-roughness and frictional power dissipation is the fault L05 (see table 4.1).

In the case of sample L05-08 from a neutral domain, based on SEM-BSE and SEM-CL images, the northern pseudotachylyte-wall rock boundary was poorly affected by damage associated with rupture propagation, while the southern block was heavily damaged (Figure 5.3). This is consistent with the evidence that most coseismic fault damage in the faults of the Lobbia area occurred in the southern side of the bounding wall rocks (Di Toro et al., 2005a). As in sample L05-08, I can likely assume that less intense damaging occurred over the entire northern block along this 5 meters-long fault segment. If this would be the case, the northern pseudotachylyte-host rock micro-roughness was mainly controlled by melting processes.

Based on this assumption, since there is an inverse trend between ω_0 and frictional dissipated power (Figure 5.6), I can estimate the frictional dissipated power from $2\omega_0$ using the distance from the pseudotachylyte-wall rock boundary of two significant isotherms (800°C, approximately the melting point for biotite; 1200°C, approximately the melting point for plagioclase) associated to seismic slip under steady-state conditions (see Equation 1.10. Note that since ω_0 is the root mean square of the deviation from a reference line, doubling ω_0 should give the average amplitude of the micro-roughness of the boundary, Figure 1.6). In Figure 5.8 I plotted the $2\omega_0$ values of the northern pseudotachylyte-host rock boundary of fault L05 with respect to the 800°C and 1200°C isotherms. These two isotherms should correspond to the 400°C temperature window over which selective melting of biotite is dominant in the wall rock and over which the micro-roughness evolution is controlled by heating associated to frictional power dissipation (Figure 1.5).

The plotted data show that frictional dissipated power is (1) considerably higher than the one estimated previously based on the estimates of $\dot{u}$=1 $\frac{m}{s}$ and τ_{ave}=50, 70 and 100 MPa (Griffith et al., 2010; Castagna, 2012), (2) about one order of magnitude larger than the one measured in experimental samples with the same roughness and (3) up to 15 times larger than the one estimated from the micro-roughness with the lowest measured $2\omega_0$ (i.e., sample L05-06; Figure 4.5b). However, for these low ω_0 values the shift between 800 and 1200°C isotherms is about 400 $\frac{MW}{m^2}$. By plotting the 800 and 1200°C isotherms, we are assuming that frictional heating only melts biotite on the wall rocks, while plagioclase is melted in the friction melt, where is carried as clasts.

This latter estimate does not consider the structural domain and is based only on the

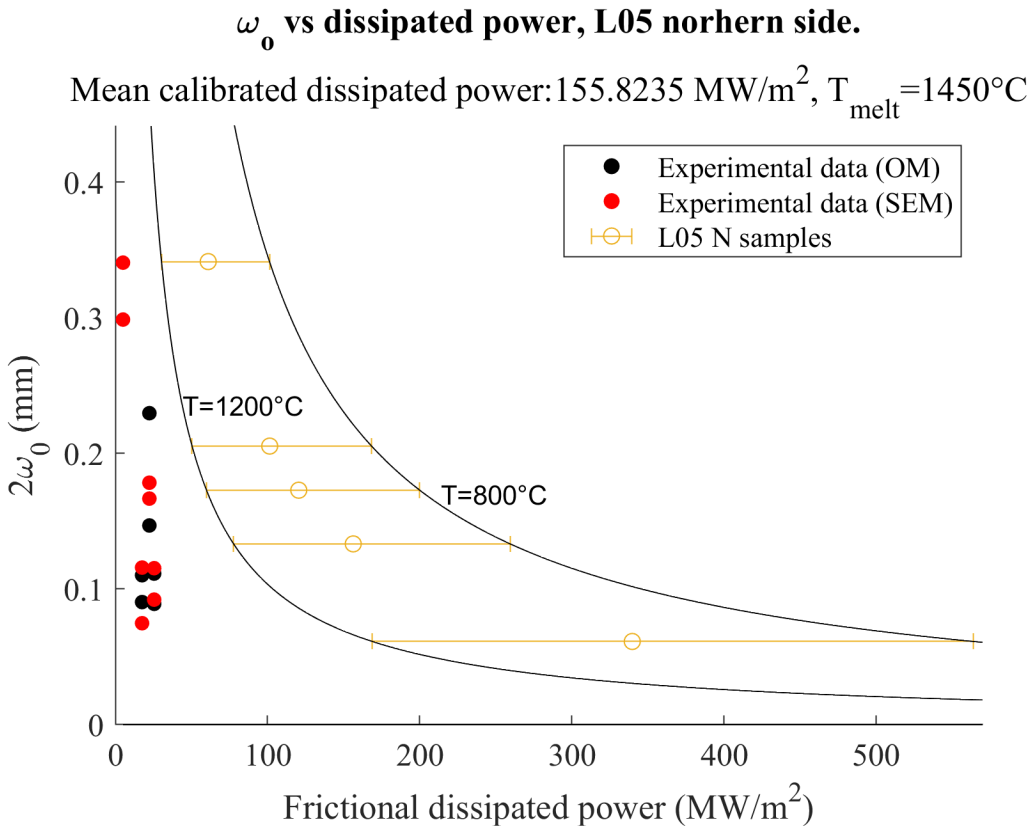

Figure 5.8: Estimated frictional dissipated power for the northern side of L05 fault. Note that frictional dissipated power is considerably higher than the estimates in Figure 5.6.

assumption that melting is controlled by the spatial distribution of the isotherms in the host rock, since there are no microstructural evidences for other processes acting on these samples.

Fault L05 is an ideal case, with an excellent outcrop exposure and limited presence of cataclasite in the host rock. SEM images confirmed that the northern side was not heavily damaged during both the rupture propagation nor the coseismic slip, so that the roughness of this side of the fault can be used to estimate frictional dissipated power with the theoretical model presented in Section 1.2.3.

The average frictional dissipated power on fault L05 is 156±90 $\frac{MW}{m^2}$, with a minimum value of 61±35 $\frac{MW}{m^2}$ for sample L05-04 and a maximum value of 340±224 $\frac{MW}{m^2}$ on sample L05-06 (Figure 4.5b).

Such high values of frictional dissipated power could be caused by a local $\dot{u}$ much higher than 1 $\frac{m}{s}$, since it is unlikely that τ_{ss}, which is the other parameter contributing to $\dot{Q}$, could vary by more than a factor of three along the L05 fault (see numerical model in Griffith

et al., 2010).

In conclusion, I show in this thesis that there is an inverse relationship (Figures 5.4a and 5.6) between the main parameter describing micro-roughness, ω_0, and the frictional dissipated power, though the scaling between natural and experimental pseudotachylytes is hindered by:

1. pivotal role played by rupture propagation (which is absent in the experimental simulations) in controlling the micro-roughness evolution;

2. for a given fault length (e.g., 15 cm) the larger initial roughness of natural faults with respect to experimental ones.

However, for near-ideal faults like L05 it is possible to estimate the frictional dissipated power directly applying the theoretical model, which yielded values of $\dot{Q}$ ranging from 100 to 500 $\frac{MW}{m^2}$, with an average value of 156$\pm$90 $\frac{MW}{m^2}$ (Fig. 5.8). Such large estimated values of frictional dissipated power could be related to very high and short in duration seismic slip rates.

Chapter 6

Conclusions

In this thesis I attempted to estimate the frictional dissipated power ($\dot{Q} = \mu_{ss}\ \sigma_N\ \dot{u}$) on natural wavy, pseudotachylyte-bearing faults using the micro-roughness of their contact with the wall rocks, motivated by the theoretical relationship based on selective melting of minerals, proposed in Nielsen et al. (2010) (Section 1.2.3) and the promising results in Castagna (2012).

In fact, experimental results in Castagna (2012) proved that the theoretical model worked for artificial pseudotachylytes (i.e., micro-roughness amplitude decreased with frictional dissipated power, section 1.2.6), but natural samples did not show a clear relationship (Figure 1.9d). One reason was probably related to the limited natural pseudotachylytes dataset; another one was that the interpretation of the micro-roughness required a dedicated microstructural analysis to discriminate roughness induced by rupture propagation from the one due to selective melting (see section 5.1). Moreover, the MATLAB®script used in Castagna (2012) to calculate micro-roughness parameters had some bugs and required improvements, as the filter applied to remove short-wavelength asperities introduced some artifacts to the pseudotachylyte-wall rock profiles (Section 2.2.2 and Figure 2.4b).

For the reasons mentioned above, I carried out a field survey to collect new samples of pseudotachylyte hosted in tonalite from the Gole Larghe Fault Zone (Adamello, southern alps, Section 3.1.2, Di Toro and Pennacchioni, 2004) and also included in my analysis well-selected samples studied in a previous works for other purposes (Griffith et al., 2010) and where micro-roughness parameters were not measured yet. As in Castagna (2012), the selected pseudotachylyte specimens were collected from injection veins (these are Mode 1

cracks, with no shear deformation and negligible frictional dissipated power), extensional, neutral and compressional structural domains which should roughly record increasing frictional dissipated power during natural earthquakes (Figure 1.7). This selection resulted in a dataset of 22 thin sections, which I studied under the optical microscope to investigate the processes that contribute to the development of the pseudotachylyte-wall rock boundary micro-roughness (section 4.1).

My analysis shows that natural pseudotachylytes are affected by multiple processes besides differential melting. Since seismic faulting is not the first deformative event that affected the rocks, several samples have preexisting cataclasites and pressure-solution stylolithic surfaces that complicate the structure of the pseudotachylyte-host rock boundary (Figure 4.3e) and ease the detachment of large rock fragments (Figures 4.4a), respectively. Moreover, rupture tip propagation intensely fractures or even pulverizes the rock (Figure 5.3d) and generates cataclasite patches that might fill embayments or might be transported in the melt (Figure 5.1), thus directly affecting the micro-roughness.

Because of these three processes influencing the pseudotachylyte-host rock profile, selective melting effects predicted by the theoretical model (Nielsen et al., 2010) are visible only on samples without cataclasites at the pseudotachylyte-host rock boundary.

To calculate the micro-roughness parameters ω_0 and λ_{ave}, I revised the MATLAB®script used in Castagna (2012) by performing a careful analysis to find problems (section 2.2.2). Debugging lead to the exclusion of the filter that was supposed to remove the shorter wavelength asperities, but only altered the real profile (Figure 2.4c). Moreover, I automatized the script to automatically save all the needed figures, build a table with the parameters values and automatically analyze all the profiles (See Section 2.2.2 for description and Appendix A for the full script).

With the revised version of the MATLAB®script I calculated ω_0 and λ_{ave} for all the 56 pseudotachylyte-host rock boundaries (these are about twice the number of studied samples because each pseudotachylyte has, when preserved, two boundaries with the host rocks), including both the natural and experimental profiles studied in Castagna (2012). The dataset shows an inverse trend between ω_0 and fault structural domain (Figure 4.6a), however the data have a large scatter. Based on my interpretation of the microstructures I produced a selected dataset, from where I excluded the profiles or the profile sections in

which rupture processes dominated on selective melting processes. The selected dataset shows considerably lower scatter than the previous one (compare Figure 4.6a with Figure 5.4a). On average, the micro-roughness amplitude described by the parameter ω_0 varies with structural domain (i.e., decreases with increasing frictional dissipated power).
An approximative estimate of the frictional dissipated power on the natural faults, based on their structural domain (Figure 1.7), allows for the comparison between natural and experimental ω_0 values, since experiments were made under controlled conditions with known $\dot{Q}$ (Figure 5.6). Natural pseudotachylytes have considerably higher characteristic asperity height with respect to experimental samples. However those values are accurate when compared to the thermal boundary distance (i.e., the distance from a thermal perturbation up to which the temperature increase is significant) calibrated on tonalite thermal parameters and mineral composition (Equations 5.1 and 5.2). The difference in micro-roughness for a given estimated frictional dissipated power can be due to:

1. air effect on experimental pseudotachylytes, that increased the thermal gradient during frictional melting, reducing the average asperities height ω_0;

2. different scale and initial roughness between natural and experimental faults;

3. absence of the rupture propagation effects on the experimental samples, that increase the roughness of natural pseudotachylytes;

4. larger slip rates achieved in the natural samples with respect to those imposed in the experiments. This may result in an extremely large frictional dissipated power for few milliseconds;

5. the theoretical model and the experiments are based on steady-state conditions, that are hardly achieved in nature.

The above explanations are not exclusive and could all play a role in generating the higher ω_0 in natural samples, or the lower ω_0 in experimental ones.
SEM images performed on sample L05-08 showed that the southern side of the fault was extremely damaged from the rupture propagation, while the northern side presented few fractures (Figure 5.3). Assuming that this was the case for the entire sampled fault L05

(I studied 6 samples from fault L05 collected from extensional, neutral and compressive domains) and consistently with asymmetric wall rock damage for these faults (Di Toro et al., 2005), I concluded that the northern wall of fault L05 was only shaped by selective melting, allowing me to direct apply the theoretical model (Figure 5.8). The frictional dissipated power estimate for the northern side of fault L05 leads to a much higher $\dot{Q}$ than the values predicted in Figure 5.6. The average value for the fault is 156±90 $\frac{MW}{m^2}$, with a minimum and maximum values of 61±35 and 340±224 $\frac{MW}{m^2}$, respectively. The large error is due to the uncertainties in melting kinetics on such a dynamic and fast-evolving environment and can probably be reduced with future studies regarding friction under non-stationary conditions in pseudotachylytes. In any case, such high average $\dot{Q}$ values can be explained by high local slip rates achieved in the fault patch during seismic slip, that leads to a high thermal gradient perpendicular to the fault surface during seismic slip. Moreover, these first field-based estimates almost overlap with the values (10-100 $\frac{MW}{m^2}$) proposed in Sibson (1980) based on reasonable but not-tested fault mechanics considerations.

In conclusion, pseudotachylyte-wall rock boundary micro-roughness, and in particular the root mean square of height distribution of the profile ω_0, does depend on frictional dissipated power $\dot{Q}$ on natural faults. However, a direct comparison between natural and experimental faults is impossible due to the different scale, environment and processes acting under the natural and experimental conditions. Only for near-ideal natural pseudotachylytes an estimate of $\dot{Q}$ can be done after making some reasonable assumptions, showing that frictional dissipated power on natural faults can be higher than expected.

References

Austrheim, H. and T. M. Boundy (1994). "Pseudotachylytes Generated During Seismic Faulting and Eclogitization of the Deep Crust". In: *Science* 265, pp. 82–83.

Bestmann, M., G. Pennacchioni, S. Mostefaoui, M. Göken, and H. de Wall (2016). "Instantaneous healing of micro-fractures during coseismic slip: Evidence from microstructure and Ti in quartz geochemistry within an exhumed pseudotachylyte-bearing fault in tonalite". In: *Lithos* 254.255, pp. 84–93. DOI: http://dx.doi.org/10.1016/j.lithos.2016.03.011.

Bestmann, M., G. Pennacchioni, S. Nielsen, M. Göken, and H. de Wall (2012). "Deformation and ultrafine dynamic recrystallization of quartz in pseudotachylytebearing brittle faults: A matter of a few seconds". In: *Journal of Structural Geology* 38, pp. 21–38. DOI: http://doi.org/10.1016/j.jsg.2011.10.001.

Bistacchi, A., W. A. Griffith, S. A. F. Smith, G. Di Toro, R. Jones, and S. Nielsen (2011). "Fault roughness at seismogenic depths from LIDAR and photogrammetric analysis." In: *Pure and Applied Geophysics*. DOI: http://doi.org/10.1007/s00024-011-0301-7.

Brack, P. (1981). "Structures in th Southwestern Border of the Adamello Intrusion (Alpi Bresciane, Italy)". In: *Schweiz. mineral. petrogr.* 61, pp. 37–50.

— (1985). "Multiple intrusions - examples from the Adamello Batholith (Italy) and their significance on the mechanisms of intrusion". In: *Memorie della Società Geologica Italiana* 26, pp. 145–157.

Callegari, E. and P. Brack (2002). "Geological map of the Tertiary Adamello batholith (Northern Italy) Explainatory notes and legend". In: *Mem. Sci. Geol.* 54.19–49.

Castagna, A. (2012). "Estimate of frictional power dissipation from natural and experimental faults". In: *Padova Digital University Archive. PADUA thesis*. URL: http://tesi.cab.unipd.it/42482/.

Chester, F. M. and J. S. Chester (1998). "Ultracataclasite structure and friction processes of the Punchbowl fault, San Andreas system, California". In: *Tectonophysics* 295, pp. 199–221.

— (2000). "Stress and deformation along wavy frictional faults". In: *Journal of Geophysical Research* 105.B010, pp. 23, 421–23, 430.

Cowan, D. S. (1999). "Do faults preserve a record of seismic slip? A field geologist's opinion." In: *Journal of structural geology* 21, pp. 995–1001. DOI: https://doi.org/10.1016/S0191-8141(99)00046-2.

d'Alessio, M. A. and S. J. Martel (2004). "Fault terminations and barriers to fault growth". In: *Journal of Structural Geology* 26, pp. 1885–1896. DOI: https://doi.org/10.1016/j.jsg.2004.01.010.

Dempsey, E.D., R.E. Holdsworth, J. Imber, A. Bistacchi, and G. Di Toro (2014). "A geological explanation for intraplate earthquake clustering complexity: The zeolite-bearing fault/fracture networks in the Adamello Massif (Southern Italian Alps)". In: *Journal of Structural Geology* 66, pp. 58–74. ISSN: 0191-8141. DOI: https://doi.org/10.1016/j.jsg.2014.04.009.

Di Toro, G., R. Han, T. Hirose, N. De Paola, S. Nielsen, K. Mizoguchi, F. Ferri, M. Cocco, and T. Shimamoto (2011). "Fault lubrication during earthquakes". In: *Science* 471, pp. 494–499. DOI: https://doi.org/10.1038/nature09838.

Di Toro, G., T. Hirose, S. Nielsen, G. Pennacchioni, and T. Shimamoto (2006). "Natural and Experimental Evidence of Melt Lubrication of Faults During Earthquakes". In: *Science* 311, pp. 647–649. DOI: https://doi.org/10.1126/science.1121012.

Di Toro, G., S. Nielsen, and G. Pennacchioni (2005a). "Earthquake rupture dynamics frozen in exhumed ancient faults". In: *Nature* 436.18, pp. 1009–1012. DOI: https://doi.org/10.1038/nature03910.

Di Toro, G., A. Niemeijer, A. Tripoli, S. Nielsen, F. Di Felice, P. Scarlato, G. Spada, R. Alessandroni, G. Romeo, G. Di Stefano, S. Smith, E. Spagnuolo, and S. Mariano (2010). "From field geology to earthquake simulation: a new state-of-the-art tool to

investigate rock friction during the seismic cycle (SHIVA).” In: *Rendiconti Lincei* 21, pp. 95–114. DOI: https://doi.org/10.1038/nature09838.

Di Toro, G. and G. Pennacchioni (2004). “Superheated friction-induced melts in zoned pseudotachylytes within the Adamello tonalites (Italian Southern Alps)”. In: *Journal of Structural Geology* 26, pp. 1783–1801. DOI: https://doi.org/10.1016/j.jsg.2004.03.001.

— (2005). “Fault plane processes and mesoscopic structure of a strong-type seismogenic fault in tonalites (Adamello batholith, Southern Alps)”. In: *Tectonophysics* 402, pp. 55–80. DOI: https://doi.org/10.1016/j.tecto.2004.12.036.

Di Toro, G., G. Pennacchioni, and S. Nielsen (2009). “Pseudotachylytes and Earthquake Source Mechanics”. In: *Rendiconti Lincei* 94, pp. 87–133. DOI: https://doi.org/10.1016/S0074-6142(08)00005-3.

Di Toro, G., G. Pennacchioni, and G. Teza (2005b). “Can pseudotachylytes be used to infer earthquake source parameters? An example of limitations in the study of exhumed faults.” In: *Tectonophysics* 402, pp. 3–20. DOI: https://doi.org/10.1016/j.tecto.2004.10.014.

Fondriest, M., F. Balsamo, A. Bistacchi, L. Clemenzi, M. Demurtas, F. Storti, and G. Di Toro (2020a). “Structural complexity and mechanics of a shallow crustal seismogenic source (Vado di Corno Fault Zone, Italy)”. In: *Journal of Geophysical Research: Solid Earth* 125.9 (e2019JB018926). DOI: https://doi.org/10.1029/2019JB018926.

Fondriest, M., J. Mecklenburgh, X. Passelegue, G. Artioli, F. Nestola, E. Spagnuolo, M. Rempe, and G. Di Toro (2020b). “Pseudotachylyte Alteration and the Rapid Fade of Earthquake Scars From the Geological Record”. In: *Geophysical Research Letters* 47 (22). DOI: https://doi.org/10.1130/G34641.1.

Fondriest, M., S. A. F. Smith, T. Candela, S. B. Nielsen, K. Mair, and G. Di Toro (2013). “Mirror-like faults and power dissipation during earthquakes”. In: *Geology* 41 (11), pp. 1175–1178. DOI: https://doi.org/10.1130/G34641.1.

Griffith, W. A., S. Nielsen, G. Di Toro, and S. A. F. Smith (2010). “Rough faults, distributed weakening, and off-fault deformation”. In: *Journal of Geophysical Research* 115 (B08409). DOI: https://doi.org/10.1029/2009JB006925.

Guatteri, M. and P. Spudich (1998). “Coseismic temporal changes of slip direction: The effect of absolute stress on dynamic rupture.” In: *Bulletin of the Seismological Society of America* 88.3, pp. 777–789. DOI: http://doi.org/10.1029/2010EO220001.

Gupta, H., S. Nayak, W. Ellsworth, Y. J. B. Rao, S. Rajan, B. K. Bansal, S. Purnachandra, Rao, S. Roy, K. Arora, R. Mohan, V. M. Tiwari, H. V. S. Satyanarayana, P. K. Patro, D. Shashidhar, and K. Mallika (2014). “Probing reservoir-triggered earthquakes in Koyna, India, through scientific deep drilling.” In: *Scientific Drilling* 18, pp. 5–9. DOI: http://doi.org/10.5194/sd-18-5-2014.

Hirose, T. and T. Shimamoto (2005). “Slip-Weakening Distance of Faults during Frictional Melting as Inferred from Experimental and Natural Pseudotachylytes”. In: *Bulletin of the Seismological Society of America* 95.5, pp. 1666–1673. DOI: https://doi.org/10.1785/0120040131.

Ji, W.Q., M.G. Malusà, M. Tiepolo, A. Langone, L. Zhao, and F.Y. Wu (2019). “Synchronous Periadriatic magmatism in the Western and Central Alps in the absence of slab breakoff”. In: *Terra Nova* 31, pp. 120–128. DOI: https://doi.org/10.1111/ter.12377.

John, B.E. and J.D. Blundy (1993). “Emplacement-related deformation of granitoid magmas, southern Adamello Massif, Italy”. In: *Geological Society of America Bulletin* 105, pp. 1517–1541.

Kame, N., J. R. Rice, and R. Dmowska (2003). “Effects of prestress state and rupture velocity on dynamic fault branching”. In: *Journal of Geophysical Research* 108.B5 (2265). DOI: https://doi.org/10.1029/2002JB002189.

Kanamori, H. and L. Rivera (2006). “Energy partitioning during an earthquake”. In: *Geophisical Monograph Series* 170, pp. 3–13. DOI: https://doi.org/10.1029/170GM03.

Li, H., H. Wang, Z. Xu, J. Si, J. Pei, T. Li, Y. Huang, S. R. Song, L. W. Kuo, Z. Sun, M. L. Chevalier, and D. Liu (2013). “Characteristics of the fault-related rocks, fault zones and the principal slip zone in the Wenchuan Earthquake Fault Scientific Drilling Project Hole-1 (WFSD-1).” In: *Tectonophysics* 584, pp. 23–42. ISSN: 0040-1951. DOI: https://doi.org/10.1016/j.tecto.2012.08.021.

Martin, S., M. Zattin, A. Del Moro, and P. Macera (1996). "Chronologic constraints for the evolution of the Giudicarie belt (Eastern Alps, NE Italy)". In: *Memorie della Società Geologica Italiana* 10, pp. 60–79. DOI: https://doi.org/10.1046/j.1365-3121.1998.00119.x.

Mckenzie, D. and J. N. Brune (1972). "Melting on Fault Planes During Large Earthquakes". In: *Geophysical Journal of the Royal Astronomical Society* 29, pp. 65–78. DOI: https://doi.org/10.1111/j.1365-246X.1972.tb06152.x.

Mitchell, T. M., V. Toy, G. Di Toro, J. Renner, and R. H. Sibson (2016). "Fault welding by pseudotachylyte formation." In: *Geology* 44.12, pp. 1059–1062. DOI: https://doi.org/10.1130/G38373.1.

Mittempergher, S., G. Pennacchioni, and G. Di Toro (2009). "The effects of fault orientation and fluid infiltration on fault rock assemblages at seismogenic depths." In: *Journal of Structural Geology* 31, pp. 1511–1524. DOI: http://doi.org/10.1016/j.jsg.2009.09.003.

Mittempergher, S., A. Zanchi, S. Zanchetta, M. Fumagalli, K. Gukov, and A. Bistacchi (2021). "Fault reactivation and propagation in the northern Adamello pluton: The structure and kinematics of a kilometre-scale seismogenic source". In: *Tectonophysics* 806 (228790). DOI: https://doi.org/10.1016/j.tecto.2021.228790.

Ngo, D., Y. Huang, A. Rosakis, W. A. Griffith, and D. Pollard (2012). "Off-fault tensile cracks: A link between geological fault observations, lab experiments, and dynamic rupture models." In: *Journal of Geophysical Research* 117 (B01307). DOI: http://dx.doi.org/10.1029/2011JB008577.

Nielsen, S., G. Di Toro, and W.A. Griffith (2010). "Friction and roughness of a melting rock surface". In: *Geophisical Journal International* 182, pp. 299–310. DOI: https://doi.org/10.1111/j.1365-246X.2010.04607.x.

Nielsen, S., G. Di Toro, T. Hirose, and T. Shimamoto (2008). "Frictional melt and seismic slip". In: *Journal of Geophysical Research* 113 (B01308). DOI: https://doi.org/10.1029/2007JB005122.

Nielsen, S. and L. Knopoff (1998). "The equivalent strength of geometrical barriers to earthquakes". In: *Journal of Geophysical Research* 103.B5, pp. 9953–9965.

Pennacchioni, G., G. Di Toro, P. Brack, L. Menegon, and I.M. Villa (2006). "Brittle–ductile–brittle deformation during cooling of tonalite (Adamello, Southern Italian Alps)". In: *Tectonophhysics* 427, pp. 191–197. DOI: https://doi.org/10.1016/j.tecto.2006.05.019.

Pittarello, L., G. Di Toro, A. Bizzarri, J. Pennacchioni G. and Hadizadeh, and M. Cocco (2008). "Energy partitioning during seismic slip in pseudotachylyte-bearing faults (Gole Larghe Fault, Adamello, Italy)". In: *Earth and Planetary Science Letters* 269, pp. 131–139. DOI: https://doi.org/10.1016/j.epsl.2008.01.052.

Poliakov, A. N. B., R. Dmowska, and J. R. Rice (2002). "Dynamic shear rupture interactions with fault bendsand off-axis secondary faulting". In: *Journal of Geophysical Research* 107.B11 (2295). DOI: https://doi.org/10.1029/2001JB000572.

Riklin, K. (1983). "Contact metamorphism of the Permian red sandstones in the Adamello area". In: *Memorie della Società Geologica Italiana* 26, pp. 159–169.

Rowe, C. D. and W. A. Griffith (2015). "Do Faults Preserve a Record of Seismic Slip: A second opinion". In: *Journal of Structural Geology* 78, pp. 1–26. DOI: https://doi.org/10.1016/j.jsg.2015.06.006.

Schaltegger, U., A. Nowak, A. Ulianov, C. M. Fisher, A. Gerdes, R. Spikings, and O. Müntener (2019). "Zircon Petrochronology and 40Ar/39Ar Thermochronology of the Adamello Intrusive Suite, N. Italy: Monitoring the Growth and Decay of an Incrementally Assembled Magmatic System." In: *Journal of Petrology* 60, pp. 701–722. DOI: https://doi.org/10.1093/petrology/egz010..

Scholz, C. H. (2019). *The Mechanics of Earthquakes and Faulting*. Cambridge University Press. ISBN: 9781316681473. DOI: https://doi.org/10.1017/9781316681473.

Sibson, R. H. (1975). "Generation of Pseudotachylyte by Ancient Seismic Faulting". In: *Geophisical Journal of the Royal Astronomical Society* 43, pp. 775–794.

— (1980). "Generation of Pseudotachylyte by Ancient Seismic Faulting". In: *Journal of Geophysical Research* 85, pp. 6239–6247.

— (2003). "Thickness of the seismic slip zone." In: *Bulletin of the Seismological Society of America* 93.3, pp. 1169–1178. DOI: http://doi.org/10.1016/j.jsg.2009.09.003.

Smith, S. A. F., A. Bistacchi, T. M. Mitchell, S. Mittempergher, and G. Di Toro (2013). "The structure of an exhumed intraplate seismogenic fault in crystalline basement". In: *Tectonophysics* 599, pp. 29–44. DOI: https://doi.org/10.1016/j.tecto.2013.03.031.

Spray, J. G. (2010). "Frictional Melting Processes in Planetary Materials: From Hypervelocity Impact to Earthquakes". In: *Annual review of Earth and Planetary Sciences* 38, pp. 221–254. DOI: https://doi.org/10.1016/S0191-8141(99)00046-2.

Stipp, M. and B. Fügenschuh (2004). "Contemporaneous plutonism and strike-slip faulting: A case study from the Tonale fault zone north of the Adamello pluton (Italian Alps)". In: *Tectonics* 23 (TC3004), pp. 191–197. DOI: https//doi.org/10.1029/2003TC001515,.

Stipp, M., R. Stünitz H.and Heilbronner, and S.M. Schmid (2002). "The eastern Tonale fault zone: a 'natural laboratory' for crystal plastic deformation of quartz over a temperature range from 250 to 700 °C". In: *Journal of Structural Geology* 24.1861–1884. DOI: https://doi.org/10.1016/S0191-8141(02)00035-4..

Swanson, M. T. (1991). "Fault structure, wear mechanisms and rupture processes in pseudotachylyte generation". In: *Tectonophysics* 204, pp. 223–242.

Zoback, M., S. Hickman, and W. Ellsworth (2010). "Scientific drilling into the San Andreas Fault Zone." In: *Eos* 91.22, pp. 97–204. DOI: http://doi.org/10.1029/2010EO220001.

Appendix A

MATLAB®script

```
%% roughness parameter computation (wo and lambda) from a .xyz file
    (raw coordinates). Modified and refined from W.A. Griffith
%3 loading modes:
%-single file: use rows 17:20 to test script. Remove for cycles,
    see comments.
% -natural samples: two for loops to automatically analyze
% the whole natural dataset. Uncomment 23:26 for sample
% name list and 38:56 for data loading
% -experimental samples: as for natural samples. uncomment
% 29:31, 41, 48, 52.
%data definition and loading sections are messy but time-saving
    when analysing whole dataset
clear all
close all
clc

ext='.xyz'; %file extension
row=16; %first row for excel data writing

%% 1 data loading

% % single file loading: use to test script
% % fname='L09-03b';
% % or='N'; %N, S, W or E vein sides
```

```
22 % % path=['D:\tesi magistrale\profiles\', fname]; %uncomment for
       single file loading
23 % % data = load([path,'\',fname,or,ext]); %load single .xyz profile
24 % % scale=32.52;
25
26 %%%%%%%%%%%%%%%%%%%%%%%% Natural dataset loading
       %%%%%%%%%%%%%%%%%%%%%%%%
27 fname=["A1" "A02-02", "A02-04","A2", "A4", "A5", "A7", "L05-02", "
       L05-03", "L05-04",...
28 "L05-06", "L05-07", "L05-08", "L09-01a", "L09-01b", "L09-02a",...
29 "L09-02b", "L09-03a", "L09-03b", "W05-S01", "W05-S04", "W09-S01"];
30 scale=[20.04, 19.06, 16.51, 16.58, 34.20, 32.21, 34.52, 32.55,
       33.67, 33.26, ...
31 32.5, 31.27, 32.7, 30.78, 15.59, 19.01, 17.21, 16.95, 19.57, 19.6,
       16.91, ...
32 6.68, 18.96, 19.91, 32.86, 32.87, 33.92, 33.31, 23.84, 18.24,
       15.48, ...
33 11.12, 32.52, 32.37, 16.38, 11.15, 27.07, 23.63, 31.57, 17.51,
       30.27, 31.88];
34 count=0;
35 for f=1:length(fname) %for loop for every sample, comment for
       single file loading (remember end)
36 path=append('D:\tesi magistrale\profiles\', fname(f)); %path for
       multiple file loading
37 %    natural samples orientation
38 if f==1||f==4||f==20  %injection veins orientation
39 or=["E", "W"];
40 elseif f==8 || f==9
41 or=["O"];
42 else
43 or=["N","S"]; %fault veins orientation
44 end
45 for o=1:length(or) %for loop for every side of the sample (remember
       end)
46 count=count+1;
47 if f==8||f==9 %single-side sections
```

```
48      data = load(append(path,'\',fname(f),ext)); %import .xyz
            profile for single side sections
49  else
50      data = load(append(path,'\',fname(f),or(o),ext)); %import
            multiple .xyz profile
51  end
52  %
    %%%%
```

```
75 %rotate profile
76 num = length(x);
77 rot = atan((y(1)-y(num))/(x(1)-x(num)));%figure out rotation angle
       by finding slope of overall trend line
78 x = x*cos(rot)+y*sin(rot); y = -x*sin(rot)+y*cos(rot);%rotate so
       that fault tips end at the same f
79 x = x-min(x); %translate x-origin to x=0
80 y = y-mean(y);%translate y-origin to mean y
81
82 % plot initial fracture profile
83 figure(1)
84 clf
85 plot(x,y)
86 xlabel('x (mm)')
87 ylabel('y (mm)')
88 title('Loaded profile')
89 axis equal
90
91 %% 3 profile elaboration
92
93 %resort data so that datapoints are increasing in x (not necessary)
94 XY = sortrows([x y]);
95 x1 = XY(:,1); y1 = XY(:,2);
96
97 %differentiate points with the same x (made during drawing)
98 for m = 1:length(x1)-1
99     if x1(m)==x1(m+1)
100         x1(m+1)=x1(m)+0.1*mean(diff(x1));
101     end
102 end
103
104 % plot data after sorting
105 figure(2)
106 clf
107 plot(x1,y1)
108 xlabel('x (mm)')
109 ylabel('y (mm)')
```

```
110 title('fracture profile after sorting')
111 %plot reference line and overall profile trend
112 X = [ones(length(x1),1) x1];
113 m = lscov(X,y1); %least square with known covariance, find ovewrall
        slope
114 yt=m(2).*x1+m(1); %overall slope
115 ref =mean(y1); %average y value
116 rl=ref+zeros(length(x1)); %vector for reference line plotting
117 hold on
118 plot(x1, rl, 'k')
119 legend('fracture profile', 'reference line')
120 axis equal
121 hold off
122
123 %calculate deviation of profile from reference line
124 z_rough=y1-ref;
125
126 figure (3)
127 clf
128 plot(x1,z_rough)
129 xlabel('x (mm)')
130 ylabel('z (mm)')
131 % title([fname, or, ' Deviation from Reference Line'])%title for
       single sample
132 title(append(fname(f), or(o), ' Deviation from Reference Line'))%
       title for multiple samples
133 axis equal
134 exportgraphics(gcf,append(path,'/',fname (f),or (o), 'profile.png')
       , 'resolution', 300) %save to sample folder
135 exportgraphics(gcf,append('D:\tesi magistrale\profiles\charts\',
       fname (f), or (o), 'profile.png'), 'resolution', 300)
136
137 %calculate wo from height distribution
138 [H1, X] = hist(z_rough, 20);
139 wo = sqrt(1/length(z_rough)*sum(z_rough.^2));
140 %bar graph representing asperities height distribution
141 figure (4)
```

```
142 barh(X, H1)
143 ylabel('z (mm)')
144 xlabel('N')
145 % title(append(fname, or,' \omega_o = ', num2str(wo), ' +/-',
        num2str(std(z_rough))));
146 title(append(fname(f), or(o),' \omega_o = ', num2str(wo),' mm')); %
        use with multiple samples
147 exportgraphics(gcf,append(path,'/',fname (f),or (o), 'wo.png'), '
        resolution', 300) %save to sample folder
148 exportgraphics(gcf,append('D:\tesi magistrale\profiles\charts\',
        fname (f),or (o),'wo.png'), 'resolution', 300)
149
150 %% 4 profile filtering and interpolation
151
152 %FILTERING CAUSES PROBLEMS, LEAVE COMMENTED WHEN CALCULATING
        DEFINITIVE DATA
153 %moving average to smooth small variations
154 % lm = 4; %characteristic width of moving window
155 % a=1; %a=1, characteristic height of moving window.
156 % b = (1/lm)*ones(1, lm);
157 % z = filter(b,a,z_rough); %unidimensional filter, moving window is
         b*a
158 z1=z_rough;
159 %interpolate and resample using linear interpolation to get
        uniformly spaced dataset
160 x2 = min(x1):mean(diff(x1)):max(x1); %build uniformly-spaced x-axis
161 z2 = interp1(x1, z1, x2, 'linear');
162 x = x2; z = z2;
163
164 %plot profile after linear interpolation
165 figure(5)
166 plot(x1, z1)
167 xlabel('x (mm)')
168 ylabel('z (mm)')
169 % title(append(fname,or,'  profile after linear interpolation'))
170 title(append(fname(f),or(o),'  profile after linear interpolation')
        ) %use with multiple samples
```

```
171 hold on
172 axis equal
173 figure (6)
174 barh(X, H1)
175 ylabel('z (mm)')
176 xlabel('N')
177 % title(append(fname, or,' \omega_o = ', num2str(wo), ' +/-',
       num2str(std(z_rough)))); %use with multiple samples
178 title(append(fname (f), or (o),' \omega_o = ', num2str(wo), ' +/-',
       num2str(std(z_rough)))); %use with multiple samples
179 exportgraphics(gcf,append('D:\tesi magistrale\Matlab\filter and
       interpolation\interpolated profiles\',fname (f),or (o),'
       profile_vs_w0.png'), 'resolution', 300)
180
181 %% 5 curvature parameters
182
183 %call function lmin.m to find local minima (valleys)
184 [lmval,i]=lmin(z,5); %lmval is the local minima value, i is the x
       position
185 scatter(x(i),z(i)) %check where minima are
186 legend('before interpolation', 'local minima')
187 hold off
188 dcX=zeros (1, length(x)-1);
189 dcZ=dcX;
190
191 %loop to calculate x and z shift between j-1 and j+1
192 for j = 2:length(x)-1
193     dcX(j) = x(j+1)-x(j-1);
194     dcZ(j) = z(j+1)-z(j-1);
195 end
196
197 dcX(1)=mean([dcX(2) dcX(end)]);
198 dcZ(1) = mean([dcZ(2) dcZ(end)]);
199
200 ds = sqrt(dcX.^2+dcZ.^2); %arc length between each pair of adjacent
       points
201 tX = dcX./ds;%x-component of tangent vector between two points
```

```
202 tZ = dcZ./ds;%Z-component of tangent vector between two points
203
204 kZ=zeros (1, length(x)-1);
205 kX=zeros (1, length(x)-1);
206
207 for j = 2:length(x)-2
208     kX(j) = (tX(j+1)-tX(j-1))./ds(j);%x-component of curvature
            vector (2nd space derivative in x direction)
209     kZ(j) = (tZ(j+1)-tZ(j-1))./ds(j);%z-component of curvature
            vector (2nd space derivative in z direction)
210 end
211 kX(1)=1;
212 kZ(1)=1;
213
214 % curvature parameter 1: curvature radius (R)
215
216 kappa = sqrt(kX(i).^2+kZ(i).^2); %scalar curvature calculated at
       minima
217 R = 1./kappa;%radius of curvature calculated at minima
218
219 figure (6)
220 hist(R)
221 xlabel('R (mm)')
222 ylabel('N')
223 title(['R_{ave}= ' num2str(mean(R))]);
224
225 %% 7 lambda_ave
226 %discard wavelengths>1 mm
227 r = 1;
228 while r <= length(R)
229     if R(r) > 1
230         R(r) = [];
231     end
232     r = r+1;
233 end
234
235 lambda = R;
```

```
236 [H2, X] = hist(lambda, 20);
237
238 bar(X, H2, 1)
239 xlabel('\lambda (mm)')
240 ylabel('N')
241 colormap('white')
242 axis square
243 % title([fname, or ', \lambda_{ave}= ' num2str(mean(lambda)) 'mm,
      +/-' num2str(std(lambda))]); %single sample
244 title(append(fname(f), ' ', or(o),' \lambda_{ave} = ', num2str(mean
      (lambda)), ' +/-',num2str(std(lambda)))); %multiple samples
245 exportgraphics(gcf,append(path,'/',fname (f), or (o), 'roughness.
      png'), 'resolution', 300) %save to sample folder
246 exportgraphics(gcf,append('D:\tesi magistrale\profiles\charts\',
      fname (f),or (o),'roughness.png'), 'resolution', 300) %save to
      charts folder
247
248 %% 8 Spectral analysis
249
250 % input parameters
251 dx = mean (diff(x)); % sampling step
252 fs  = 1/dx; % spatial sampling frequency
253 np = length (x); %number of points in profile (length of X)
254 Lx = (0:np-1)*dx;
255 % calcolo transformata e plot spettro:
256 yt = fft(z);
257 P2 = abs(yt/np);
258 P1 = P2(1:np/2+1);
259 P1(2:end-1) = 2*P1(2:end-1);
260 ft = fs*(0:(np/2))/np;
261 wl=1./ft;
262 F = polyfit(log(wl(2:end)),log(P1(2:end)),1);
263
264 figure(9)
265 clf
266 loglog(wl,P1)
267 xlabel ('Wavelength (mm)')
```

```
xlim([8*10^-3 40])
ylabel('Magnitude')
ylim([10^-7 2])
title (append(fname(f),' ', or(o), ' Fourier transform, slope=',
    num2str(F(1))))
% title (append(fname,' ', or, ' Fourier transform spectral
    analysis, slope=', num2str(F(1))))
exportgraphics(gcf,append('D:\tesi magistrale\profiles\charts\
    Spectral analysis\',fname (f),or (o),'spectral.png'), '
    resolution', 300) %save to charts folder

% Write spectral data to text file
T = [wl ;P1];
size(T)
dlmwrite(append('D:\tesi magistrale\profiles\charts\Spectral
    analysis\',fname (f),or (o),'spectral.txt'),T);
dlmwrite(append('D:\tesi magistrale\profiles\charts\Spectral
    analysis\',fname ,or,'spectral.txt'),T);

%% 9 producing a global view of the parameters

global_plot(x,z,wl,P1,lambda,f,o,scale,z_rough,F,fname,or) %
    function producing two figures with all the parameters

%% 10 writing data to excel worksheet

xlsname='Roughness data.xls'; %excel filename
xlswrite(['D:\tesi magistrale\', xlsname], cellstr(append(fname(f),
    or(o))),1,['A',num2str(row)]); %sample name and orientation
xlswrite(['D:\tesi magistrale\', xlsname], mean(lambda),1,['B',
    num2str(row)]); %lambda
xlswrite(['D:\tesi magistrale\', xlsname], std(lambda),1,['C',
    num2str(row)]); %lambda standard deviation
xlswrite(['D:\tesi magistrale\', xlsname], wo,1,['D',num2str(row)])
    ; %w0 calculated on distribution
xlswrite(['D:\tesi magistrale\', xlsname], std(z_rough),1,['E',
    num2str(row)]); %wo standard deviation
```

```
293 xlswrite(['D:\tesi magistrale\', xlsname], wo1,1,['F',num2str(row)
    ]); %w0 calculated on asperities
294 xlswrite(['D:\tesi magistrale\', xlsname], std(z_s),1,['G',num2str(
    row)]); %wo standard deviation
295 xlswrite(['D:\tesi magistrale\', xlsname], F(1),1,['J',num2str(row)
    ]); %fourier spectrum overall slope
296 xlswrite(['D:\tesi magistrale\', xlsname], F(2),1,['K',num2str(row)
    ]); %fourier spectrum intercept
297 row=row+1; %update writing row
298 end %uncomment both end for multiple file loading
299 end
```

Appendix B

Pseudotachylyte-host rock boundary micro-roughness

A1 E

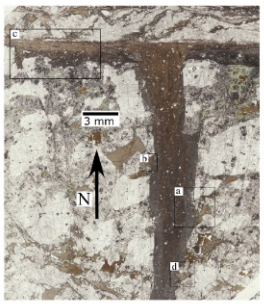

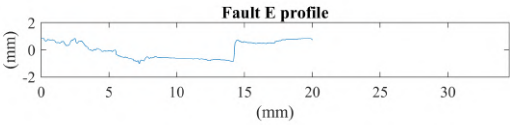

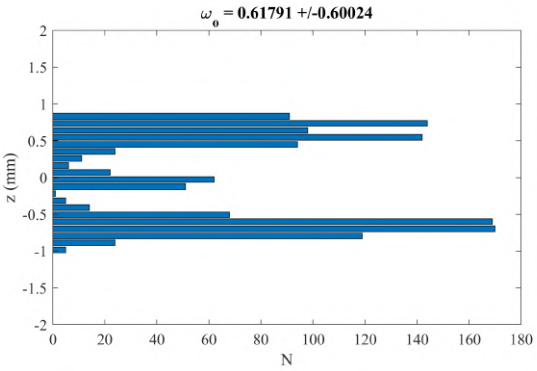

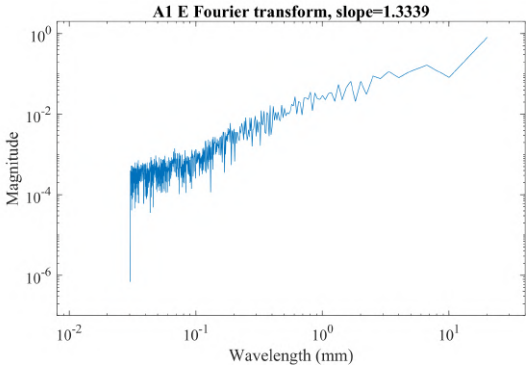

A1 E selected

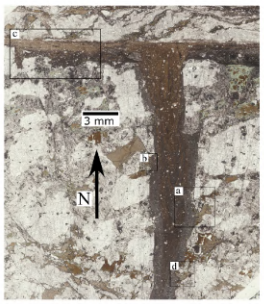

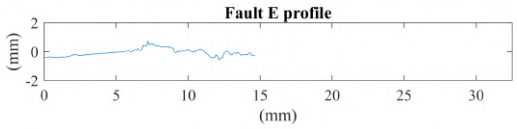

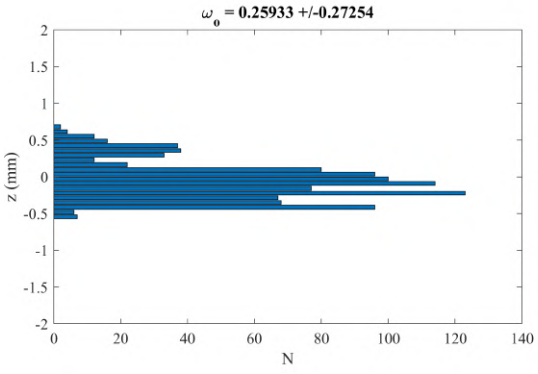

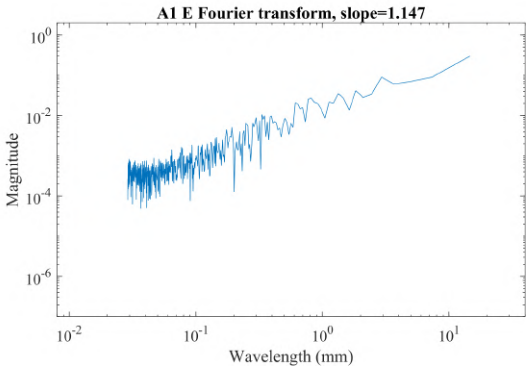

A1 W

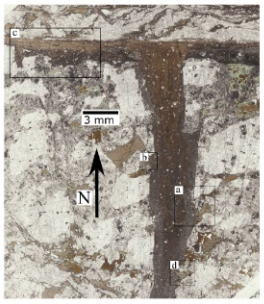

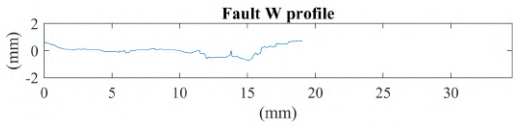

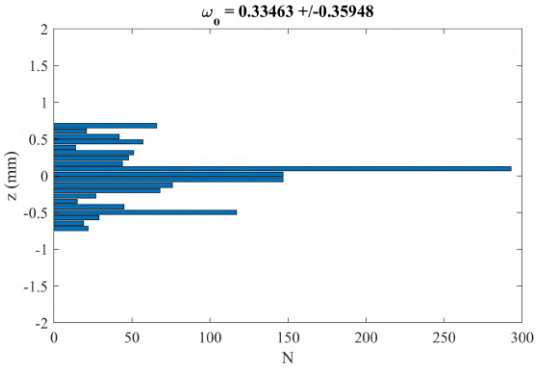

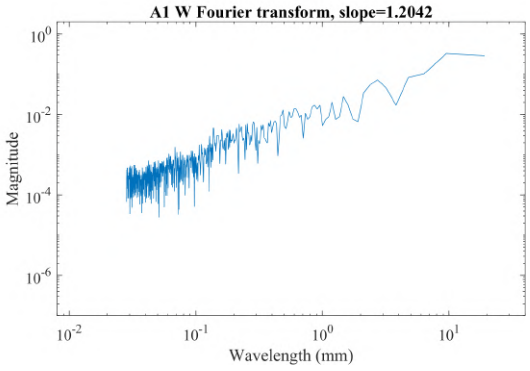

A02-02 N

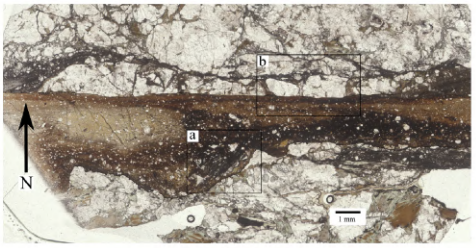

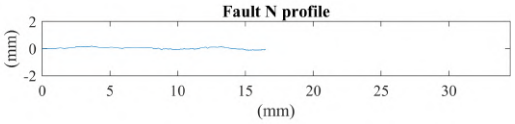

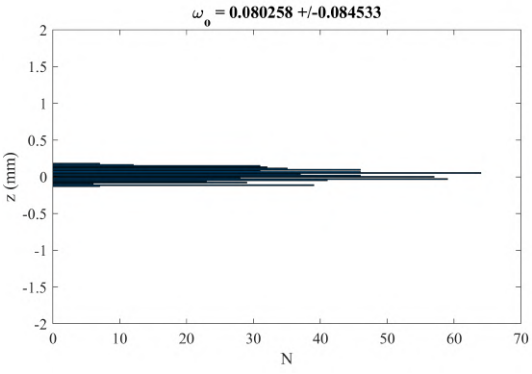

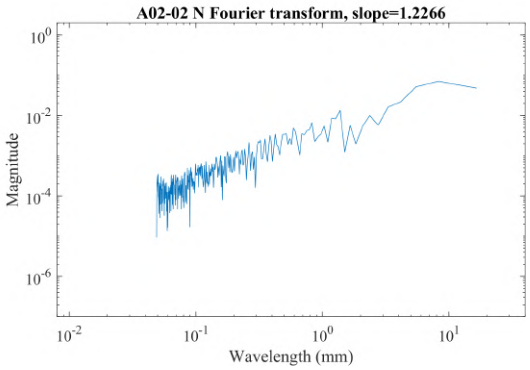

A02-02 S

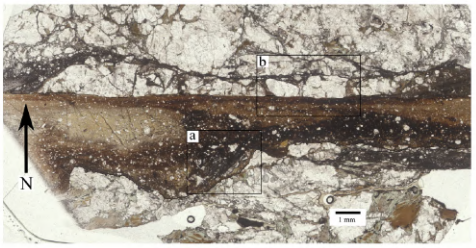

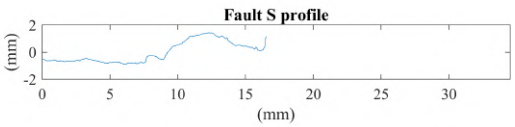

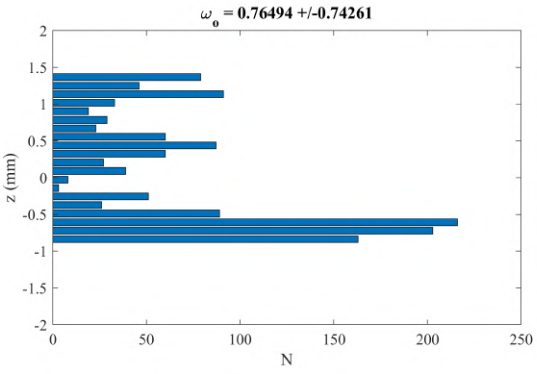

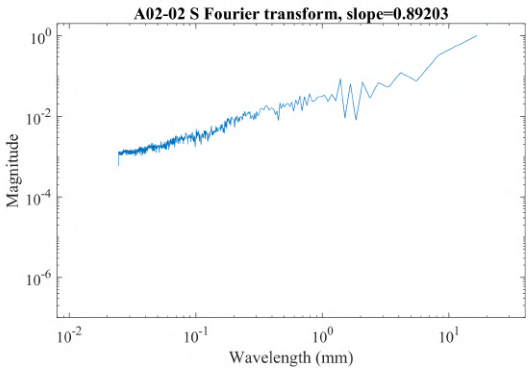

A02-02 S selected

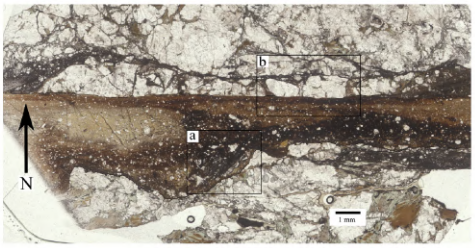

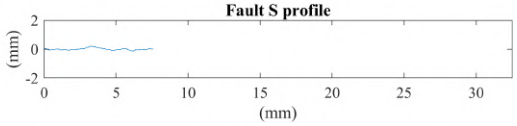

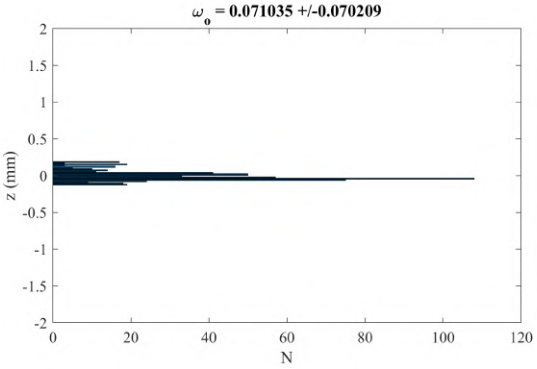

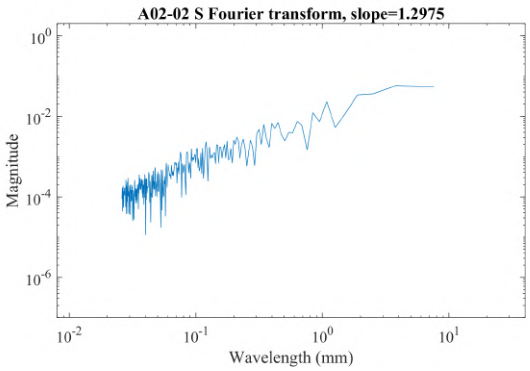

A02-04 N

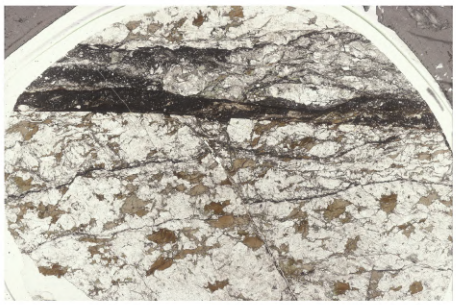

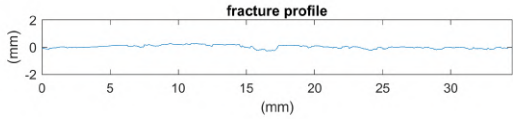

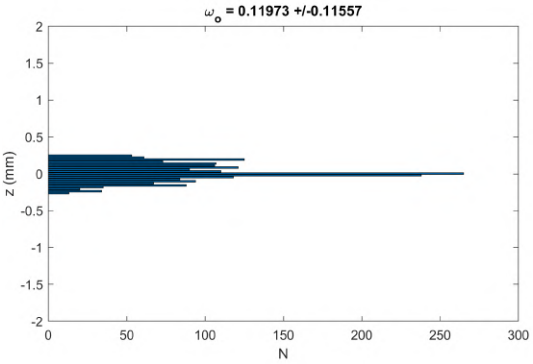

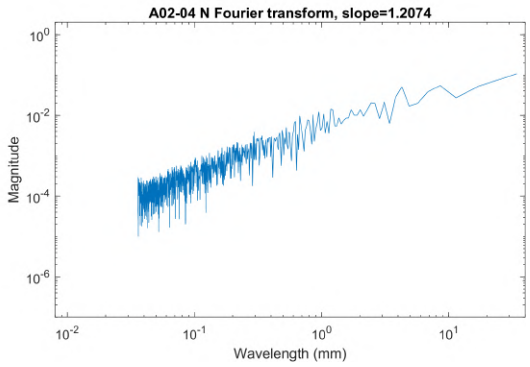

A02-04 S

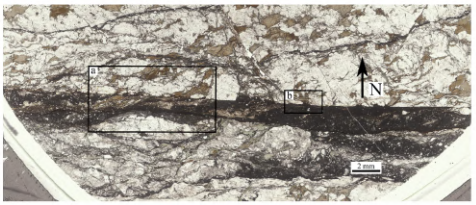
a
b
N
2 mm

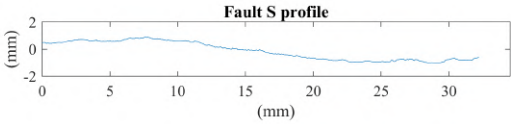
Fault S profile
(mm)
(mm)

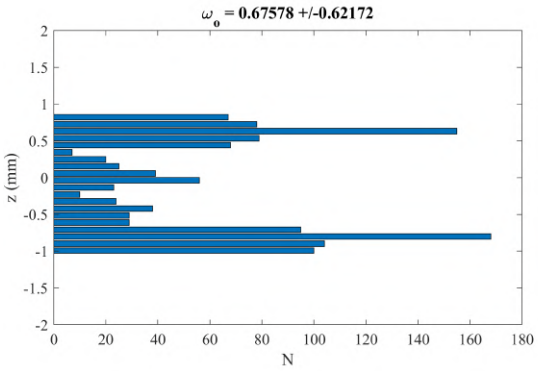
ω o = 0.67578 +/-0.62172
z (mm)
N

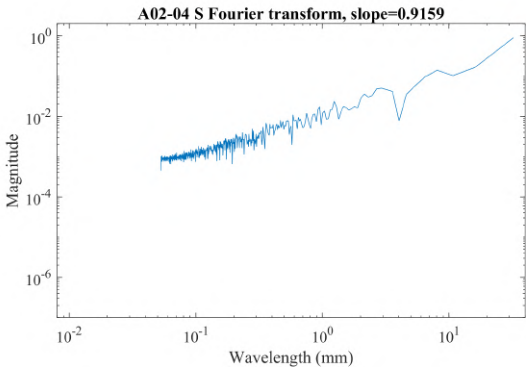
A02-04 S Fourier transform, slope=0.9159
Magnitude
Wavelength (mm)

A2 E

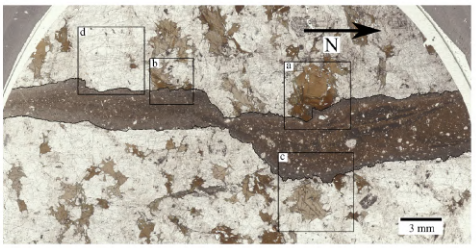
d
b
a
c
N
3 mm

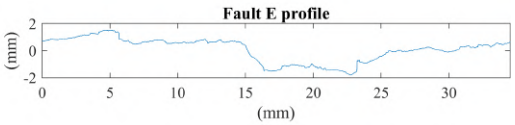
Fault E profile
(mm)
(mm)

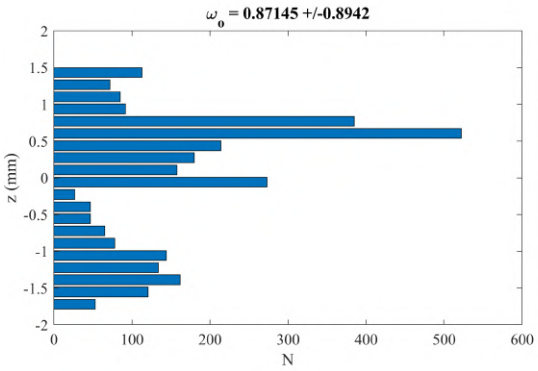
ω o = 0.87145 +/-0.8942
z (mm)
N

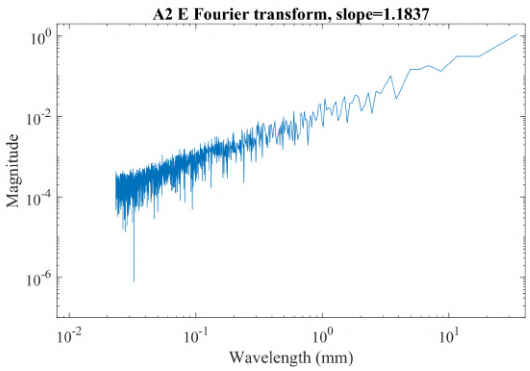
A2 E Fourier transform, slope=1.1837
Magnitude
Wavelength (mm)

A2 W

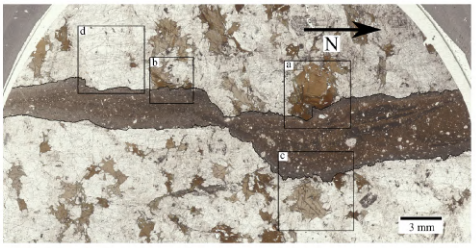
d
b
a
c
N
3 mm

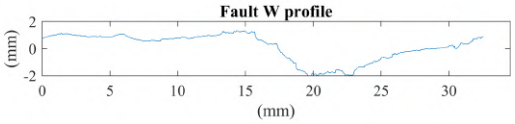
Fault W profile
(mm)
(mm)

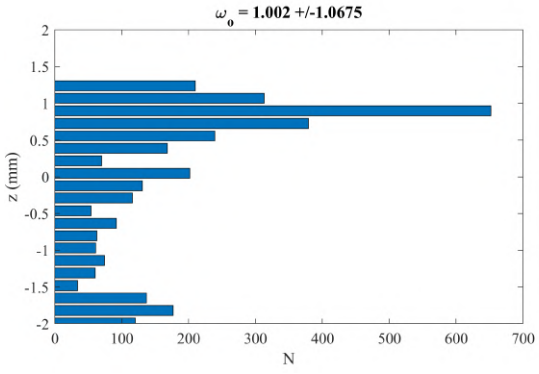
ω_o = 1.002 +/-1.0675
z (mm)
N

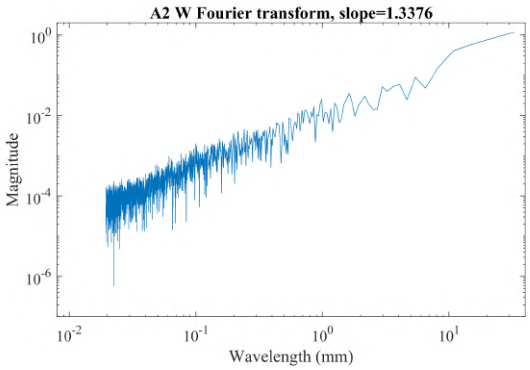
A2 W Fourier transform, slope=1.3376
Magnitude
Wavelength (mm)

A4 N

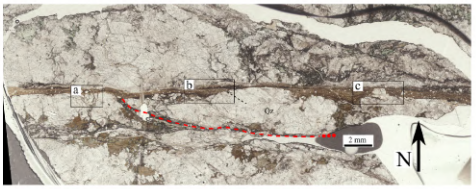
a
b
c
2 mm
N

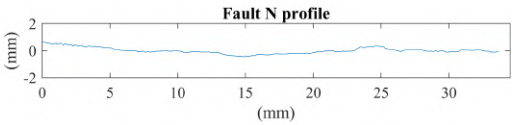
Fault N profile
(mm)
(mm)

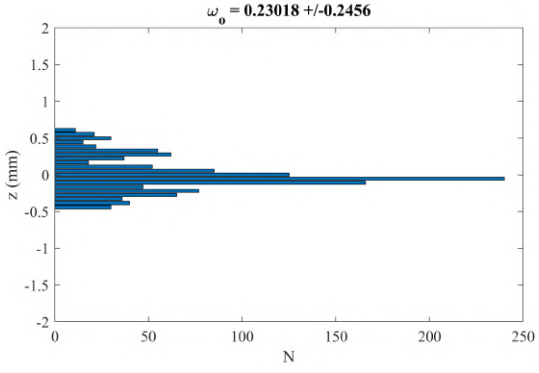
ω_o = 0.23018 +/-0.2456
z (mm)
N

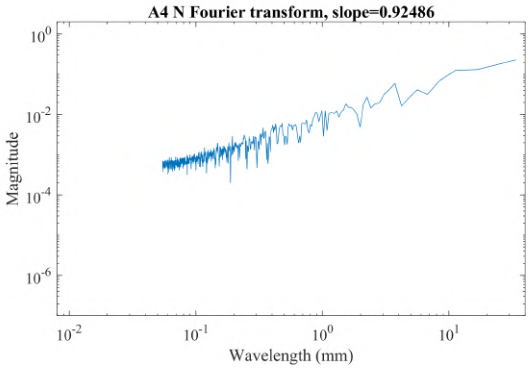
A4 N Fourier transform, slope=0.92486
Magnitude
Wavelength (mm)

A4 S

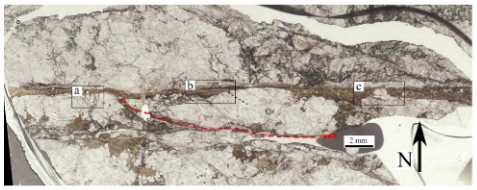
a
b
c
2 mm
N

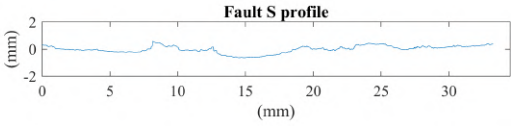
Fault S profile
(mm)
(mm)

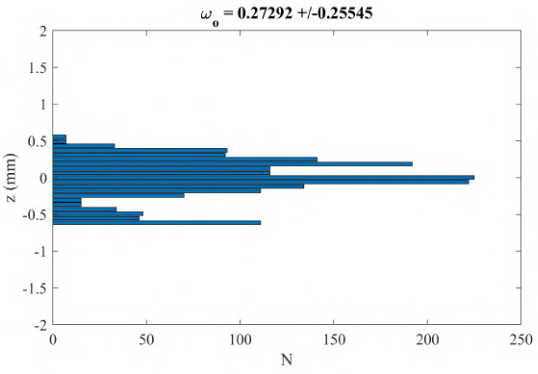
ω_o = 0.27292 +/-0.25545
z (mm)
N

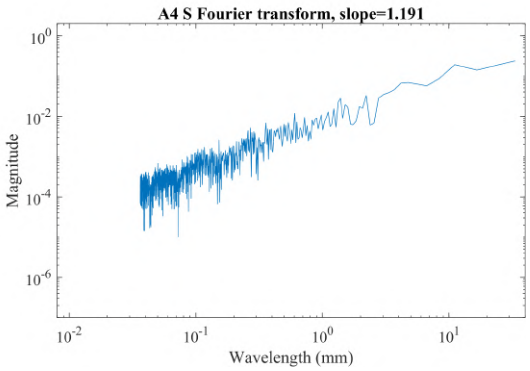
A4 S Fourier transform, slope=1.191
Magnitude
Wavelength (mm)

A5 N

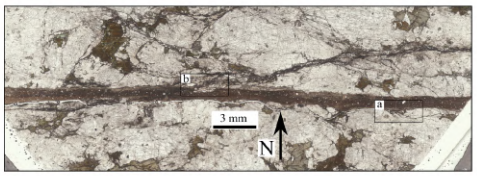
b
3 mm
a
N

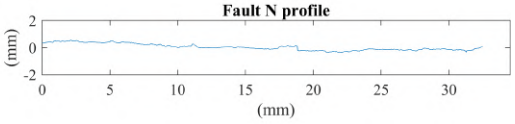
Fault N profile
(mm)
(mm)

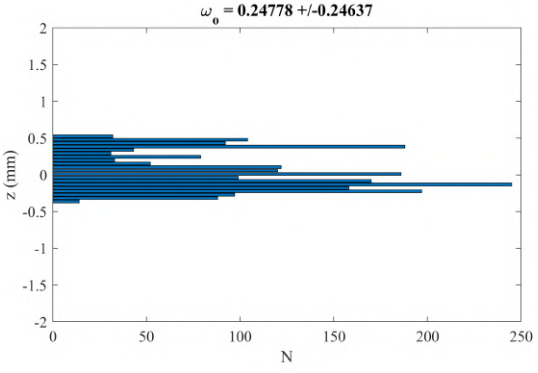
ω_o = 0.24778 +/-0.24637
z (mm)
N

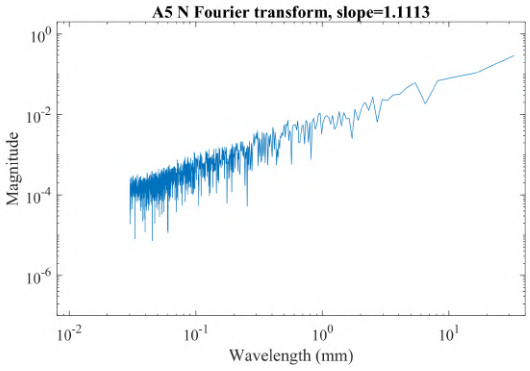
A5 N Fourier transform, slope=1.1113
Magnitude
Wavelength (mm)

A5 N selected

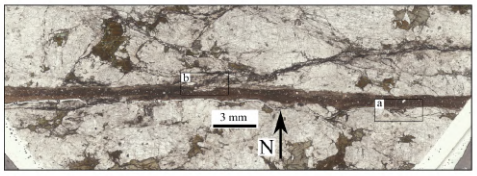

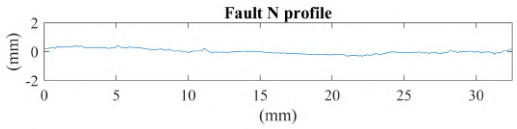

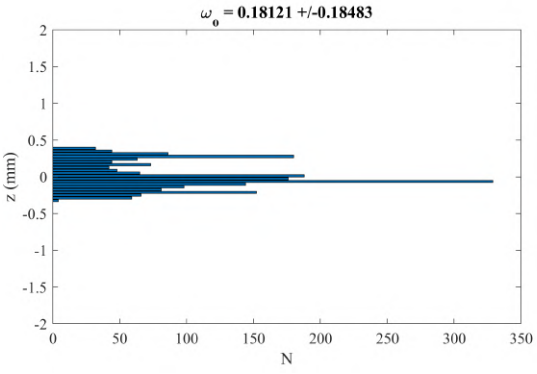

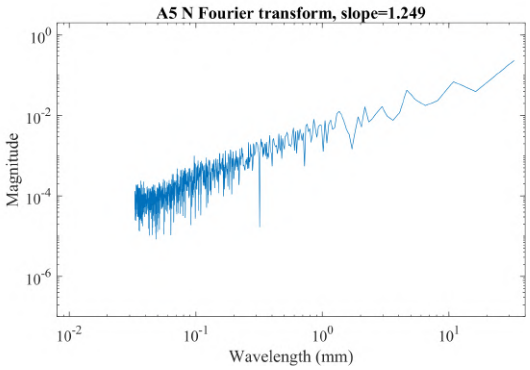

A5 S

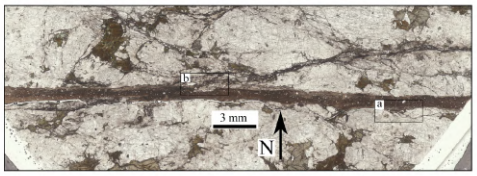

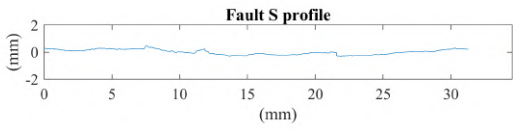

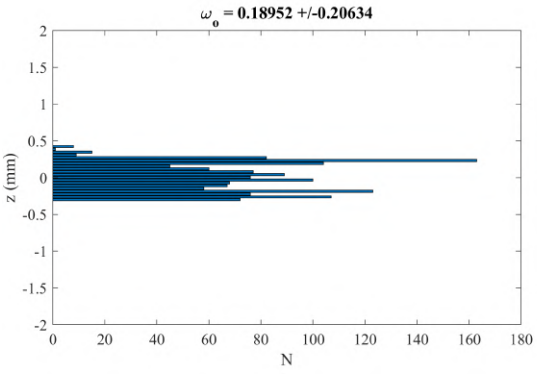

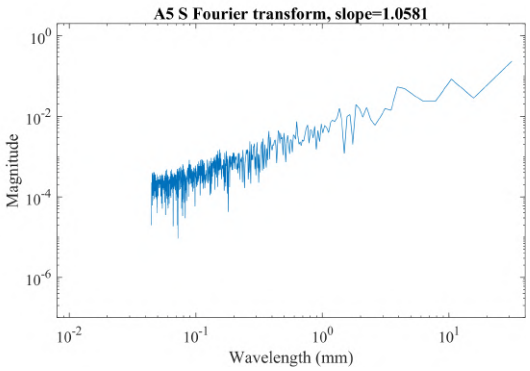

A5 S selected

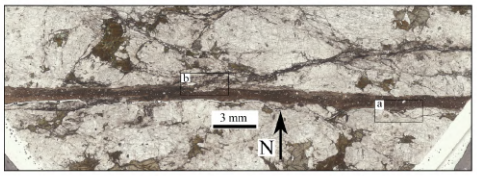

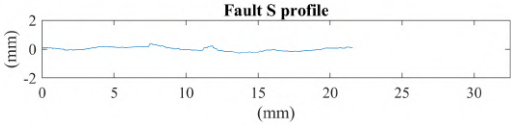

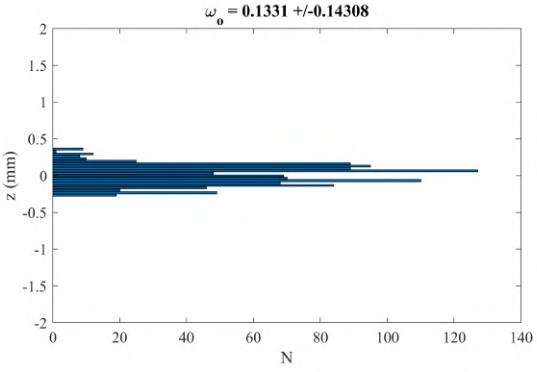

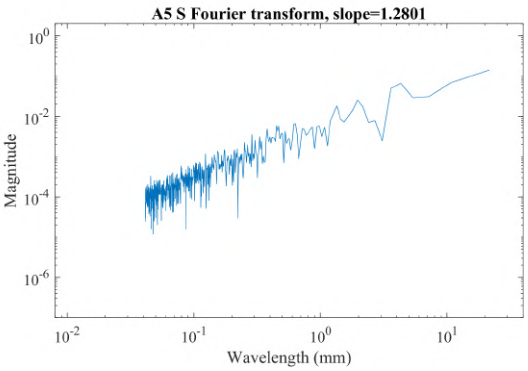

A7 N

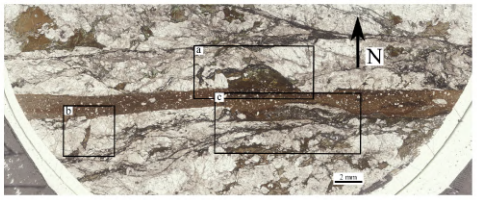

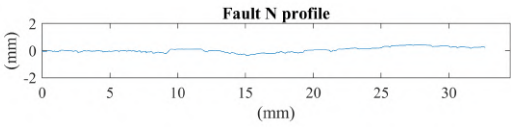

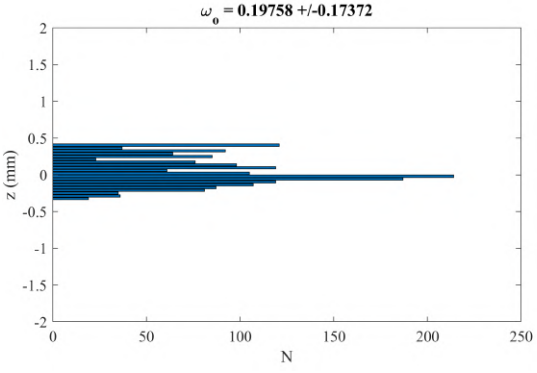

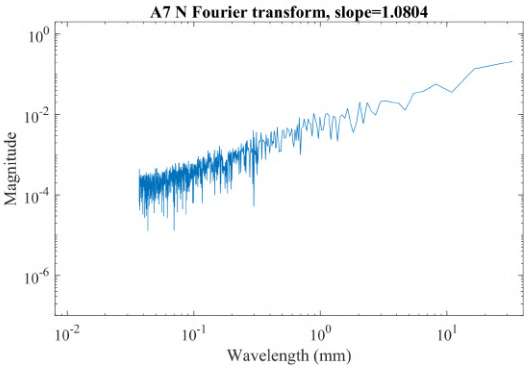

A7 S

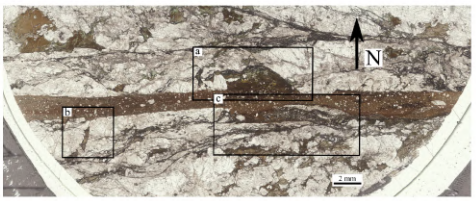

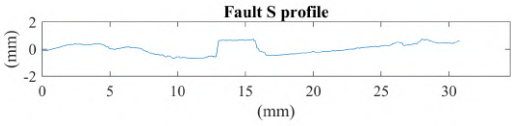

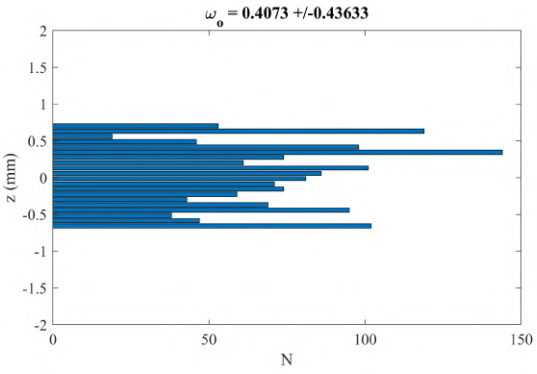

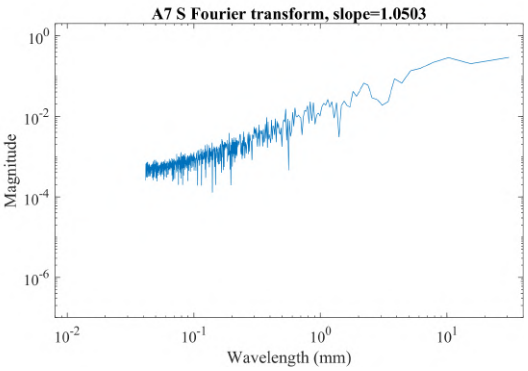

A7 S selected

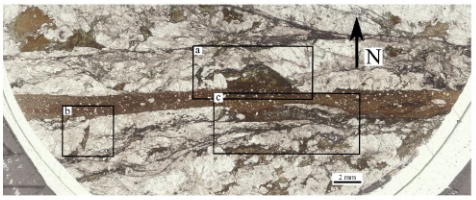

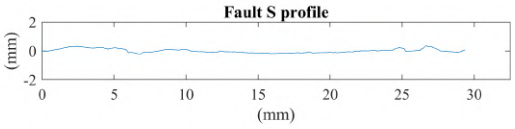

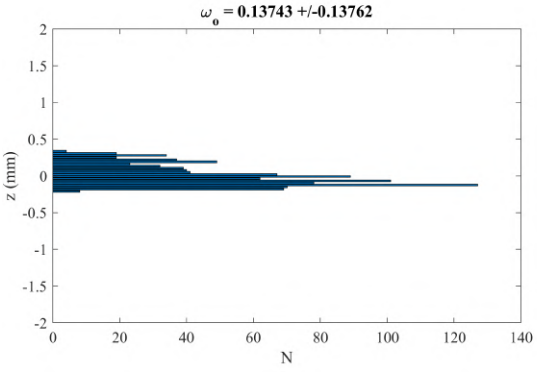

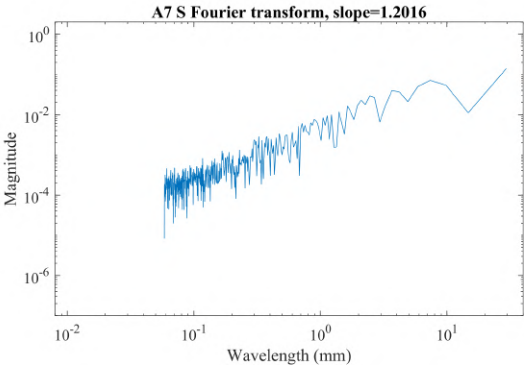

L05-02

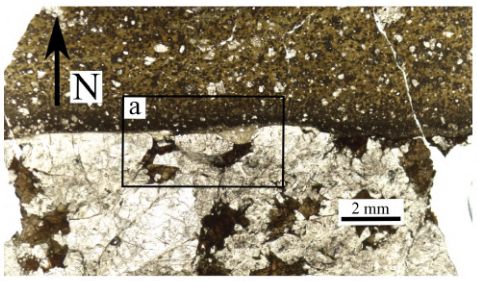
N
a
2 mm

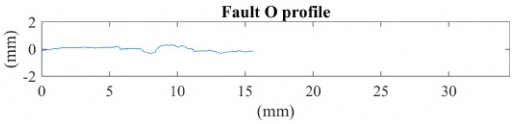
Fault O profile
(mm)
(mm)

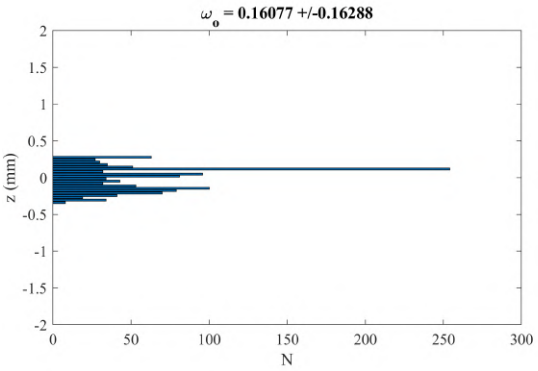
ω_o = 0.16077 +/-0.16288
z (mm)
N

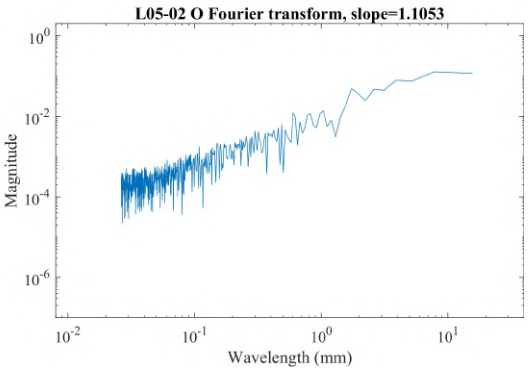
L05-02 O Fourier transform, slope=1.1053
Magnitude
Wavelength (mm)

L05-03

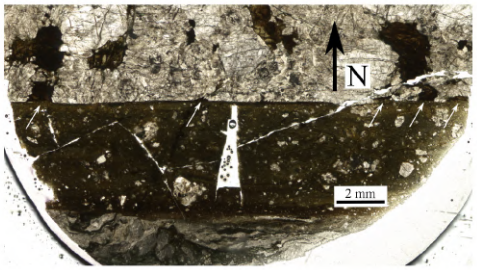
N
2 mm

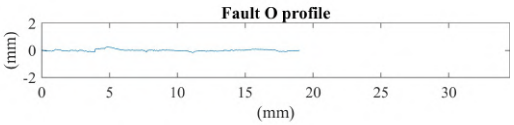
Fault O profile
(mm)
(mm)

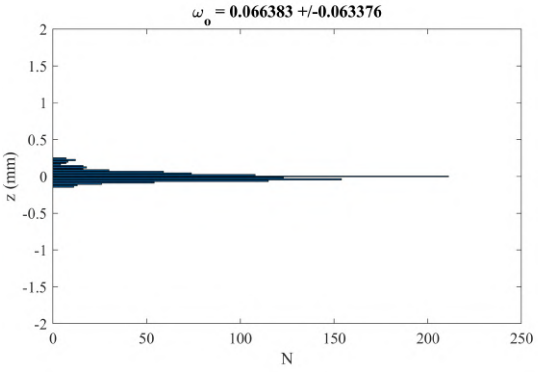
ω_o = 0.066383 +/-0.063376
z (mm)
N

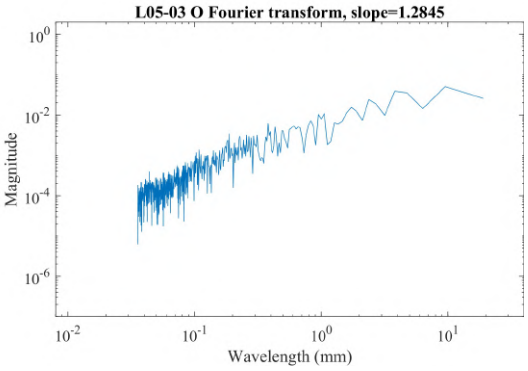
L05-03 O Fourier transform, slope=1.2845
Magnitude
Wavelength (mm)

L05-04 N

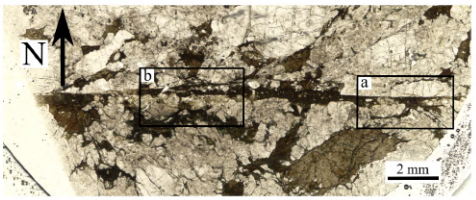

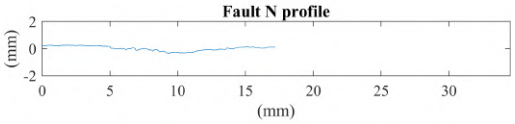

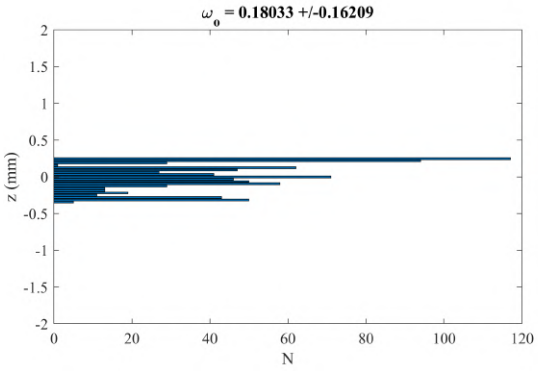

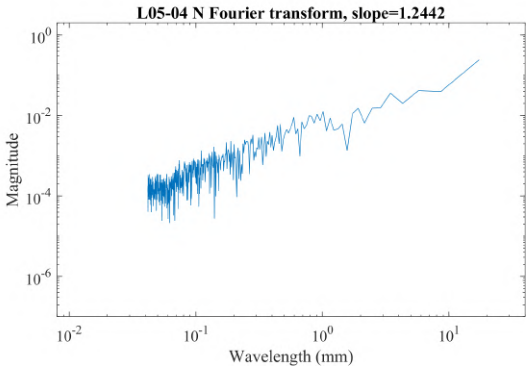

L05-04 S

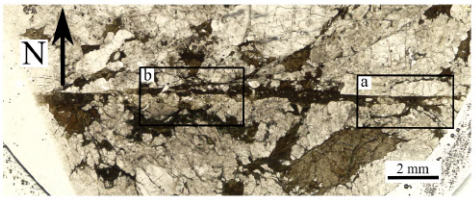

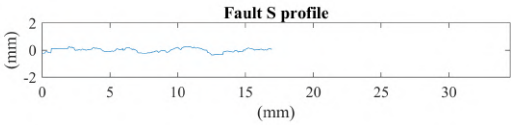

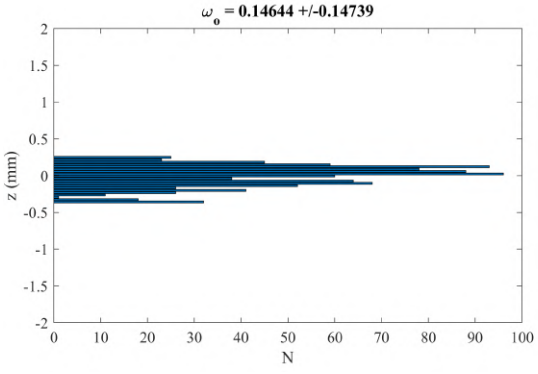

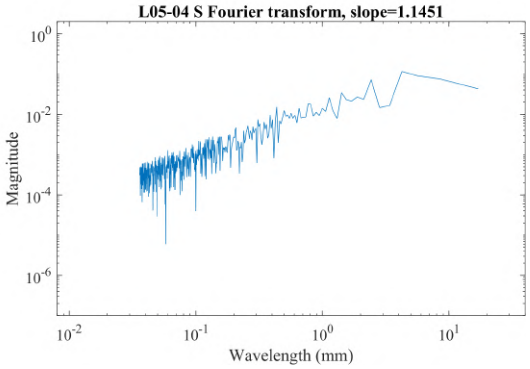

L05-06 N

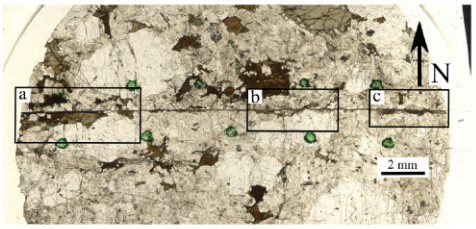

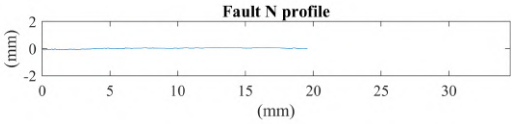

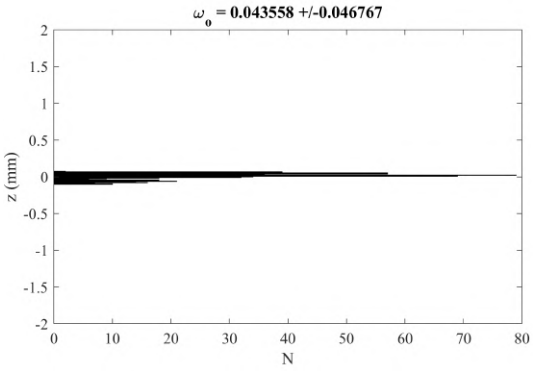

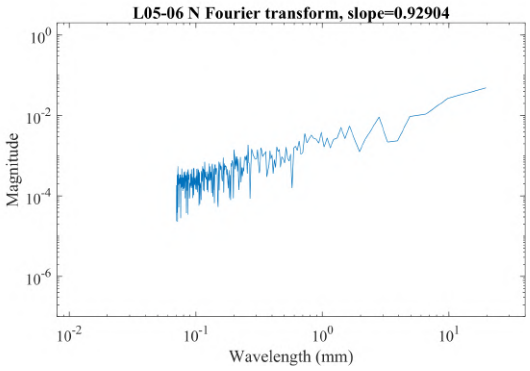

L05-06 S

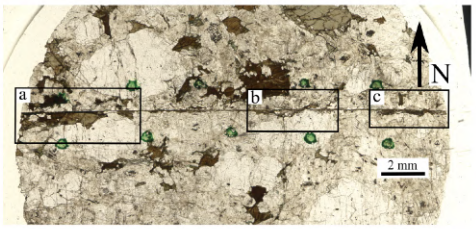

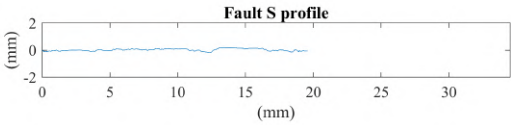

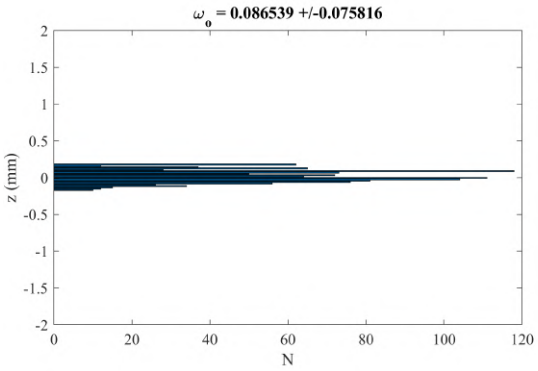

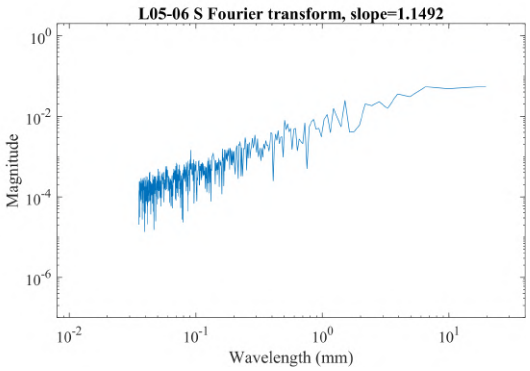

L05-07 N

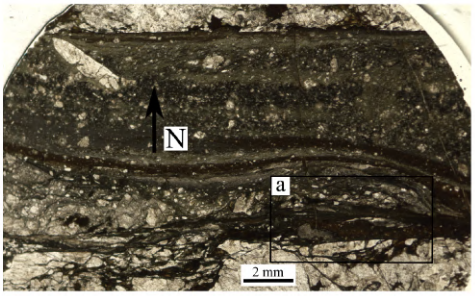

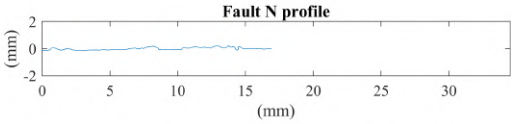

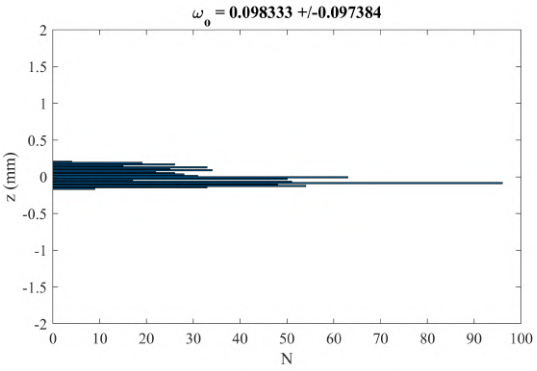

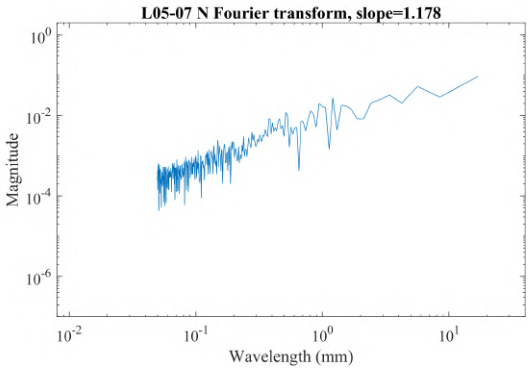

L05-07 S

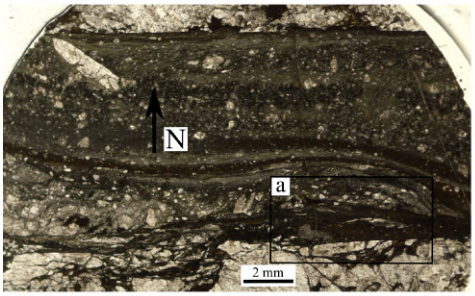

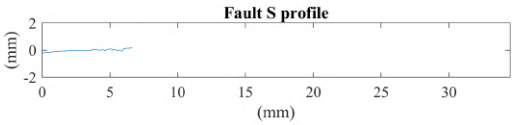

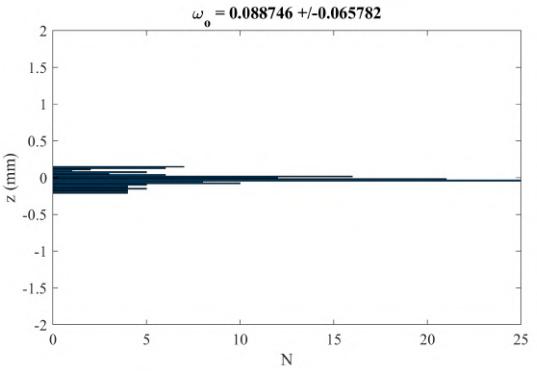

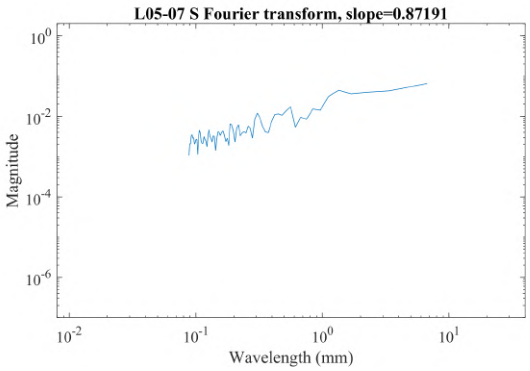

L05-08 N

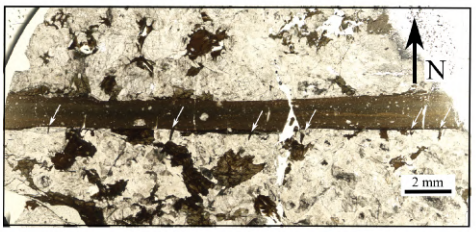

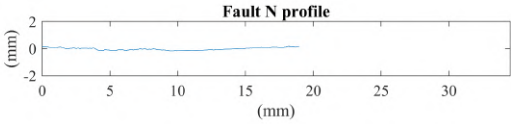

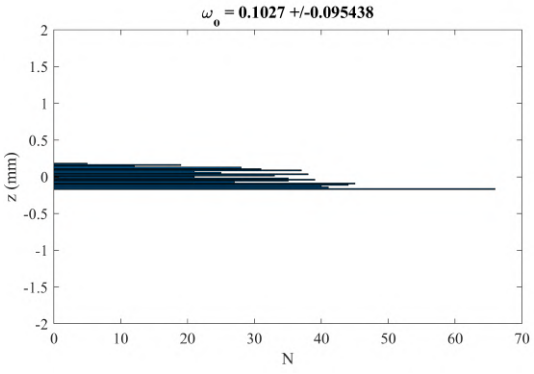

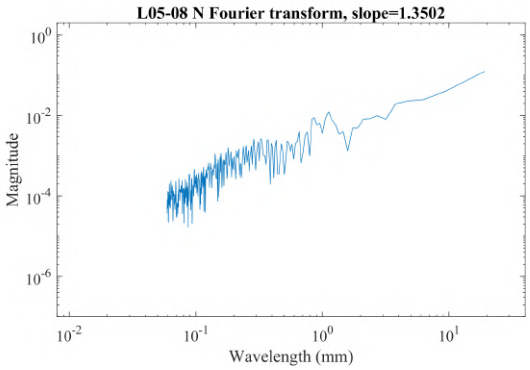

L05-08 S

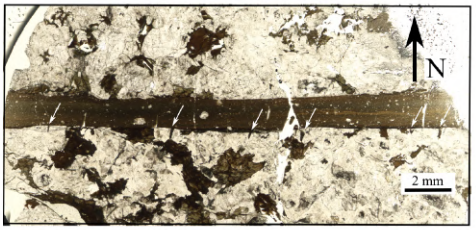

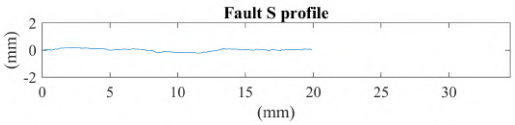

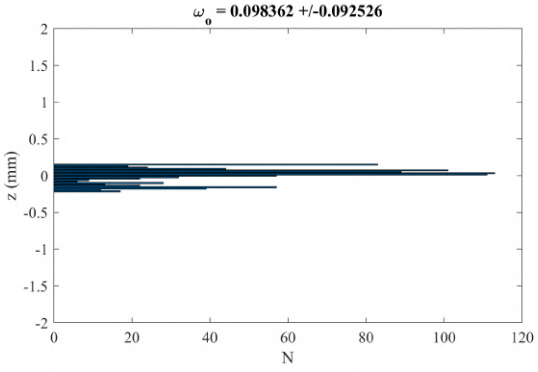

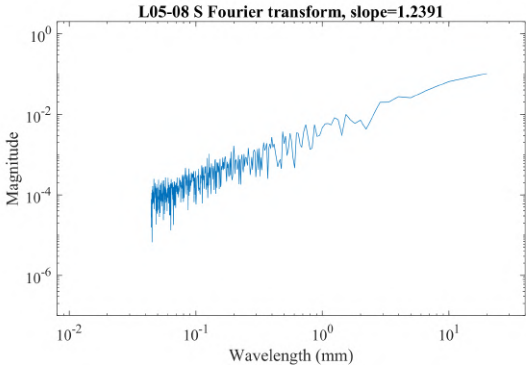

L09-01a N

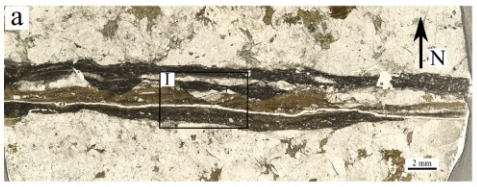

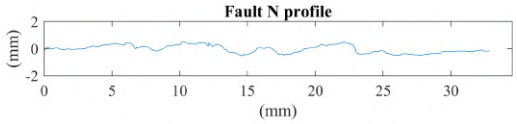

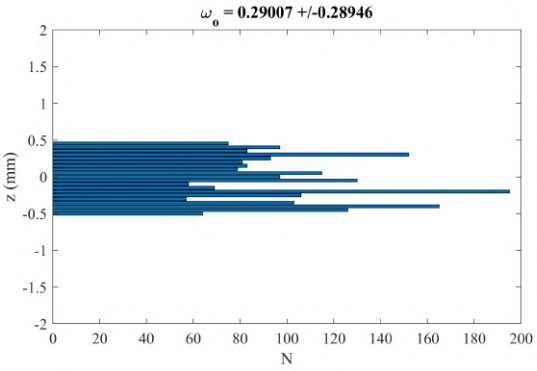

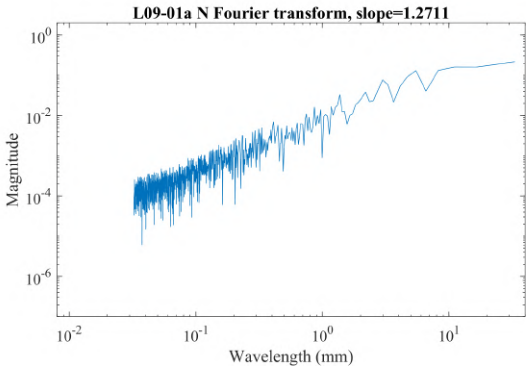

L09-01a S

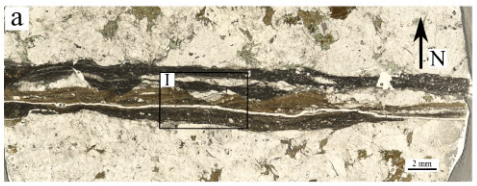

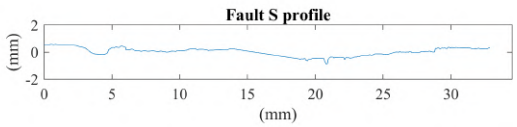

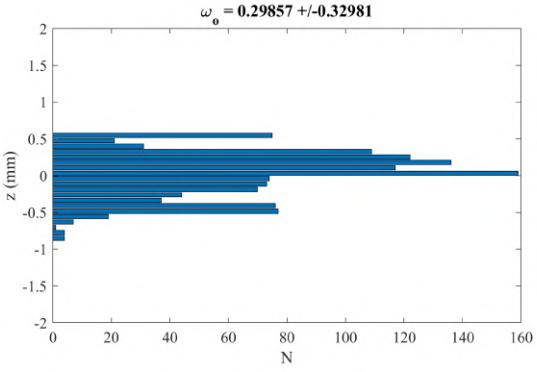

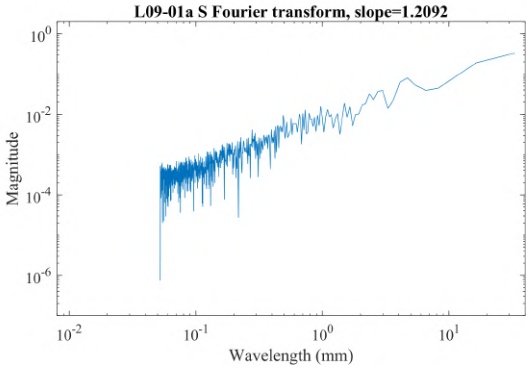

L09-01b N

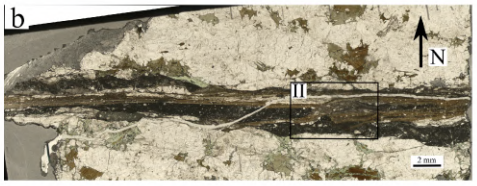

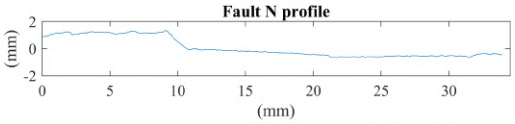

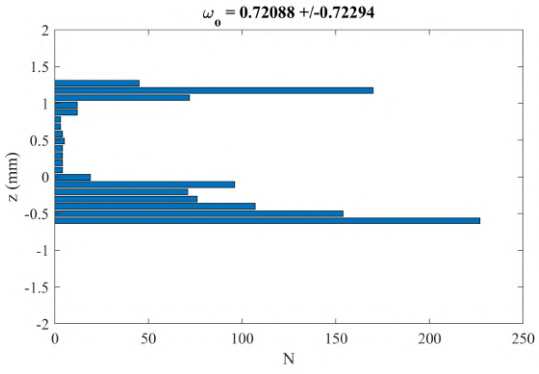

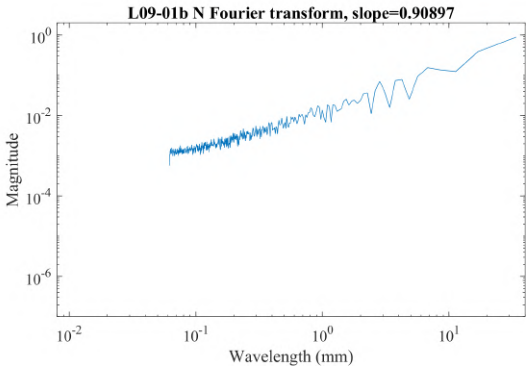

L09-01b S

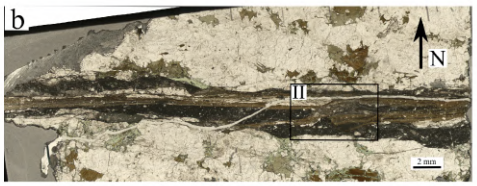

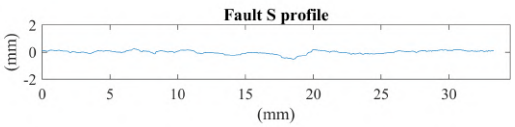

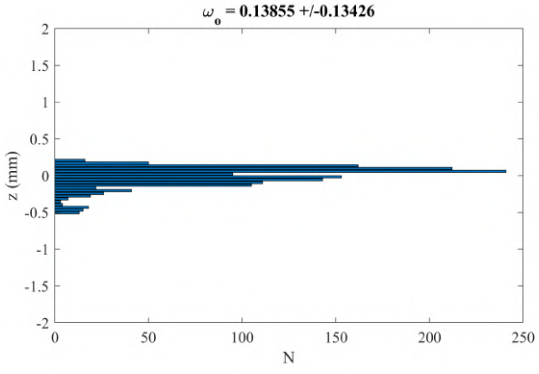

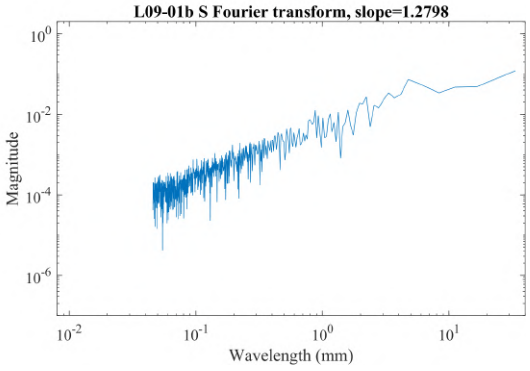

L09-02a N

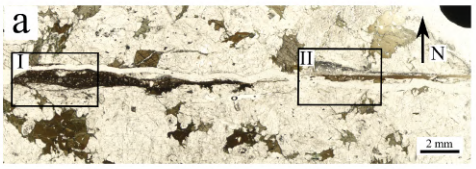

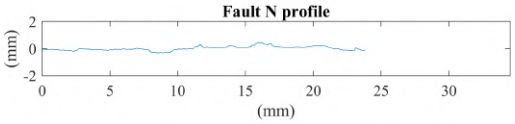

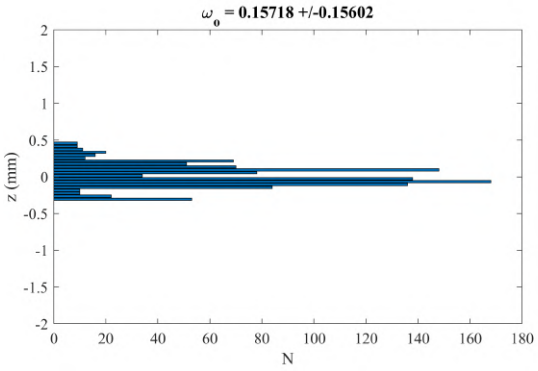

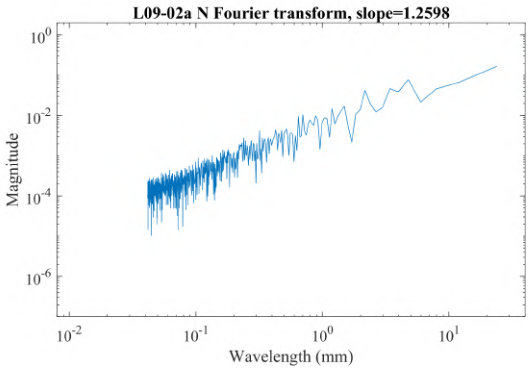

L09-02a S

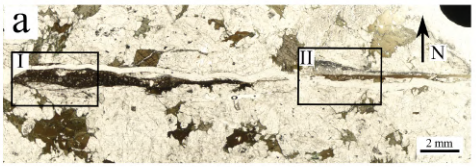

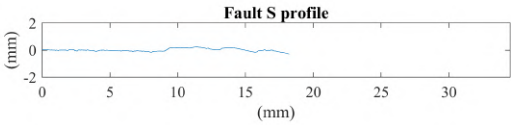

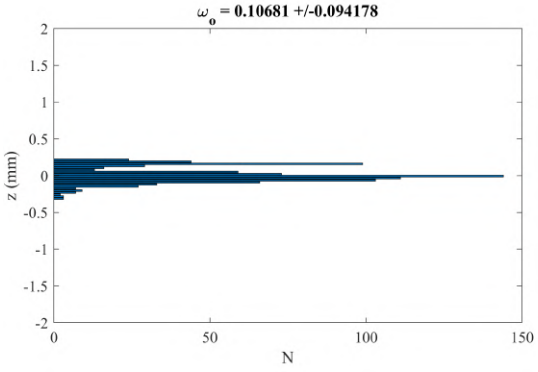

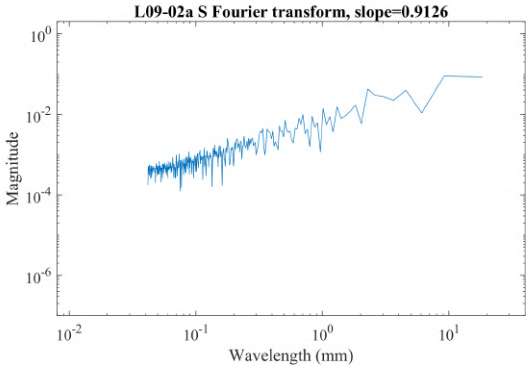

L09-02b N

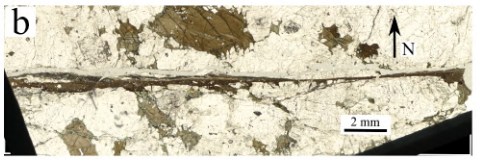

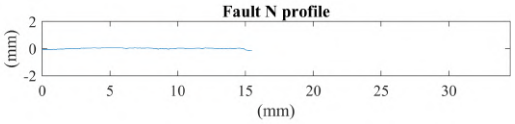

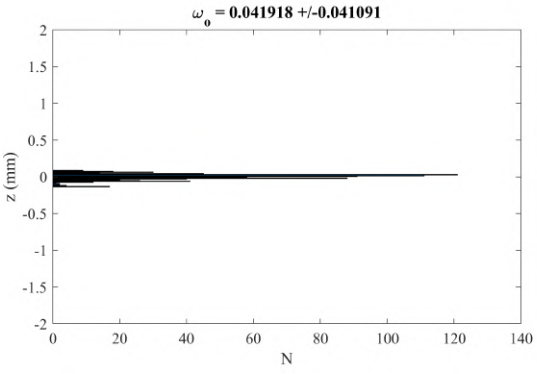

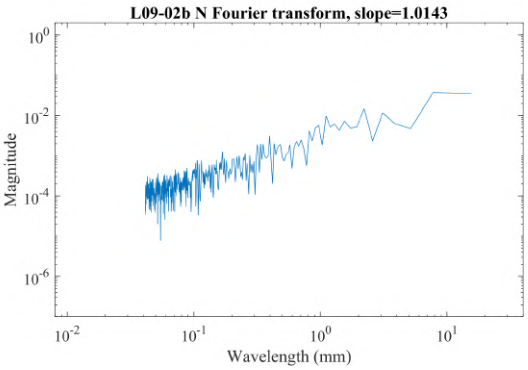

L09-02b S

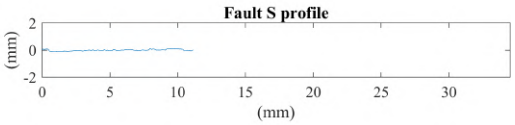

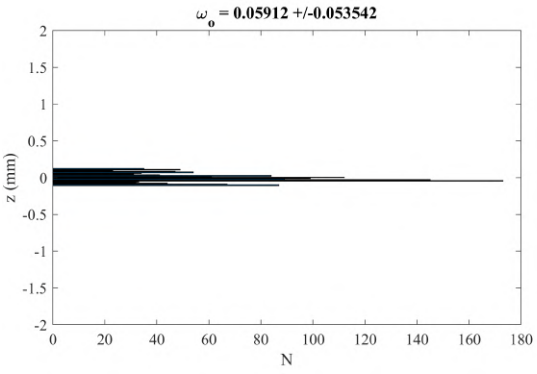

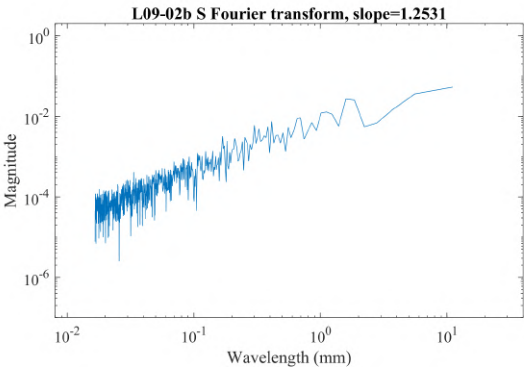

L09-03a N

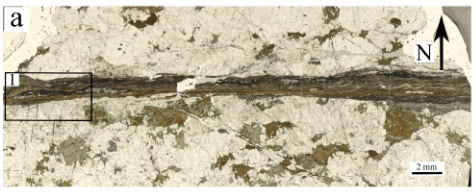

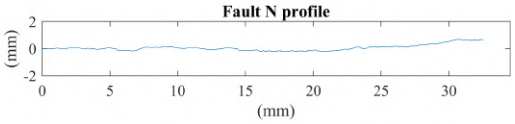

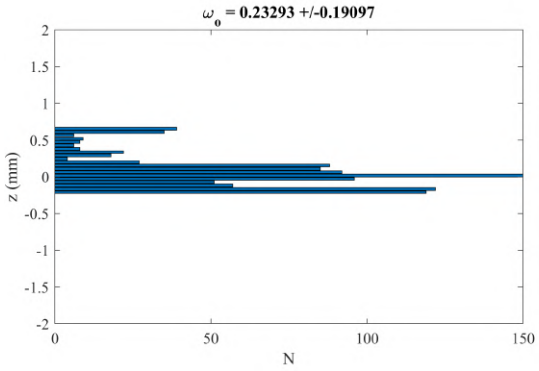

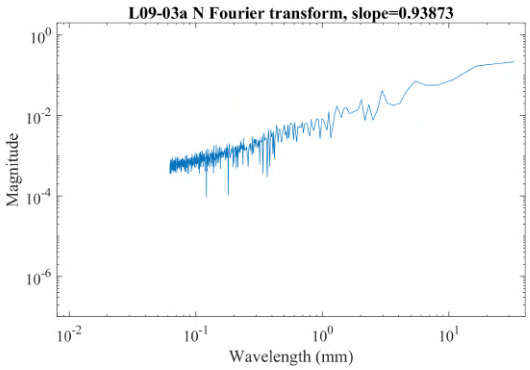

L09-03a S

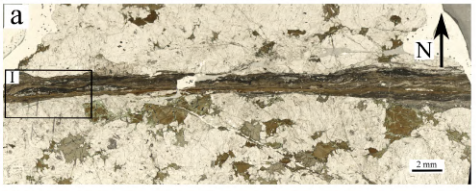

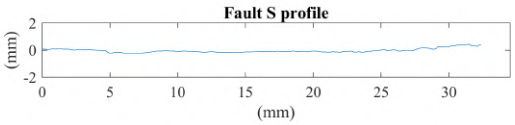

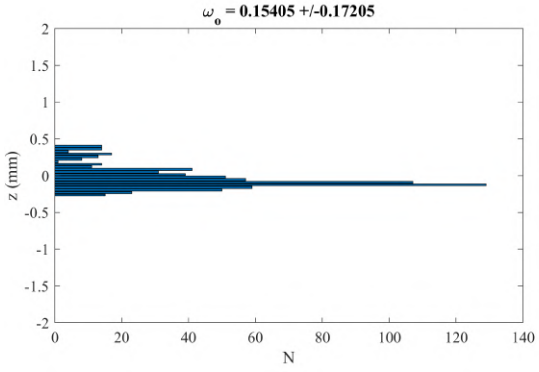

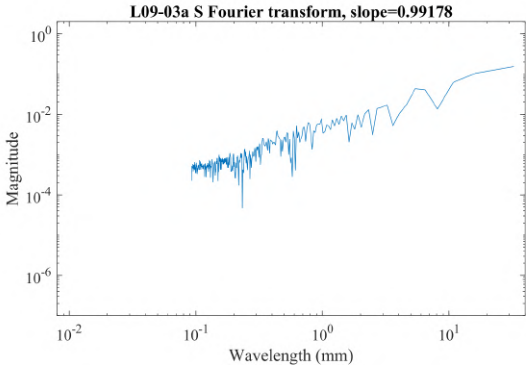

L09-03b N

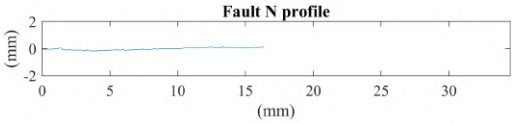

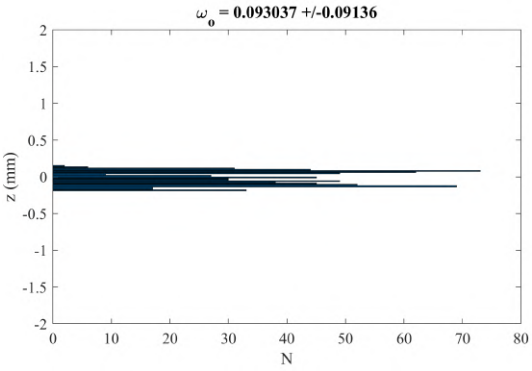

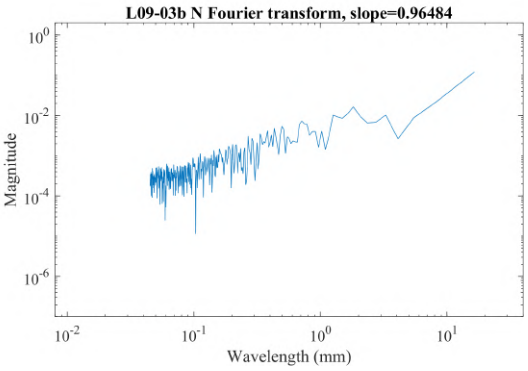

L09-03b S

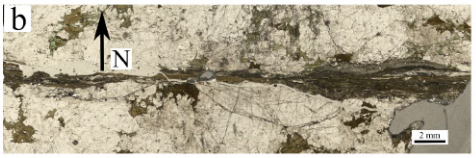

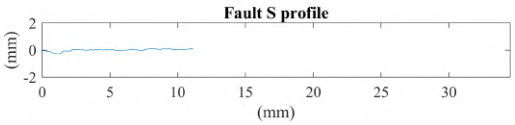

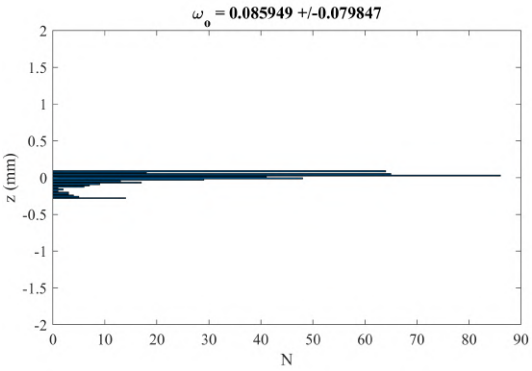

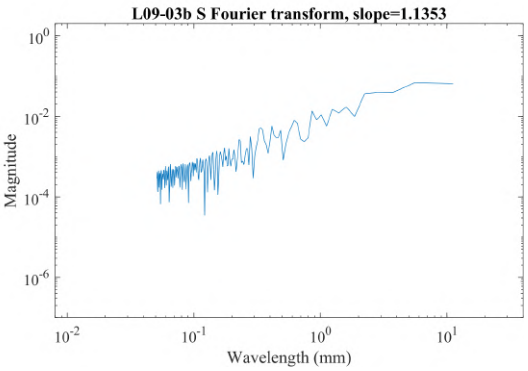

W05-S01 E

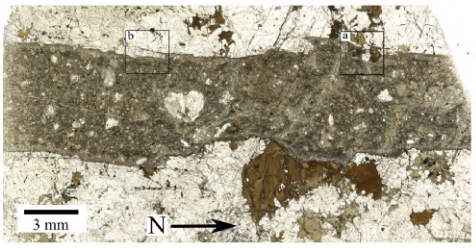

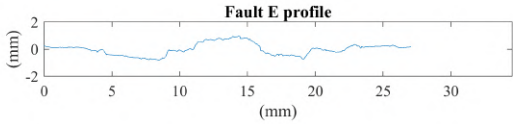

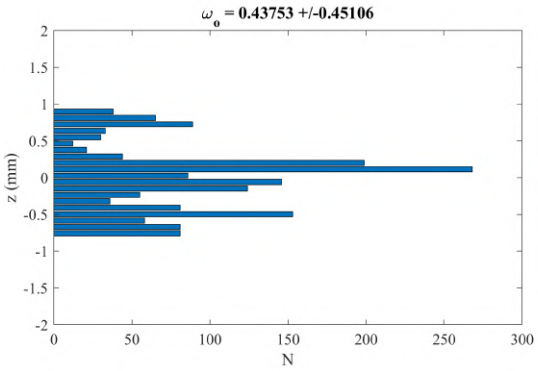

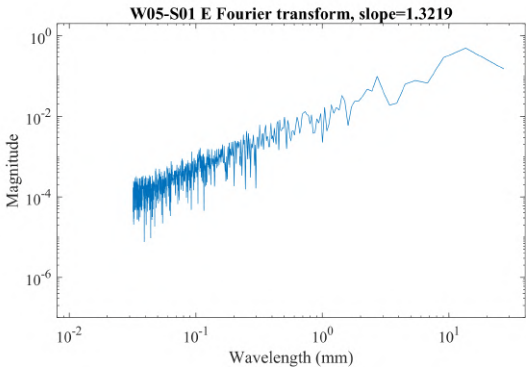

W05-S01 W

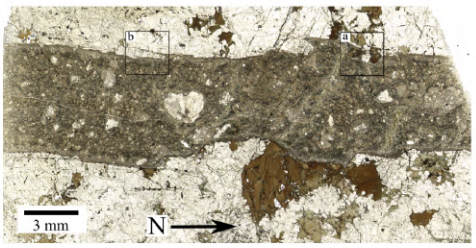

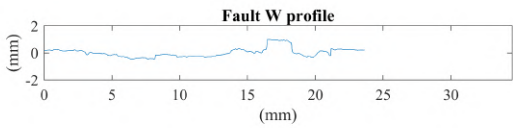

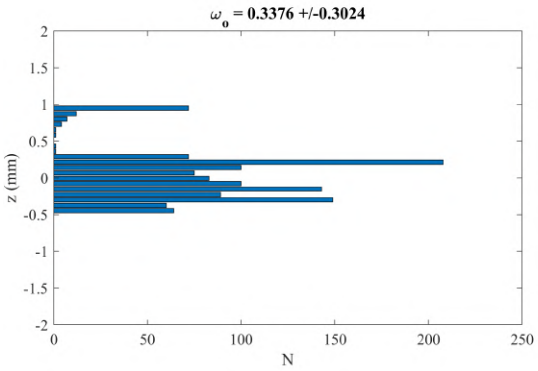

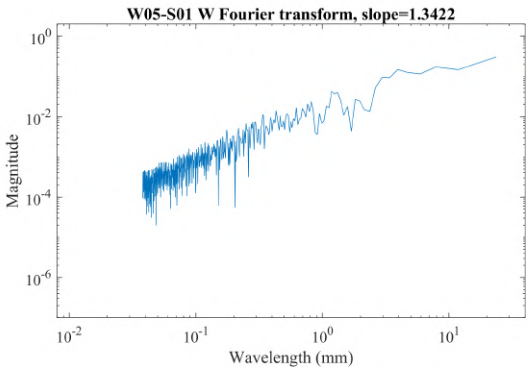

W05-S01 W selected

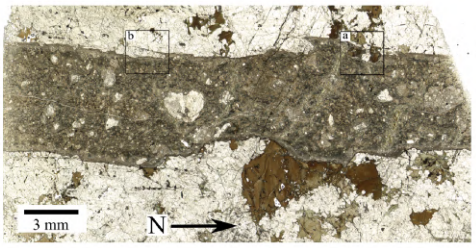

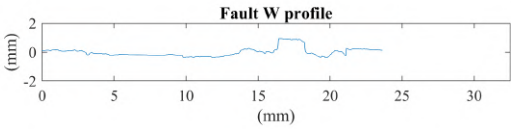

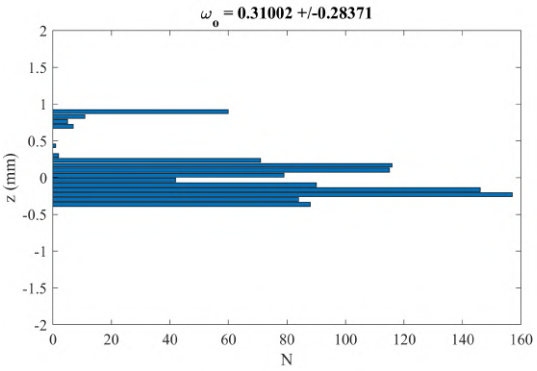

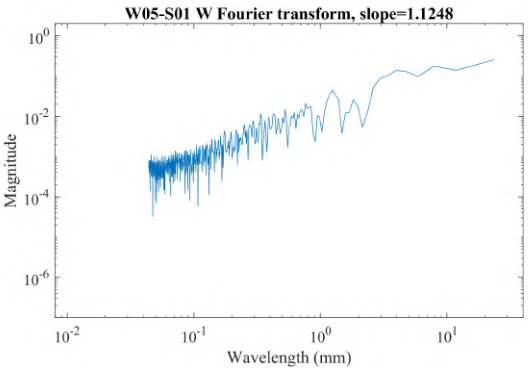

W05-S04 N

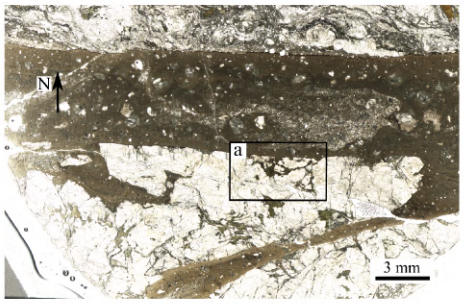

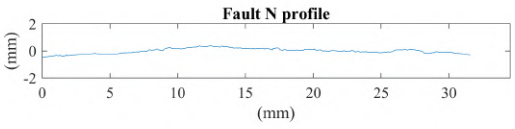

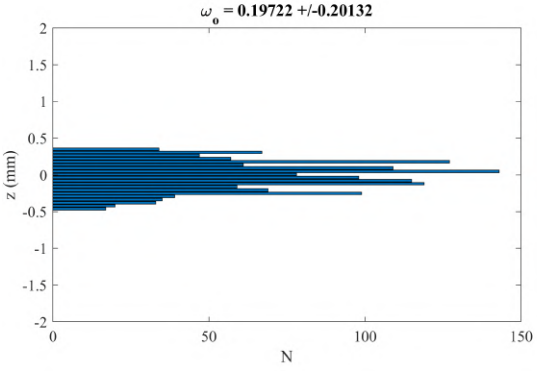

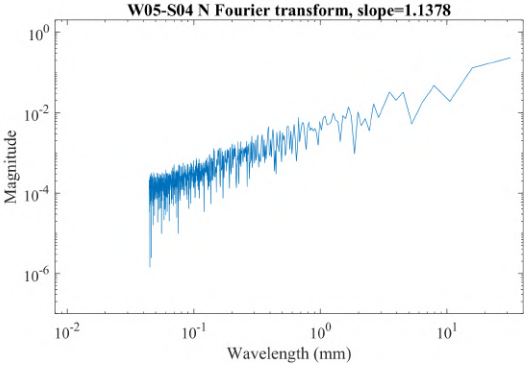

W05-S04 S

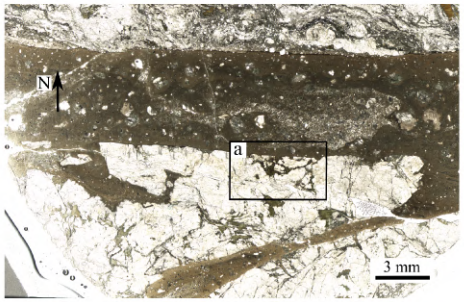

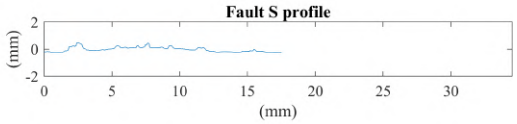

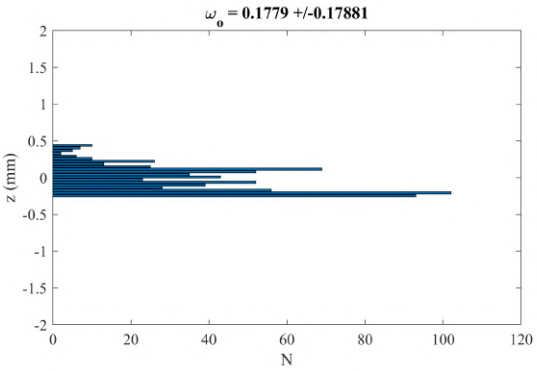

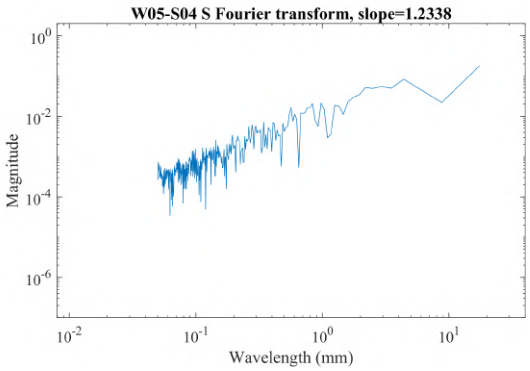

W09-S01 N

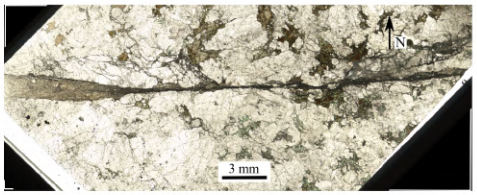

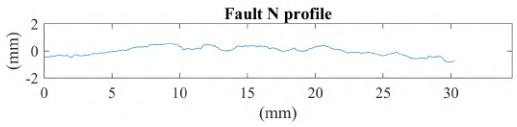

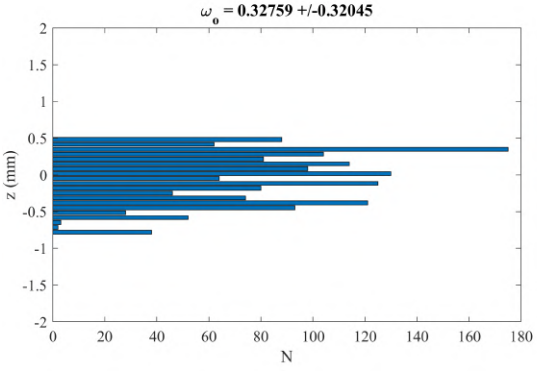

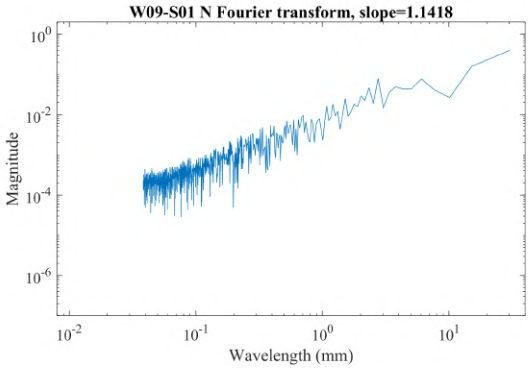

W09-S01 N selected

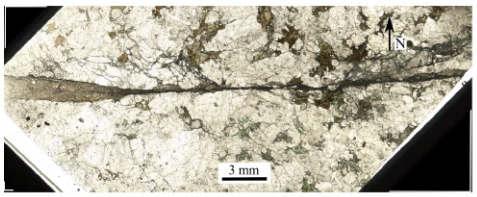

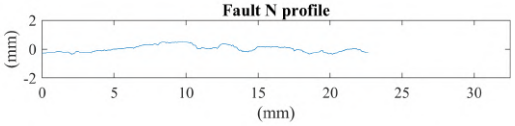

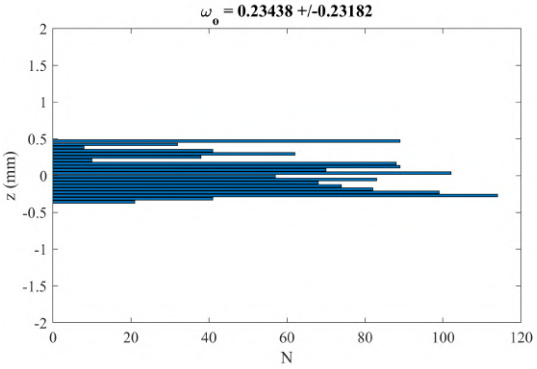

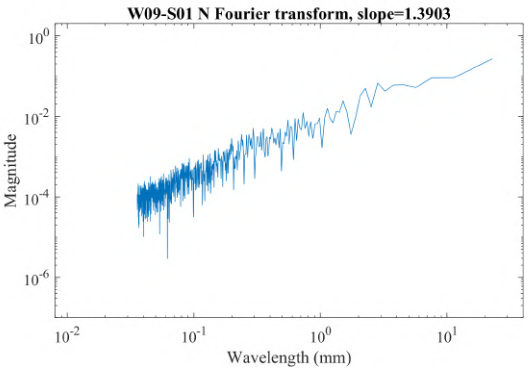

W09-S01 S